
Holistic simulation of optical systems

DISSERTATION

zur Erlangung des akademischen Grades
doctor rerum naturalium (Dr. rer. nat.)

vorgelegt an der Physikalisch-Astronomischen Fakultät der
Friedrich-Schiller-Universität Jena

von M. Sc. Johannes Maximilian Stock
geboren am 18. März 1993 in Ellwangen (Jagst)

Erster Gutachter: Prof. Dr. Herbert Gross, Friedrich-Schiller-Universität Jena

Zweiter Gutachter: Prof. Dr. Alois Herkommer, Universität Stuttgart

Dritter Gutachter: Prof. Dr. Alexander Rohrbach, Universität Freiburg

Tag der Disputation: 9. März 2020

Ganzheitliche Simulation optischer Systeme

Ausgehend von einer linearen Anordnung einfacher Komponenten, wie beispielsweise sphärischen Linsen und Spiegeln, und einer geometrisch-optischen Beschreibung hat sich die Optik zu einem immer komplexer werdenden Gebiet entwickelt. Viele moderne Systeme basieren neben der Brechung auf weiteren optischen Effekten, wie beispielsweise Beugung, Kohärenz, Polarisation und Streuung, enthalten präzise gefertigte Freiformflächen oder digitale Signalverarbeitung. Für eine umfangreiche und aussagekräftige Vorhersage der Leistung solcher Systeme, können diese Aspekte in der Simulation meist nicht vernachlässigt werden. Außerdem führt eine entkoppelte Betrachtung der einzelnen Teilbereiche oftmals nicht zu einem erfolgreicher Abgleich mit dem real gefertigten Aufbau. Ein Ziel der Dissertation ist die Erarbeitung umfassender, systemischer Ansätze zur Konzeption und Simulation moderner optischer Systeme. Durch die Entwicklung neuer Algorithmen und Modelle soll eine zunehmend ganzheitliche Beschreibung und Optimierung ermöglicht und deren Nutzen diskutiert werden.

Als Grundlage für eine ganzheitliche Simulation optischer Systeme wurde eine modulbasierte Simulationsumgebung erarbeitet, welche sowohl die Zusammenführung vorhandener Modelle als auch die Integration neuer Ansätze ermöglicht. Selbstverständlich können im Rahmen dieser Arbeit nur eine Auswahl der nahezu unüberschaubaren Anzahl an relevanten Aspekten adressiert werden. Der Fokus liegt hierbei auf der Berücksichtigung gefertigter Komponenten und realer Lichtquellen, der Integration nachgeschalteter Signalverarbeitung und physikalischer Effekte, wie beispielsweise Streuung und Beugung. Ein wichtiger Teil für die Verbindung einzelner Komponenten ist die Beschreibung der Lichtausbreitung im freien Raum. Im Rahmen der Arbeit wird ein neuer Algorithmus für die wellenoptische Propagation von kohärentem Licht zwischen beliebig gekippten Ebenen vorgestellt. Durch eine Zerlegung der allgemeinen Rotationsmatrix kann auf eine komplexe Interpolation verzichtet werden. Ein Vergleich mit bestehenden Alternativen ist Teil der Arbeit. Ein erfolgreicher Abgleich mit dem gefertigten System kann oftmals nur unter Berücksichtigung von herstellungsbedingten Fertigungsfehlern und Justagetoleranzen erfolgen. Speziell für die Simulation und Tolerierung von abbildenden Systemen, welche diamantgedrehte Freiformflächen enthalten, wird eine Lösung vorgestellt. Basierend auf einer analytischen Beschreibung der gefertigten Substrate, kann deren Einfluss

auf die Abbildungsleistung des Systems untersucht werden. Die Verifizierung der Methode ist exemplarisch an Messergebnissen erbracht. Ein weiterer Schritt zu einer umfassenderen Systemsimulation ist die Berücksichtigung der verwendeten Lichtquelle. Für die Analyse eines kompakten, hoch-sensitiven Streulichtensors wurde, neben der Integration von digitaler Signalverarbeitung und einem für die Anwendung kritischen Schutzglases, die verwendete Laserdiode mittels Phasenrekonstruktion charakterisiert. Der entsprechende experimentelle Aufbau und eine Abschätzung der erreichten Genauigkeit sind Teil der Arbeit.

Insgesamt, ist der Funktionsnachweis einer ganzheitlichen Herangehensweise exemplarisch anhand unterschiedlicher Demonstratoren erfolgreich erbracht. Gegenüber einer Lösung der singulären Teilbereiche konnte gezeigt werden, dass eine ganzheitliche Betrachtung zu einer signifikant höheren Übereinstimmung mit den experimentell bestimmten Resultaten führt. Fernziel dieser Arbeit ist ein virtuelles Prototyping, welches die industrielle Entwicklung komplexer Optiken hinsichtlich Kosten, Risiken und Entwicklungszeiten erheblich verbessern würde.

Contents

1. Introduction	3
2. Fundamentals	7
2.1. Propagation of light	7
2.1.1. Angular spectrum of plane waves	9
2.1.2. Transport of intensity equation	13
2.1.3. Geometrical optics	14
2.2. Modeling of light scattering at rough surfaces	15
2.3. Description of surfaces	19
2.3.1. Polynomial expansions	20
2.3.2. Radial basis functions	21
3. Concept for a holistic simulation of optical systems demonstrated on a thin-disk multipass amplifier	23
3.1. General concept	25
3.2. Description of the modules	29
3.3. Results	36
4. Coherent light propagation between tilted planes	43
4.1. Development and analysis of a quasi-fast algorithm	44
4.2. Example I: Gaussian Beam on a folding mirror	52
4.3. Example II: Intensity distribution on a high-order Littrow grating	55
4.4. Comparison to interpolation based methods	56
5. Simulation and analysis of imaging systems including real freeform components	61
5.1. Surface description of diamond-turned freeform components	63
5.2. Holistic simulation of an afocal, anamorphic imaging telescope in the visible wavelength range	67

5.3. Results and verification	69
5.4. Tolerance analysis	75
6. Holistic simulation of a table-top scattering setup	77
6.1. Characterization of the real light source by phase retrieval	79
6.2. Simulation concept of the system	86
6.3. Integration of a cover glass	94
6.4. Summary	97
7. Conclusion and outlook	99
Bibliography	101
A. Ehrenwörtliche Erklärung	117
B. Liste der wissenschaftlichen Veröffentlichungen und Vorträge	119
C. Danksagung	121

1. Introduction

For many years, the design of optical systems mainly comprised a linear arrangement of plane or spherical components, such as lenses, mirrors or prisms, and a geometric-optical description by ray tracing lead to an accurate and satisfactory result. Today, many modern optical systems found in a variety of different industrial and scientific applications, deviate from this structure. Polarization, diffraction and coherence, or material interactions, such as volume or surface scattering, need to be included when reasonable performance predictions are required. For example, this is apparent in the simulation of optical coherence tomography systems or fluorescence microscopes for biological applications [1,2]. For high-power laser systems used in material processing [3], an agreement with the experimental measurements is often only achievable if non-linear gain effects and thermal lensing within the active medium are considered. In the field of ultra-fast optics, short pulses and time-dependent interactions need to be described [4,5]. Modern manufacturing technologies allow for the realization of complex components with a variety of different functions. For example, ultracompact multi-lens objectives can be printed using two-photon laser writing [6,7] whilst diffractive structures with nanoscopic dimensions can be realized by lithography [8]. Furthermore, selective laser melting in combination with ultra-precise diamond-turning [9] and magnetorheological finishing [10] enables the construction of lightweight mirrors and housings. This technology is commonly used in space applications [11,12] as a result of its resistance to thermal and mechanical influences. Independent of the production method however, limitations for the application still exist as a consequence of surface imperfections, such as regular mid spatial frequencies [13]. These aspects must be considered in the design and simulation of optical systems to ensure that their impact is not damaging to the overall purpose of the corresponding setup. Another important part is the growing field of digital optics. Signal processing algorithms have become an indispensable part of many systems, whereby an almost unlimited number of current and potential applications exists. These include modern microscopy systems [14], whose usage

comprises various medical applications [15], and even consumer electronics such as digital compact or smartphone cameras [16], wherein the final image is heavily based on post processing. Since these algorithms are an essential part of the system, their compatibility and impact on the completed system is an important aspect to consider. In principle, this list of relevant topics and examples can be further expanded to an almost unlimited extend. However, the simulation and optimization of the single sub-aspects do often not lead to a satisfactory result. The goal of this thesis is to demonstrate that the performance prediction of modern optical systems benefits significantly from an aggregation of the individual models and technological aspects. Present concepts should be further enhanced by the development and analysis of new approaches and algorithms, leading to a more holistic description and simulation of complex setups as a whole. The long-term objective of this work is a comprehensive virtual and rapid prototyping. From an industrial perspective, this would reduce the risk, time and costs associated with the development of an optical system.

Currently, there exist several concepts for a modular design of basic optical systems within the literature [17–21]. Additionally, there is a wide range of software tools, both open source and commercially available, which address different simulation aspects [22–24]. Instead of selecting a single, application-specific distribution which is limited by predefined interfaces, a modular framework is constructed in order to allow for a more holistic simulation. By a flexible and transparent realization, problem-specific approaches can be combined and further enhanced through new models and solutions. It is clear that the almost unlimited number of different aspects and effects to describe all kind of optical systems cannot be covered within this work. Therefore, the developed toolbox is exemplary filled for several systems, spanning a range of different topics, and new approaches are developed within this thesis to achieve a more holistic simulation and demonstrate the associated benefits and opportunities. A central part for the connection of the individual components is the propagation of light in a linear, homogeneous and isotropic medium. While mostly the propagation between parallel planes is considered, the evaluation of a coherent field distribution on a tilted plane is of special interest, when dealing with an off-axis geometry or designing modern computer generated holograms [25]. In comparison to the extensively studied propagation between parallel planes [26–29], fast Fourier transforms cannot be applied straightforward due to a non-equidistant grid spacing. Several algorithms have been previously developed to deal with this

problem using complex interpolation [30–34]. This is unfortunately accompanied by varying levels of inaccuracy, depending on the magnitude of the rotation angles [35]. In this work, a new method is presented based on a decomposition of the general rotation matrix. Established through comparisons with state-of-the-art algorithms, this new approach maintains a greater level of accuracy even for large rotation angles, independent of the application. The consideration of imperfections on freeform surfaces resulting from the diamond-turning process is another challenge addressed in this work. There currently exists a few comprehensive approaches for the analysis of different fabrication processes [36, 37] and the theoretical descriptions of surface deformations on the optical performance [38–42]. However, despite this research, there still exists a need for a more holistic description of systems, including multiple real freeform components. Based on an analytic approximation of the manufactured surface profiles, a new solution is presented in this thesis that enables performance predictions based on the system as a whole. This approach is demonstrated and compared successfully to measured data for an afocal, anamorphic imaging telescope in the visible wavelength range [43]. In addition, the concept of a holistic simulation, is further investigated on two more setups. The first is a wave-optical simulation of a thin-disk multipass amplifier [44], involving gain effects and thermal lensing. The second is a table-top scattering setup [45] whereby signal processing algorithms, surface scattering and multiple reflected light at a cover glass are taken into account for the performance prediction. Furthermore, the characterization of the light source by a modified phase retrieval approach based on the transport of intensity equation [46] is realized.

The thesis is structured as follows. In Chapter 2, the necessary fundamentals are introduced. On the basis of Maxwell’s equations, several state-of-the-art free-space propagation algorithms are derived and possible approximations are discussed. Using the semi-analytical Fourier and the chirp z-transform, methods for an efficient and flexible sampling are then described. Additionally, the modeling of light scattering at rough surfaces and several approaches for analytic surface descriptions through global polynomials and radial basis functions are outlined. The motivation and concept behind a modular framework for more holistic simulations is introduced in Chapter 3. For a better demonstration and to derive general requirements, the modules are exemplary implemented for a thin-disk multipass amplifier. The used approximations are discussed and the results are subsequently analyzed. Additionally, the impact of alignment uncertainties on the beam quality during the adjust-

ment process are shown. The new algorithm for coherent light propagation between tilted planes is presented in Chapter 4. After the idea of decomposing a general rotation into three elementary transformations is outlined, two application-related examples are evaluated. These comprise a Gaussian beam on a folding mirror and the intensity distribution on a high-order Littrow grating. The performance of the quasi-fast algorithm is analyzed and the approach is compared to the Rayleigh-Sommerfeld diffraction integral and interpolation-based solutions for different rotation angles. In Chapter 5, a solution for a more holistic simulation by including the impact of diamond-turned freeform components is introduced. After the real surface profiles are measured and approximated through an analytic description, their integration back into the optical design is realized based on the modular framework. An afocal, anamorphic, imaging telescope is used as a practical example for this process. Its corresponding results are analyzed and the solution is verified by a comparison against measured wavefronts. How the approach can be used for a comprehensive tolerance analysis of the surface shapes is demonstrated at the end of this chapter. A holistic simulation of a modern table-top scattering setup is outlined in Chapter 6. The used laser light source is characterized through a modified phase retrieval approach. This happens before the systems performance is predicted, which occurs by taking the surface scattering at the mirror and the necessary post processing of the captured images into account. The wave-optical simulation is then further enhanced by the inclusion of a critical cover glass for the protection of the system. The simulation results are discussed and compared to corresponding measurements. The thesis concludes with a summary and an outlook of future research based on this work.

2. Fundamentals

In this chapter, relevant fundamentals for this thesis are introduced. Based on Maxwell's equations, several approaches for a wave-optical description of light are outlined and possible approximations are discussed. Apart from this, the modeling of light scattering at rough surfaces and two different approaches for an analytic description of surfaces by global polynomials and more local radial basis functions are studied. The chapter concludes with a brief overview on available software distributions for the simulation of optical systems.

2.1. Propagation of light

In the theory of electromagnetic optics, light is described by a vectorial electric field $\boldsymbol{\mathcal{E}} = (\mathcal{E}_x, \mathcal{E}_y, \mathcal{E}_z)^\top$ and a magnetic field $\boldsymbol{\mathcal{H}} = (\mathcal{H}_x, \mathcal{H}_y, \mathcal{H}_z)^\top$, which are dependent on the time t and the position $\mathbf{r} = (x, y, z)^\top$. Following the literature in [27, 28, 47], the vectors are related by Maxwell's equations in a source-free medium

$$\nabla \times \boldsymbol{\mathcal{H}}(\mathbf{r}, t) = \frac{\partial \boldsymbol{\mathcal{D}}(\mathbf{r}, t)}{\partial t}, \quad (2.1)$$

$$\nabla \times \boldsymbol{\mathcal{E}}(\mathbf{r}, t) = -\frac{\partial \boldsymbol{\mathcal{B}}(\mathbf{r}, t)}{\partial t}, \quad (2.2)$$

$$\nabla \cdot \boldsymbol{\mathcal{D}}(\mathbf{r}, t) = 0, \quad (2.3)$$

$$\nabla \cdot \boldsymbol{\mathcal{B}}(\mathbf{r}, t) = 0. \quad (2.4)$$

Here, ∇ is the nabla operator, $\boldsymbol{\mathcal{D}}$ is the electric displacement and $\boldsymbol{\mathcal{B}}$ is the magnetic induction. In linear, nondispersive, isotropic and homogeneous media the following relation holds

$$\mathcal{D}(\mathbf{r}, t) = \epsilon \mathcal{E}(\mathbf{r}, t), \quad (2.5)$$

$$\mathcal{B}(\mathbf{r}, t) = \mu \mathcal{H}(\mathbf{r}, t). \quad (2.6)$$

where ϵ is the electric permittivity and μ the magnetic permeability. Both are dependent on the electric and magnetic properties of the medium and are connected to its refractive index by $n = c/c_0 = \sqrt{\epsilon\mu/(\epsilon_0\mu_0)}$. Here, c/c_0 is the ratio between the speed of light in the medium and in vacuum, ϵ_0 and μ_0 are the respective constants in vacuum. Relying on the inverse Fourier transform, the time dependent fields can be represented under this conditions by a superposition of monochromatic electromagnetic waves with a complex amplitude $\mathbf{E}(\mathbf{r}, \omega)$ and $\mathbf{H}(\mathbf{r}, \omega)$, dependent on the angular frequency ω ,

$$\mathcal{E}(\mathbf{r}, t) = \text{Re} \left\{ \frac{1}{\sqrt{2\pi}} \int_{-\infty}^{\infty} \mathbf{E}(\mathbf{r}, \omega) e^{i\omega t} d\omega \right\}, \quad (2.7)$$

$$\mathcal{H}(\mathbf{r}, t) = \text{Re} \left\{ \frac{1}{\sqrt{2\pi}} \int_{-\infty}^{\infty} \mathbf{H}(\mathbf{r}, \omega) e^{i\omega t} d\omega \right\}. \quad (2.8)$$

Using the relation $\frac{\partial}{\partial t} \exp(i\omega t) = i\omega \exp(i\omega t)$ and the Equations 2.5 and 2.6, the Maxwell equations in the spectral domain for a linear, nondispersive, isotropic and homogeneous medium are formulated for the complex amplitudes by

$$\nabla \times \mathbf{H}(\mathbf{r}, \omega) = i\omega \epsilon \mathbf{E}(\mathbf{r}, \omega), \quad (2.9)$$

$$\nabla \times \mathbf{E}(\mathbf{r}, \omega) = -i\omega \mu \mathbf{H}(\mathbf{r}, \omega), \quad (2.10)$$

$$\nabla \cdot \mathbf{E}(\mathbf{r}, \omega) = 0, \quad (2.11)$$

$$\nabla \cdot \mathbf{H}(\mathbf{r}, \omega) = 0. \quad (2.12)$$

For a dispersive medium, ϵ and μ are dependent on the angular frequency. Furthermore, the homogeneous wave equation is derived for the electric and magnetic

field by taking the curl of Equation 2.10 and 2.9, respectively, and using the vector identity $\nabla \times (\nabla \times \mathbf{U}) = \nabla(\nabla \cdot \mathbf{U}) - \nabla^2 \mathbf{U}$

$$\nabla^2 \mathbf{H}(\mathbf{r}, \omega) + k^2 \mathbf{H}(\mathbf{r}, \omega) = 0, \quad (2.13)$$

$$\nabla^2 \mathbf{E}(\mathbf{r}, \omega) + k^2 \mathbf{E}(\mathbf{r}, \omega) = 0. \quad (2.14)$$

Here, $k = \omega/c$ is the wavenumber. In principle, one needs to find a solution, $\mathbf{H}(\mathbf{r}, \omega)$ or $\mathbf{E}(\mathbf{r}, \omega)$, for only one of these equations. Therefore, the following considerations are formulated based on the electric field only. The magnetic field is then given by Equation 2.10. Furthermore, the homogeneous equation does not contain any dependency between the individual components of the field and, consequently, can be solved by independent solutions of the scalar equations, which have the form of a Helmholtz equation. In the following sections, several modifications, solutions and their properties in terms of a numerical implementation are discussed.

2.1.1. Angular spectrum of plane waves

An elementary solution for the described problem are monochromatic plane waves

$$\mathbf{E}(\mathbf{r}, \omega) = \mathbf{E}_0(\omega) e^{-i\mathbf{k}\mathbf{r}}, \quad (2.15)$$

where the wavevector $\mathbf{k} = (k_x, k_y, k_z)^\top$ needs to fulfill $|\mathbf{k}| = \omega/c$. As a consequence of Maxwell's equations, the electric field of the plane wave must be perpendicular to the wavevector and the magnetic field, what is called a transverse electromagnetic wave. Due to the orthogonal relation of the vectors, only two components, or polarization states, of the electric field vector, say $E_{0x}(\omega)$ and $E_{0y}(\omega)$, can be chosen independently. The third component is then given by

$$E_{0z}(\omega) = -\frac{k_x E_{0x}(\omega) + k_y E_{0y}(\omega)}{k_z}. \quad (2.16)$$

As a consequence of the linearity of Equation 2.14, the principle of superposition

applies and also the linear combination of plane waves is a solution. A complex electric field across the $z = 0$ plane can be represented by its angular spectrum of plane waves according to

$$E_i(k_x, k_y, 0) = \frac{1}{\sqrt{2\pi}} \iint_{-\infty}^{+\infty} E_i(x, y, 0) e^{-i(k_x x + k_y y)} dx dy = \mathcal{F} \{E_i(x, y, 0)\}, \quad (2.17)$$

where i specifies the component of the field and \mathcal{F} is the Fourier transform. The important problem of light propagation in a linear, isotropic and homogeneous medium between parallel planes is solved by finding a relation to the angular spectrum at a position z and evaluating the inverse Fourier transform \mathcal{F}^{-1}

$$E_i(x, y, z) = \frac{1}{\sqrt{2\pi}} \iint_{-\infty}^{+\infty} E_i(k_x, k_y, z) e^{i(k_x x + k_y y)} dk_x dk_y = \mathcal{F}^{-1} \{E_i(k_x, k_y, z)\}. \quad (2.18)$$

By inserting Equation 2.18 into the wave equation, the desired relation is found to be

$$E_i(k_x, k_y, z) = E_i(k_x, k_y, 0) e^{ik_z z}, \quad (2.19)$$

$$k_z = \sqrt{\left(\frac{\omega}{c}\right)^2 - k_x^2 - k_y^2}. \quad (2.20)$$

The final result is then given by

$$E_i(x, y, z) = \mathcal{F}^{-1} \{ \mathcal{F} \{E_i(x, y, 0)\} e^{ik_z z} \}. \quad (2.21)$$

Without going into detail here, this relation can be approximated for the paraxial region by $k_z \approx \frac{\omega}{c} - \frac{c^2}{2\omega^2} k_x^2 - \frac{c^2}{2\omega^2} k_y^2$ and in the far field by $k_z \approx \frac{\omega}{c}$, which are called the Fresnel and Fraunhofer approximation, respectively.

From the viewpoint of numerical implementation, the discrete Fourier transforms (DFT) can be solved efficiently by the fast Fourier transform (FFT). Unfortunately, the spectral and spatial resolution are coupled and special caution must be taken on the sampling of the field distributions. Both aspects are addressed within the following explanations with respect to the simulation of optical systems.

Chirp z-transform

One possibility to overcome some of the limitations of the FFT, is the evaluation of the Fourier transform by a chirp z-transform, which will be briefly introduced according to [48] for one dimension. For a finite set of samples, the z-transform of a sequence of complex numbers $x_n \in \mathbb{C}$ is defined as

$$X_\kappa = \sum_{n=0}^{N-1} x_n z_\kappa^{-n}, \quad \kappa \in \mathbb{N}, z_\kappa \in \mathbb{C}. \quad (2.22)$$

One special form of the z-transform is the DFT with

$$z_\kappa = \exp\left(i2\pi \frac{\kappa}{N}\right), \quad \kappa = 0, 1, \dots, N-1. \quad (2.23)$$

Using the chirp z-transform, z_κ is considered in a more general way

$$z_\kappa = AW^{-\kappa}, \quad \kappa = 0, 1, \dots, M-1, \quad (2.24)$$

and a discrete Fourier transform with a more flexible sampling of the frequencies ν can be realized by

$$A = \exp(-i2\pi\nu_0\Delta x), \quad (2.25)$$

$$W = \exp(i2\pi\Delta\nu\Delta x), \quad (2.26)$$

where Δx is the spacing of the samples, $\Delta \nu$ is the spacing of the frequencies and ν_0 is an arbitrary starting frequency. According to [49], the overall result of the form

$$X_\kappa = \sum_{n=0}^{N-1} x_n A^{-n} W^{nk}, \quad \kappa = 0, 1, \dots, M-1, \quad (2.27)$$

can be reformulated in terms of a convolution and efficiently calculated by the use of three conventional FFTs. In summary, the chirp z-transform can be interpreted as a loop in the frequency domain and a $\Delta \nu$ - Δx -decoupling. This is of special interest for the evaluation of cascaded diffraction [50, 51] because additional interpolation can be avoided.

Analytic handling of the linear and quadratic phase

When simulating optical systems, typically, one has to deal with linear and spherical wavefronts or phases. In order to allow for an accurate numerical evaluation of Equation 2.21, the phase of the input field and the propagation kernel needs to be sampled properly [27]. The required lateral sampling can be reduced by an analytic handling of the linear and quadratic phase terms [52]. Apart from using the shift theorem of the Fourier transformation

$$\mathcal{F}\{E(x + \Delta x, y + \Delta y)\} = E(k_x, k_y) \exp(i\Delta x k_x + i\Delta y k_y), \quad (2.28)$$

$$\mathcal{F}\{E(x, y)e^{-i\Delta k_x x - i\Delta k_y y}\} = E(k_x + \Delta k_x, k_y + \Delta k_y), \quad (2.29)$$

the phase up to a quadratic order $\phi_q(x, y) = a_x x^2 + a_y y^2 + a_{xy} xy + b_x x + b_y y$ can be handled analytically based on the explanations of [53]. If ϕ_q is separated from the initial field

$$E(x, y) = \tilde{E}(x, y)e^{i\phi_q(x, y)}, \quad (2.30)$$

the following convolution needs to be solved in order to obtain the Fourier transformation

$$\mathcal{F}\{E(x, y)\} = \mathcal{F}\{\tilde{E}(x, y)\} * \mathcal{F}\{e^{i\phi_q(x, y)}\}. \quad (2.31)$$

Due to the fact that an analytic result exists for the Fourier transform of the quadratic phase [54], the convolution can be evaluated by a substitution of the spatial frequencies and a conventional inverse Fourier transform. While for a detailed derivation and the explicit coefficients, it is referred to [53], the overall result has the form of

$$E(\kappa_x, \kappa_y) = \alpha e^{i\tilde{\phi}'_q(\kappa_x, \kappa_y)} \mathcal{F}^{-1}\left\{\tilde{E}(k_x, k_y) e^{i\tilde{\phi}_q(k_x, k_y)}\right\}(\kappa_x, \kappa_y). \quad (2.32)$$

Here, the factor α and the quadratic phases, $\tilde{\phi}'_q(\kappa_x, \kappa_y)$ and $\tilde{\phi}_q(k_x, k_y)$, are dependent on the coefficients of the initial quadratic phase. $\mathcal{F}^{-1}\{\}\!(\kappa_x, \kappa_y)$ denotes the inverse Fourier transform with a substitution of the spatial frequencies. Dependent on the application, this reduces the required sampling for the evaluation of the Fourier transform, when the inner quadratic phase ϕ_q is smaller than the initial phase ϕ_q . The larger the curvature of the initial phase, the more efficient Equation 2.32 becomes. For high numerical apertures, the parabolic approximation of the strong spherical wave becomes inaccurate and stitching approaches will be necessary [55].

2.1.2. Transport of intensity equation

Based on the homogeneous wave equation, see Equation 2.14, the transport of intensity equation can be obtained [56]. Therefore, a paraxial monochromatic field propagating along z is assumed, which implies $k \approx k_z$. In a first step, the fast oscillating term is separated from the complex scalar field

$$E(\mathbf{r}) = \tilde{E}(\mathbf{r}) e^{ik_z z} \quad (2.33)$$

and substituted into the homogeneous wave equation

$$\nabla^2 \tilde{E}(\mathbf{r}) e^{ik_z z} + k^2 \tilde{E}(\mathbf{r}) e^{ik_z z} = 0. \quad (2.34)$$

The assumption of a slowly varying envelope leads to

$$\left| \frac{\partial^2 \tilde{E}(\mathbf{r})}{\partial z^2} \right| \ll k \left| \frac{\partial \tilde{E}(\mathbf{r})}{\partial z} \right| \quad (2.35)$$

and the Helmholtz equation can be simplified to the paraxial wave equation

$$\nabla_{\perp}^2 \tilde{E}(\mathbf{r}) + 2ik \frac{\partial \tilde{E}(\mathbf{r})}{\partial z} = 0. \quad (2.36)$$

Here, ∇_{\perp} is the lateral nabla operator. If the following approach is inserted,

$$\tilde{E}(\mathbf{r}) \propto \sqrt{I(\mathbf{r})} e^{i\phi(\mathbf{r})}, \quad (2.37)$$

where $I(\mathbf{r})$ is the intensity and $\phi(\mathbf{r})$ is the phase, and the result is separated into its real and imaginary part, the transport of phase and the transport of intensity equation are obtained. The latter is given by

$$-k \frac{\partial I(\mathbf{r})}{\partial z} = \nabla_{\perp} I(\mathbf{r}) \cdot \nabla_{\perp} \phi(\mathbf{r}) + I(\mathbf{r}) \nabla_{\perp}^2 \phi(\mathbf{r}). \quad (2.38)$$

This result connects the intensity, its gradient, the lateral gradient of the phase and its lateral Laplacian ∇_{\perp}^2 . As a consequence, the phase can be retrieved based on measurements of the intensity distribution along z of a paraxial field. This is used in Chapter 6 for the characterization of a real light source.

2.1.3. Geometrical optics

The concept of geometrical optics applies, if the wavelength becomes vanishingly small ($\lambda \rightarrow 0$) compared to the spatial scales of the considered field. According to [27, 47], such a monochromatic and scalar field traveling through a medium that also varies slowly on the scale of a wavelength can be formulated by

$$E(\mathbf{r}) = A(\mathbf{r}) e^{ik_0 S(\mathbf{r})}. \quad (2.39)$$

Here, $A(\mathbf{r})$ is the amplitude, k_0 is the free-space wavenumber and $S(\mathbf{r})$ is called the Eikonal, which is dependent on the refractive index of the medium. By inserting Equation 2.39 into the wave equation, see Equation 2.14, and applying the limit of $\lambda \rightarrow 0$, the Eikonal equation,

$$|\nabla S(\mathbf{r})|^2 = n^2(\mathbf{r}), \quad (2.40)$$

is obtained. This equation needs to be satisfied by the Eikonal, which is proportional to the phase in wave optics. Constant surfaces ($S(\mathbf{r}) = \text{constant}$) are called wavefronts, which can be determined for a specific problem by the Eikonal equation. At each point of the wavefronts, the wave vector is orthogonal to the surface. If a point of the general wave is approximated in its neighborhood by a local plane wave, its trajectory can be described by a ray that remains always perpendicular to the wavefront. As a consequence, optical systems can be efficiently analyzed by tracing rays under the outlined conditions. Especially in focal regions, the description by rays becomes inaccurate.

In this thesis, geometrical optics are used in Chapter 5 for the consideration of surface imperfections, which are much larger than a wavelength. Furthermore, the geometric-optical version of the local plane-interface approximation (LPIA) [57] is used for the combination of wave-optical propagation in free-space and ray tracing in inhomogeneous regions, such as an curved interface between two dielectric media.

2.2. Modeling of light scattering at rough surfaces

The scattering of waves at rough surfaces is of special interest in a variety of different applications in optics. Following the literature in [58, 59], a mathematical solution for the scattering problem will be outlined. In Figure 2.1, the general problem is sketched.

An incoming field distribution $\mathbf{E}_{1in}(\mathbf{r})$ is scattered at a rough interface $h(x, y)$ between two homogeneous media with refractive indices n_1 and n_2 . Dependent on the properties of the boundary, a reflected field $\mathbf{E}_{1sc}(\mathbf{r})$ and a transmitted field $\mathbf{E}_{2sc}(\mathbf{r})$ results. In principal, the scattered waves need to fulfill the wave equation under

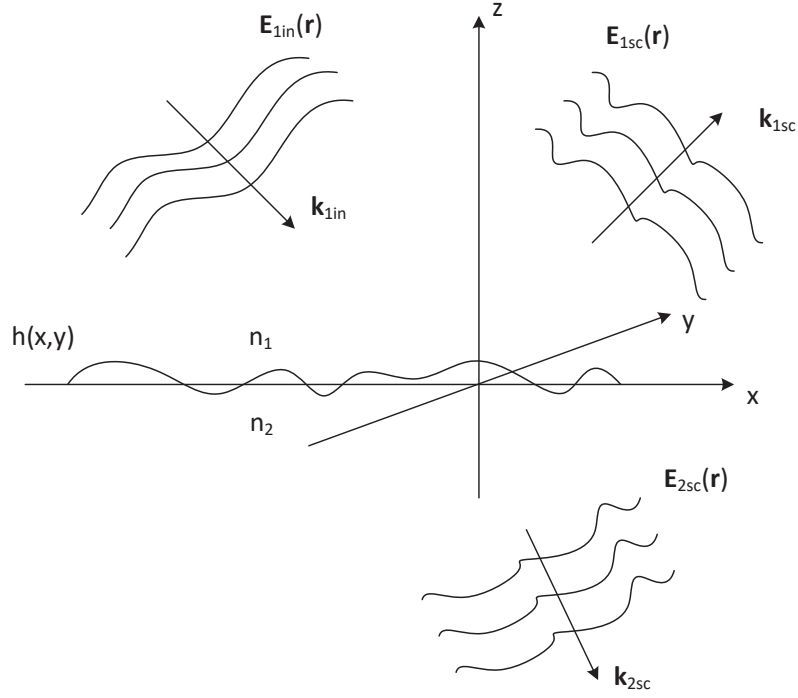


Figure 2.1.: Sketch of wave scattering at a rough interface $h(x, y)$.

certain boundary conditions, which are dependent on the properties of the rough interface. As a result of the radiation condition it follows that the field in an infinite distance of the rough surface needs to be composed of outgoing waves only. According to the previous section, the incoming electric field can be decomposed into plane waves

$$\mathbf{E}_{1in}(\mathbf{r}) = \iint \mathbf{E}_0(\mathbf{k}_{1in}) \exp(-i\mathbf{k}_{1in}\mathbf{r}) dk_{x,1in} dk_{y,1in}. \quad (2.41)$$

As a consequence, the scattering problem can be studied by considering the case of a single plane wave only. Due to the interaction at the rough interface, a scattered reflected and transmitted electric field results, which are dependent on the incoming plane wave. Again, the scattered fields can be represented by a superposition of plane waves

$$\mathbf{E}_{1sc}(\mathbf{r}, \mathbf{k}_{1in}) = \iint \mathbf{S}_r(\mathbf{k}_{1sc}, \mathbf{k}_{1in}) \mathbf{E}_0(\mathbf{k}_{1in}) \exp(-i\mathbf{k}_{1sc}\mathbf{r}) dk_{x,1sc} dk_{y,1sc}, \quad (2.42)$$

$$\mathbf{E}_{2sc}(\mathbf{r}, \mathbf{k}_{1in}) = \iint \mathbf{S}_t(\mathbf{k}_{2sc}, \mathbf{k}_{1in}) \mathbf{E}_0(\mathbf{k}_{1in}) \exp(-i\mathbf{k}_{2sc}\mathbf{r}) dk_{x,2sc} dk_{y,2sc}. \quad (2.43)$$

Here, $\mathbf{S}_r(\mathbf{k}_{1sc}, \mathbf{k}_{1in})$ and $\mathbf{S}_t(\mathbf{k}_{2sc}, \mathbf{k}_{1in})$ represents the scattering amplitude of \mathbf{k}_{1in} to \mathbf{k}_{1sc} for the reflected and \mathbf{k}_{1in} to \mathbf{k}_{2sc} for the transmitted field, respectively. In general, the scattering amplitude is dependent on the surface properties and is for two field components a 2 by 2 matrix. Finally, the scattered field distribution is obtained by superposing the scattered plane waves

$$\mathbf{E}_{1sc}(\mathbf{r}) = \iint \mathbf{E}_{1sc}(\mathbf{r}, \mathbf{k}_{1in}) dk_{x,1in} dk_{y,1in}, \quad (2.44)$$

$$\mathbf{E}_{2sc}(\mathbf{r}) = \iint \mathbf{E}_{2sc}(\mathbf{r}, \mathbf{k}_{1in}) dk_{x,1in} dk_{y,1in}. \quad (2.45)$$

The outlined approach is based on the assumption that the point of observation is not close to the rough surface. For most cases, the field far away of the interface is of interest and therefore, this limitation is here not of practical importance. In general, there exist a huge variety of different strategies and models for calculating the scattering amplitude. In [60], an overview based on made assumptions and approximations is given. Without going into detail, two fundamental models will be introduced in the following, which are of interest for this work in Chapter 6.

Small perturbation method

The small perturbation method (SPM), or Rayleigh-Rice vector perturbation theory (VPT), assumes that the original field distribution is not distorted significantly by the scattering at the rough surface, so the surface height variation is assumed to be small. Based on an idea of Rayleigh [61] and Rice [62], the scattering amplitude is approximated by a Taylor-Volterra expansion in surface elevation

$$\begin{aligned} \mathbf{S}(\mathbf{k}_{sc}, \mathbf{k}_{in}) &= \mathbf{V}_0(\mathbf{k}_{sc})\delta(\mathbf{k}_{sc} - \mathbf{k}_{in}) - i\mathbf{C}_1(\mathbf{k}_{sc}, \mathbf{k}_{in})h(\mathbf{k}_{sc} - \mathbf{k}_{in}) \\ &\quad - \int \mathbf{C}_2(\mathbf{k}_{sc}, \mathbf{k}_{in}, \nu)h(\mathbf{k}_{sc} - 2\pi\nu)h(2\pi\nu - \mathbf{k}_{in})d\nu + \dots, \end{aligned} \quad (2.46)$$

where the first term describes the specular reflection with the coefficient matrix $\mathbf{V}_0(\mathbf{k}_{sc})$. $\mathbf{C}_1(\mathbf{k}_{sc}, \mathbf{k}_{in})$ and $\mathbf{C}_2(\mathbf{k}_{sc}, \mathbf{k}_{in}, \nu)$ are the coefficient matrices in first- and second-order. $h(\nu)$ corresponds to the Fourier transform of the surface height and is connected to the power spectral density (PSD) of the surface profile by

$$\text{PSD}(\nu_x, \nu_y) = \lim_{A \rightarrow \infty} \left| \frac{1}{A} h(\nu_x, \nu_y) \right|^2, \quad (2.47)$$

where A is the area of the surface. This is of special interest for application because the PSD of a surface profile is easier accessible than the accurate measurement of the full surface profile. Due to the absolute value, the phase information is not included if the PSD is used. Dependent on the boundary conditions of the particular scattering problem, the coefficient matrices can be calculated. For a detailed derivation, it is referred to [58].

Tangent plane approximation

The tangent plane approximation is based on the evaluation of the Kirchhoff integral taking the varying local surface normal into account [63]. In contrast to the SPM, the TPA is valid for smooth surface curvatures with local radii of curvature $r_c \gg \lambda$. Comparable to geometrical optics, it is assumed that at each point of the rough surface the incident wave is reflected at the locally tangent plane according to the Fresnel equations. The scattering amplitude can be formulated by

$$\mathbf{S}(\mathbf{k}_{sc}, \mathbf{k}_{in}) = \iint \mathbf{K}(\mathbf{k}_{in}, \nabla h(x, y)) e^{-i(k_{z,sc} - k_{z,in})h(x, y)} \cdot e^{-i((k_{x,sc} - k_{x,in})x + (k_{y,sc} - k_{y,in})y)} dx dy, \quad (2.48)$$

where $\mathbf{K}(\mathbf{k}_{in}, \nabla h(x, y))$ is the Kirchhoff matrix, which is given for certain boundary conditions in [58].

2.3. Description of surfaces

The description of surfaces by an analytic, two-dimensional function $f(x, y)$ has an important role throughout the simulation and modeling of optical systems. Based on a suitable set of functions, the surface is efficiently integrated into the design by ray tracing and its parameters can be adapted during the optimization process according to different strategies [64]. In contrast to simple, spherical components, the choice of an adequate description becomes far from being trivial for aspherical, and even more so for freeform components [65].

Apart from the usage during the design process, analytic descriptions can be applied for the approximation of discrete two-dimensional data, such as measurements of a surface profile. This becomes of special interest for the integration of manufactured components into the simulation of optical systems, which is part of this thesis in Chapter 5. The goal is to find a continuous function that approximates a given set of M data points $z_i(x_i, y_i) \in \mathbb{R}$ in an appropriate way

$$f(x_i, y_i) \approx z_i, \quad i = 1, 2, \dots, M. \quad (2.49)$$

If $f(x, y)$ is represented by a linear combination of a set of functions $\phi_n(x, y)$, which will be discussed within the next sections,

$$f(x, y) = \sum_{n=1}^N c_n \phi_n(x, y), \quad (2.50)$$

the resultant system of linear equations can be approximated for the typical case $N < M$ by using least squares [66]

$$\mathbf{A}\mathbf{c} = \mathbf{z}, \quad (2.51)$$

$$\mathbf{c} = (\mathbf{A}^\top \mathbf{A})^{-1} \mathbf{A}^\top \mathbf{z}. \quad (2.52)$$

Here, \mathbf{A} is a $M \times N$ matrix, which entries are given by $A_{in} = \phi_n(x_i, y_i)$, \mathbf{c} is

the vector of weighting coefficients c_n and \mathbf{z} consists of the data points z_i . In the following sections, two approaches for the description of surfaces based on different set of functions $\phi_n(x, y)$ will be introduced and discussed, which are of interest for this work.

2.3.1. Polynomial expansions

One option is the description of a surface by a set of a two-dimensional polynomial expansion F_{nm} , with orders $n = 0, 1, \dots, N$ and $m = 0, 1, \dots, M$,

$$f(x, y) = \sum_{m=0}^M \sum_{n=0}^N c_{nm} F_{nm}(\bar{x}, \bar{y}), \quad (2.53)$$

which is typically formulated for normalized coordinates \bar{x} and \bar{y} . In the context of optical freeform surfaces, an overview of different polynomial expansions, and their corresponding properties, such as orthogonality, is given in [67].

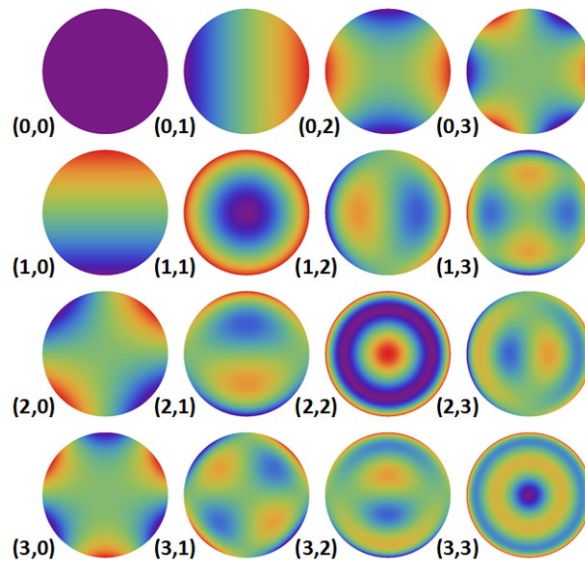


Figure 2.2.: Comparison of the Zernike polynomials for different orders (n, m) on a circular aperture [67].

As an example, the first orders of the Zernike polynomials are shown in Figure 2.2. These functions are typically defined in polar coordinates and are used in optics not

only for the modeling of freeform surfaces but also for the description of wavefront deviations because of their direct relation to primary aberrations [56]. For a constant weighting, they are orthogonal functions within the unit circle.

2.3.2. Radial basis functions

An alternative approach is the description of surfaces by non-orthogonal, lateral shifted, radial basis functions (RBFs). In contrast to a description by polynomials, RBFs account for more local features and an arbitrary shape of the boundary [65]. Based on [68], $f(x, y)$ is composed by a linear combination of N radial symmetric functions, which are distributed on a certain grid (x_n, y_n) ,

$$f(x, y) = \sum_{n=1}^N c_n \phi_{\text{RBF}}(x - x_n, y - y_n, \epsilon_n). \quad (2.54)$$

Here, ϵ accounts for the shape of the RBF and the coefficient c can be interpreted as its height. The approach is sketched in Figure 2.3.

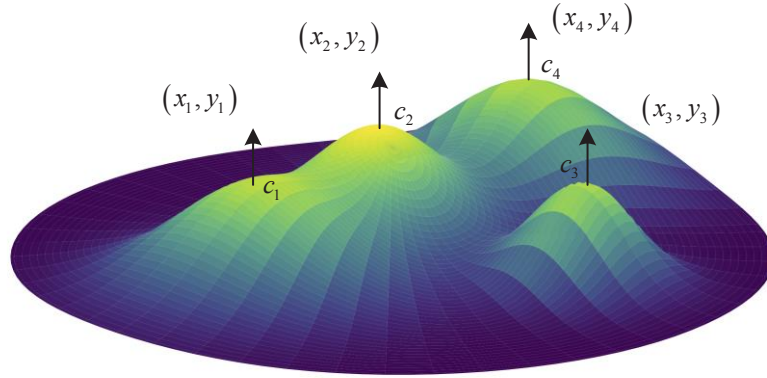


Figure 2.3.: Example of a surface described by RBFs. Four radial symmetric functions with height c_n are laterally distributed on a statistical grid (x_n, y_n) .

One possible choice for the radial symmetric function is the Gaussian function with a constant shape factor

$$\phi_n(x, y) = \exp(-\epsilon^2((x - x_n)^2 + (y - y_n)^2)). \quad (2.55)$$

Alternative representations are multiquadric or Wendland functions [69], and certain procedures for orthogonalization exists [70]. For the lateral distribution of the RBFs, often cartesian, polar, hexagonal or Fibonacci grids are used [71]. If the number of basis functions is sufficiently large, also a statistical distribution is possible [72]. Within the masters thesis of the author [73], a suitable set of parameters is investigated and it is shown that for the application on manufactured freeform surfaces, the combination of Gaussian functions, which are distributed on a Fibonacci grid, gives a decent result. Furthermore, a strategy for the optimization of the shape factor for a certain set of functions is introduced. Following this work, first approaches for a more adaptive distribution of the RBFs in the context of optical surfaces were researched [74].

3. Concept for a holistic simulation of optical systems demonstrated on a thin-disk multipass amplifier

For many years the design of optical systems by a geometric-optical description of a linear arrangement of lenses, mirrors or prisms was satisfactory and lead to an accurate result. Today, physical effects, as diffraction, coherence, polarization or scattering, need to be included into the simulation for many modern optical systems. Further, an agreement with the experimental measurement is often only achievable by a consideration of real, manufactured components, signal processing and digital optics.

The scope and motivation of this thesis are to develop and analyze new approaches, introduced and discussed within the following chapters, leading to a more holistic simulation of such systems. The prerequisite and basement for this purpose is a framework or software platform that allows for the description, simulation and optimization in a modular environment. A possibility would be to select one of the comprehensive, available optical design or simulation software [22–24]. To include new approaches, the development of additional extensions, limited by the specific, predefined interfaces, would be necessary. Based on the individual scope of the application, for example, imaging or illumination, the optimal selection of the software varies. A complex link and connection between several toolboxes would be necessary in order to address the wide range of aspects of a more holistic description. Therefore, and to allow for a manageable and fully transparent solution, a new simulation framework based on Python 3 [75] was created, so new approaches can be implemented, used and analyzed with a high flexibility. It is clear that within this work the almost unlimited number of different modules and effects to describe all kind of optical systems cannot be covered. Therefore, the developed toolbox is exemplary

filled for several systems, focusing on different aspects. Four topics are selected that are, from the authors point of view, relevant for a more holistic description. Physical effects, real light sources, real manufactured components and systems, and signal processing are addressed within this thesis and further enhanced by several new approaches.

	physical effects	real light sources	real manufactured components	signal processing
Trumpf disk amplifier (Chapter 3)	x		x	x
VISTEL freeform system (Chapter 5)			x	
HOROS scattering setup (Chapter 6)	x	x	x	x

Table 3.1.: Overview of selected key aspects, addressed in the example systems of this thesis.

In Table 3.1, an overview is given of selected key aspects, addressed in the studied systems of this thesis.

In this chapter, the concept of a modular simulation framework for a more holistic simulation is evaluated. For a better demonstration and to derive general requirements on such a toolbox, an example system is introduced in the next section. Here, a disk amplifier, based on a development by the Trumpf Laser GmbH, Schramberg [3, 44, 76], is chosen. The challenges for a comprehensive simulation of this systems are the handling of the complex arrangement, the modeling of the physical effects, as gain, absorption and thermal lensing, at the active medium and the diffraction calculation between the individual elements. Based on this system, the structure of the platform, the layout of the individual modules and their interfaces and connections with each other are discussed. In Section 3.2, the specific modules for the simulation of the disk amplifier are derived and made assumptions are discussed. The results, based on the developed framework, are presented in the last section together with a tolerancing analysis of the system, demonstrating the applicability of such a simulation.

3.1. General concept

The goal of the example system is to amplify a laser beam by multiple interactions with an active medium for high power applications, while preserving a superior beam quality. In contrast to a classical laser resonator, the optical path of the light is not replicated in a cavity and therefore, special in- and out-coupling elements, as for example saturable absorbers or Pockels cells [77], are not necessary. The incoming laser beam with a wavelength of $\lambda = 1030 \text{ nm}$ is coupled into the system by three mirrors in order to hit the active medium under a certain angle. To keep thermal-lensing as small as possible, a thin disk geometry is used here. The amplifier system is composed by an array of several mirror pairs. Each of these pairs is aligned in order to return the beam back to the disk, so it is reflected onto the following mirror pair. After several interactions with the active medium, the amplified laser beam leaves the system by a simple plane mirror and can be further guided to its place of application.

The geometrical layout of the disk amplifier is shown in Figure 3.1. The corresponding arrangement of the mirror array with the sequence of interactions is illustrated in Figure 3.2.

Before discussing the necessary modules for a description of the multipass amplifier, several general requirements on the simulation framework are highlighted. Keeping the complex arrangement of the mirror array in mind, a structured definition and flexible handling of the used coordinate systems is mandatory, especially for a comprehensive tolerancing analysis. Derived from existing software projects [22, 78, 79], the coordinate system is divided into one global and several, module dependent, local systems. While the modules, as for example the light source or optical components, are arranged in the global coordinate system, the structure, corresponding surfaces and effects within the individual module are defined and described in their local systems. A transformation between different systems is realized by specifying their origin and rotation matrix relative to the global coordinate system. For the studied example system, this means that the components, as i.e. the mirrors or the disk, are oriented in the global system, while the corresponding physical models and interactions are independently defined in the relative systems.

Another central aspect is the description of the light. For a more holistic simulation

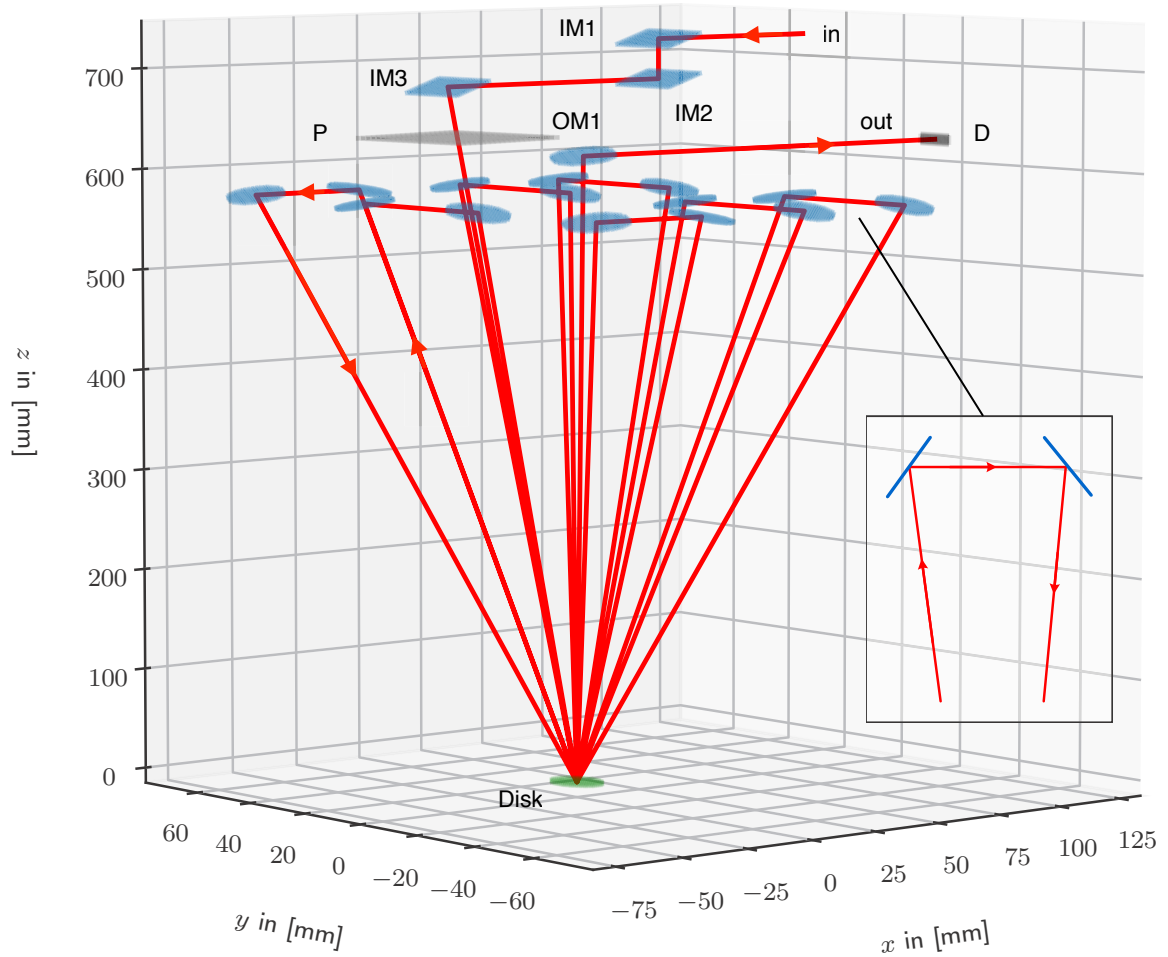


Figure 3.1.: Geometrical layout of the disk amplifier system. The laser beam is in-coupled by three mirrors (blue, IM1-IM3) and its polarization is adjusted (grey, P1). By an array of fourteen mirrors (blue), the beam is reflected several times back to the disk (green, Disk). The amplified light is out-coupled by a mirror (OM1) and evaluated at the detector (grey, D). The scaling along x , y and z is different. As a consequence, the reflection at the mirrors seems to be odd.

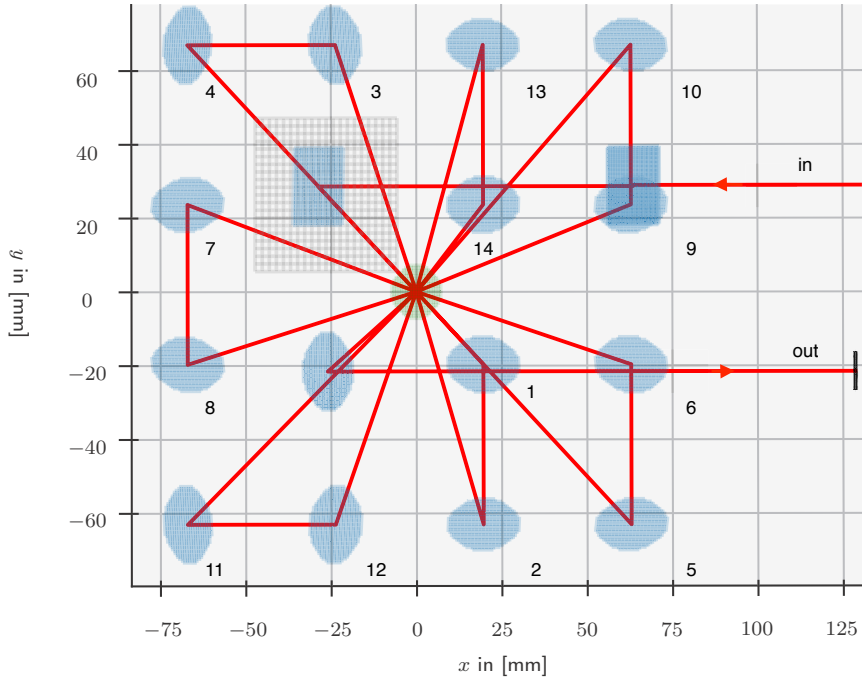


Figure 3.2.: Arrangement of the mirror array in a view along z . The number of the mirrors (1-14) represents the sequence of reflections.

of optical systems, the restriction to a single numerical description, as for example rays or Gaussian beams [80], is not expedient and efficient. Dependent on the boundary conditions of the application and the necessary modeling depth of the problem, the framework should allow for the most suitable light description and to combine them. As a simple example, for simulating a classical microscopic objective lens, typically a hybrid-approach is used [81]. Rays are traced to get the wavefront in the exit pupil of the system before the light is further propagated into the image plane taking wave-optics into account. As a consequence the conversion between specific approaches, i.e., monochromatic, electrical fields to rays or into Gaussian beams [82,83], needs to be realized, keeping the physical and numerical restrictions in mind. For the amplifier system, the light is described by a composition of coherent, monochromatic and linear polarized electromagnetic waves, which are introduced in Section 2.1

$$\begin{pmatrix} E_x \\ E_y \end{pmatrix}(\mathbf{r}, t) = \begin{pmatrix} E_{x0}(\mathbf{r}) \cdot \exp(i\phi(\mathbf{r}) - i\omega t) \\ E_{y0}(\mathbf{r}) \cdot \exp(i\phi(\mathbf{r}) - i\omega t) \end{pmatrix}. \quad (3.1)$$

The time-dependency is neglected for further steps. The connection between the optical components is realized by Fourier-based free-space propagation based on the angular spectrum of plane waves [84]. To allow for an efficient and flexible sampling, the chirp z-transform is used and the quadratic and linear phases are handled analytically. Details are given and discussed in Section 2.1. In order to simulate the full system, the individual modules and propagators need to be connected and a calculation path and sequence need to be defined.

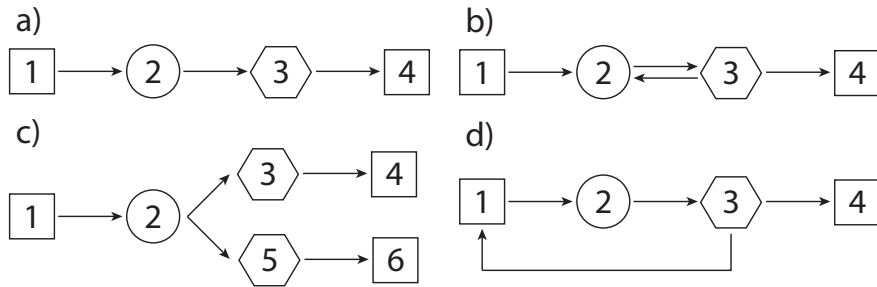


Figure 3.3.: Exemplary arrangements and interactions between different modules: a) sequential setup, b) simple interaction between module two and three, i.e., multiple reflections, c) beamsplitter and d) resonator.

For example, if a simple sequential arrangement is considered, see Figure 3.3 a), the corresponding path of calculation is straight forward. First, evaluating the code of module one. Second, propagating from module one to module two. Third, evaluating the next module, and so on. But the more complex the system gets the more important is the concept of scheduling the calculation path. Several further examples are made in Figure 3.3 that can be realized by the simulation framework and are used within the following examples. In Figure 3.4, the schematic arrangement of the disk amplifier simulation is shown.

The in-coupling path of the system is described by five modules, the light source, three mirrors and a linear polarizer, that are connected by free-space propagation in a linear arrangement. The calculation path of the actual amplifier system corresponds to a loop over the propagation between varying array mirrors and the disk. An important aspect to consider here, are the intensity-dependent saturation effects at the active medium, which will be discussed in detail during the next section. As a consequence for the simulation, the intensity at the disk needs to be continuously updated until a steady-state result is achieved. This procedure is comparable to the approach of Fox and Li [85, 86]. After the linear out-coupling path, the final field

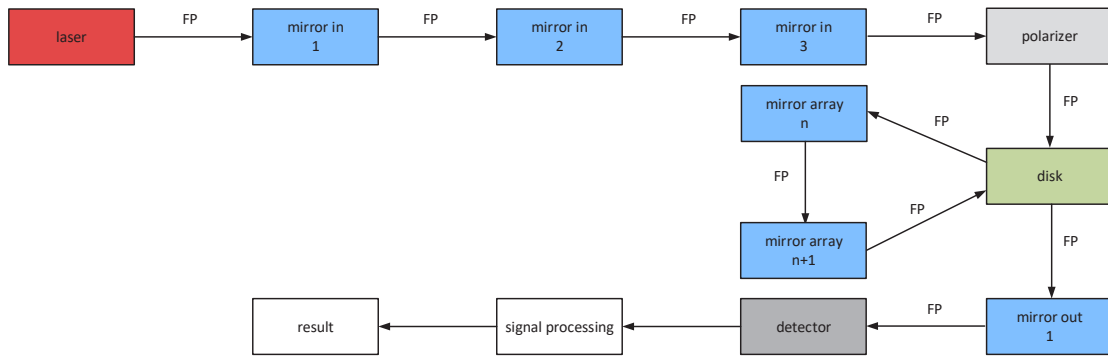


Figure 3.4.: Schematic arrangement of the thin-disk multipass amplifier simulation. The individual optical components are connected by free-space propagation FP. Only one mirror pair ($n, n + 1$) is shown.

is obtained at the detector. Signal processing, as for example the evaluation of the beam quality, is included into the simulation by the final module.

From a viewpoint of implementation, the object-oriented, high-level language Python 3 is used. Compared to the compiled programming language C++ [87], the simplicity for the development is preferred over runtime here. By certain extensions the speed of the individual algorithms can be further improved [88,89]. Another aspect is the large community of Python and the availability of interfaces to hardware and software. For example, the COM- or DDE-connection to Zemax OpticStudio [22] can be used to verify certain results [90].

3.2. Description of the modules

In general, all the simulation algorithms and descriptions of the framework are located and ordered in different modules. As shown in the previous section, the system to model is then composed by a suitable arrangement. To allow for an accurate and flexible connection and interaction, all the modules have to fulfill some predefined requirements. Independent if they represent optical components, propagators or software processing. The schematic layout of a module and its predefined sub-classes are sketched in Figure 3.5.

Simplified, a certain input signal enters the module by a defined entrance port, is

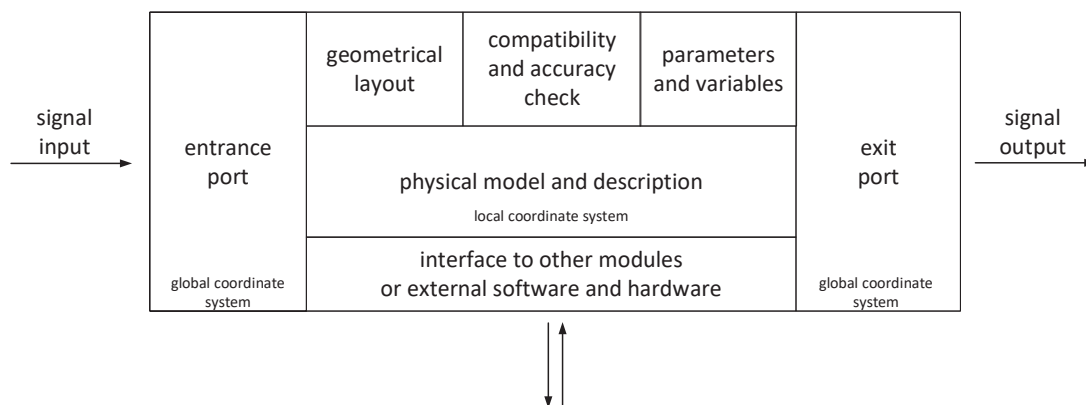


Figure 3.5.: Schematic structure of a module, such as a mirror. Dependent on the actual content, some functions may not be used.

then modified by some algorithms and exits the component by another interface, called exit port. Before some detailed examples for the multipass amplifier are given, the individual sub-functions and interfaces are discussed briefly. The entrance and exit ports are the main interfaces to adjacent modules. They are defined in the global coordinate system by their position and rotation matrix. The type of the interface can be defined dependent on the signal or light description. For example, if monochromatic electrical fields are used, usually, the entrance and exit ports are defined to be plane surfaces, so FFT-based propagation algorithms can be used. If the light is described by rays, the interfaces of the component, i.e., a lens, have typically the same shape as its first and last surface. Further, the actual position, its orientation and aperture can be defined in relation to the previous and next components by a pilot ray. For example, dependent on the position of the previous exit port, the front or the back surface of a lens are used as an input interface. Or, if the next component lies on the same hemisphere as the previous one, the reflected light is evaluated. Also multiple entrance and exit ports are possible, which are necessary for describing beam splitters or interference of multiple fields at a detector. The actual core of each module, the implementation of the physical model or algorithm, is defined in the local coordinate system relative to the entrance and exit ports. With respect to the selected definition of the signal and the required accuracy, multiple descriptions can be implemented based on different approximations and assumptions. The correct selection of the model and its parameters is ensured by a compatibility and accuracy check. For the different propagators, the accuracy of the model and the correct sampling can be estimated by a comparison

to analytical results or by an evaluation with a simplified example [21, 91]. Another sub-class of the module structure, is the definition of parameters, as for example selected materials or surface descriptions, which can be kept variable for simple optimization tasks. Environmental influences, as a change in temperature or pressure, or interactions between different modules, which are not directly considered by the signal, are taken into account by an additional interface function. To arrange and illustrate a component within the system, a certain layout function is defined. Apart from the geometrical layout of the module, the light path through most optical components can be sketched by a ray-based description. A more abstract and individual visualization is needed for signal processing algorithms. It is clear that, dependent on the actual content of the module, some functions of the predefined module-class may not be used. For example, a typical light source has an output signal only and therefore no entrance port.

The modules, used to describe the disk amplifier system, are presented in the following.

Light source

As a light source, a fully coherent, monochromatic ($\lambda = 1030$ nm), paraxial Gaussian beam [47] is defined with a waist radius of $w_0 = 1.5$ mm on a rectangular shaped, 15 mm by 15 mm, aperture

$$\mathbf{E}(\mathbf{r}) = \mathbf{E}_0 \cdot \frac{w_0}{w(z)} \cdot e^{-\frac{x^2+y^2}{w(z)^2}} \cdot e^{-ik\frac{x^2+y^2}{2R(z)}} \cdot e^{-i(kz-\zeta(z))}, \quad (3.2)$$

$$w(z) = w_0 \sqrt{1 + \left(\frac{z}{z_R}\right)^2}, \quad (3.3)$$

$$R(z) = z \left(1 + \left(\frac{z_R}{z}\right)^2\right), \quad (3.4)$$

$$\zeta(z) = \arctan\left(\frac{z}{z_R}\right), \quad (3.5)$$

$$z_R = \frac{\pi w_0^2}{\lambda}, \quad (3.6)$$

Here, \mathbf{E}_0 is the electrical field vector at the origin, z_R is the Rayleigh range and

$\zeta(z)$ is the Gouy phase. The beam is defined at $z = 0$ and is assumed to be linear polarized. The exit port corresponds to a plane surface and its surface normal points along the propagation direction of the beam. For the particular example, the lateral discrete sampling is chosen to be 255 by 255 points.

Mirror

Eighteen components of the system are plane mirrors. Each of the circular array elements has a size of 20 mm in diameter. The rectangular input mirrors have a size of 20 mm by 15 mm. Often, the aperture of a component is not fully illuminated by the light. To allow for an efficient evaluation of the module, this is taken into account. Therefore, the position of the entrance port, a plane surface, is determined by calculating the intersection with the pilot ray and the effective size of the surface is adapted accordingly to the previous propagation step. The orientation of the entrance port is chosen to be parallel to the exit port of the previous component in order to use conventional FFT-based free-space propagators. The residual propagation step to the tilted mirror surface can then be evaluated by the algorithm introduced in Chapter 4. At the mirror surfaces, an aperture mask is applied dependent on its actual size and the coating, if available, or the Fresnel equations are applied. The influence by the actual surface shape can be included by the LPIA introduced in Section 2.1.3 or by alternative propagation algorithms [92–94]. Dependent on the application, also the propagation steps to the tilted plane can be included here. The final exit port, a plane surface, is then determined according to the law of reflection. In addition, a ray-based modeling can be used for the assembling and illustration. Therefore, simply the intersection points with the mirror surface are calculated and the law of reflection is applied.

Polarizer

In principle, the polarizer corresponds to a plane plate. The input field enters the module at the entrance port, which is defined at the corresponding front plane of the plate and an aperture filter is applied on the amplitude. Afterwards, the coating, if available, or the Fresnel equations are evaluated for the first interface between two media and the field is propagated through the homogeneous medium of the plate. Before the field exits the component at the rear surface, the coating is evaluated

once more. A geometric-optical solution by ray tracing is straight forward and can be used for layout purposes. For the impact on the polarization of the electrical field vector, the Jones calculus is used [95]

$$\mathbf{E}_{out}(\mathbf{r}) = \mathbf{J}_{lp}(\theta)\mathbf{E}_{in}(\mathbf{r}) = \begin{pmatrix} \cos^2(\theta) & \cos(\theta)\sin(\theta) \\ \cos(\theta)\sin(\theta) & \sin^2(\theta) \end{pmatrix} \mathbf{E}_{in}(\mathbf{r}), \quad (3.7)$$

where \mathbf{J}_{lp} is the Jones matrix for a linear polarizer rotated by a certain angle θ . If the light is not fully polarized the Mueller calculus needs to be used instead [96].

Active disk

The active medium of the amplifier system has the geometry of a thin disk to minimize thermal lensing. The material is assumed to be Yb:YAG. In Figure 3.6, the layout of the description scheme is shown. In principle, the disk corresponds to plane plate with a curved reflective back surface. The effects of the active medium, which is assumed to be polarization-independent, can be separated into gain, absorption and an additional phase because of thermal effects. Due to the minor thickness $d = 1$ mm of the disk and large radii of curvature, a thin element approximation is made and all effects are assumed to take place in a single plane. The gain factor at the disk $\mathbf{r} = (x_D, y_D)$ is described by the classical formula [97]

$$g(\mathbf{r}) = \frac{g_0}{1 + \frac{I_D(\mathbf{r})}{I_{sat}}}. \quad (3.8)$$

Here, g_0 is the small signal gain, I_{sat} is the saturation intensity and $I_D(\mathbf{r})$ is the total intensity at the disk. For an initial guess, the total intensity distribution at the disk is assumed to be the input intensity times the number of interactions with the active medium. As described in Section 3.1, this value is continuously updated after each run, until a saturation of the output power is achieved. In addition to the gain, a part of the energy is absorbed within the disk medium. This is taken into account by the absorption coefficient α . According to the law of Lambert-Beer [98] and by including the thermal effects of the deformed disk as an additional phase ϕ_{th} , this leads to

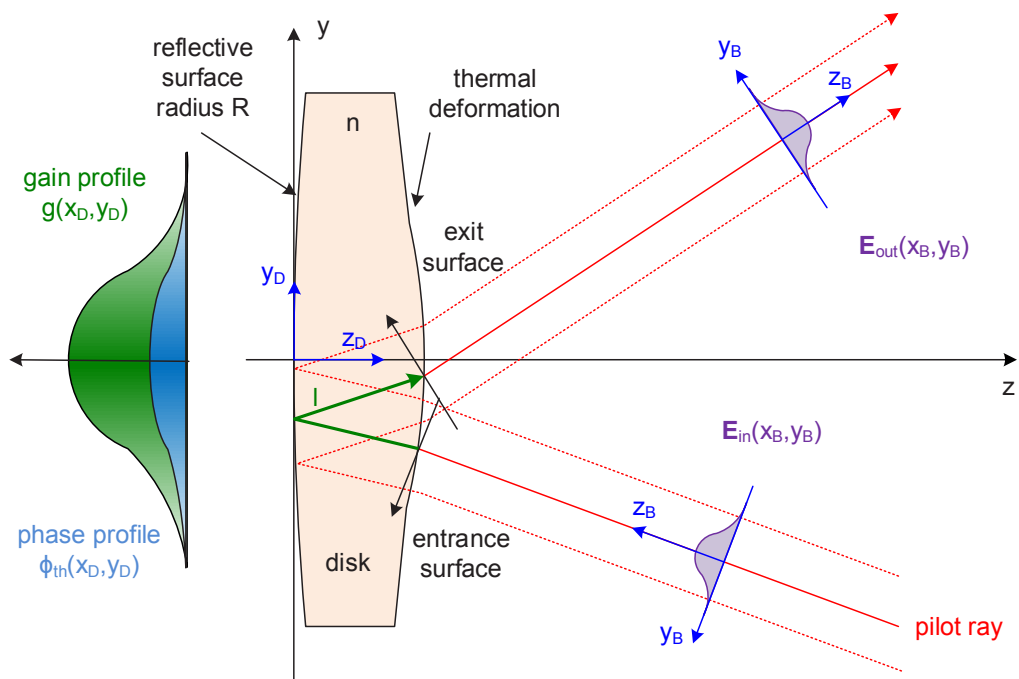


Figure 3.6.: Sketch of the disk component in the global coordinate system (x, y, z) . The local coordinate system of the disk is (x_D, y_D, z_D) and of the respective beam is (x_B, y_B, z_B) .

$$\mathbf{E}_{out}(\mathbf{r}) = \mathbf{E}_{in}(\mathbf{r}) \cdot \sqrt{e^{gl}} \cdot \sqrt{e^{-\alpha l}} \cdot e^{-ik\phi_{th}}, \quad (3.9)$$

where l is the total path length through the disc. The thermal heating of the disk leads to a deformation and a locally dependent change in refractive index. The former is included by the additional phase and empirically determined by fitting measured data with, i.e., the descriptions introduced in Section 2.3. The specific set of parameters used for the individual simulation are given in the results in Section 3.3.

Detector

While in a final setup the output of the amplifier system is used for material processing, in a first step the beam is evaluated at a 10 mm by 10 mm detector. Therefore, the input signal is discretized and sampled according to its specifications. Also the response function of the appropriate detector can be taken into account here.

Signal processing

One motivation for the comprehensive simulation of the disk amplifier system is the evaluation of the beam quality dependent on a variable set of parameters. Typically, in laser applications the M^2 factor is used as a quantitative measure [99]. It is defined by

$$M^2 = \sqrt{\left(\frac{\pi}{\lambda}\right)^2 \det \mathbf{P}}, \quad (3.10)$$

where $\det \mathbf{P}$ is the determinant of the variance or second-moment matrix. The explicit angular moments are calculated by the FFT according to [100]. While this algorithm is based on the electrical field, in the experiment only the intensity can be directly measured. In principle, it is also possible to include the measurement of the divergence [99] or a reconstruction procedure of the phase and its influences into the simulation here.

3.3. Results

In this section, the results of the disk multipass amplifier simulation are presented. First, the output distribution after propagating through the mirror array is compared to the field of the light source without taking the effects of the active medium into account. Second, the impact of the gain, the absorption and thermal lensing at the disk is analyzed in steady-state mode and the change of the beams waist along the propagation distance is evaluated for different parameter sets. In a last step, a comprehensive tolerancing analysis of the array adjustment is performed and the impact on the final beam quality and the intensity at the disk is displayed.

For reasons of confidentiality, the simulation of the system is based on arbitrary parameters. Further, the actual geometry is changed compared to the assembled system. Therefore, the comparison with the experiment is not part of this thesis, even though the verification of the results was successfully realized.

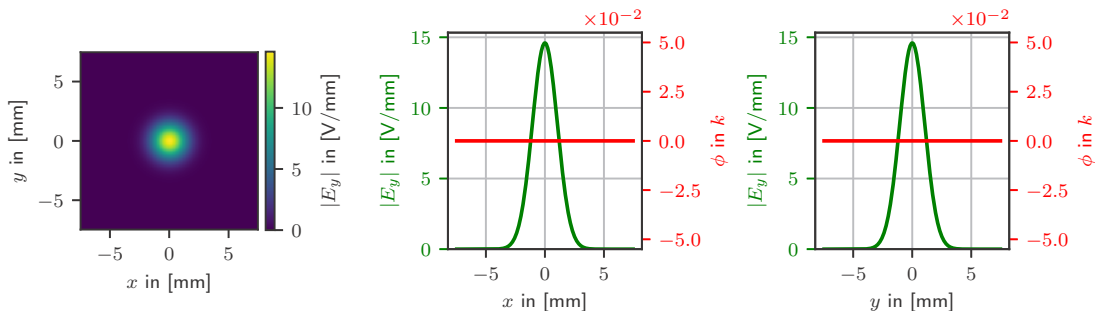


Figure 3.7.: Electrical field distribution of the input Gaussian beam and corresponding cross-sections. The waist radius is $w_0 = 1.5$ mm and the total power is $P = 1$ W. The beam is linear polarized along the y -axis, so only $|E_y|$ is shown. The wavelength is $\lambda = 1030$ nm.

In Figure 3.7, the distribution of the input field is shown. The beam is defined according to the specification in Section 3.2 and it is normalized to a power of $P = 1$ W. The phase of the field is constant because the beam is defined in its waist. The simulated light distribution, intensity and phase, after the propagation through the array system are displayed in Figure 3.8. Without any gain effects and a plane, reflective rear surface of the disc, the beam is diverging with the propagation distance. As a consequence, the lateral waist radius is increased in comparison to

the input field and a nearly spherical, diverging wavefront is observed. Further, the smooth shape of the amplitude and phase of the beam is slightly affected due to edge diffraction at the variety of mirror apertures and therefore, the overall quality of the Gaussian beam is decreased to an M^2 factor of 1.24. Also the total power of the beam is decreased to $P = 0.85$ W. The orientation of the linear polarization has changed due to the reflections in different directions.

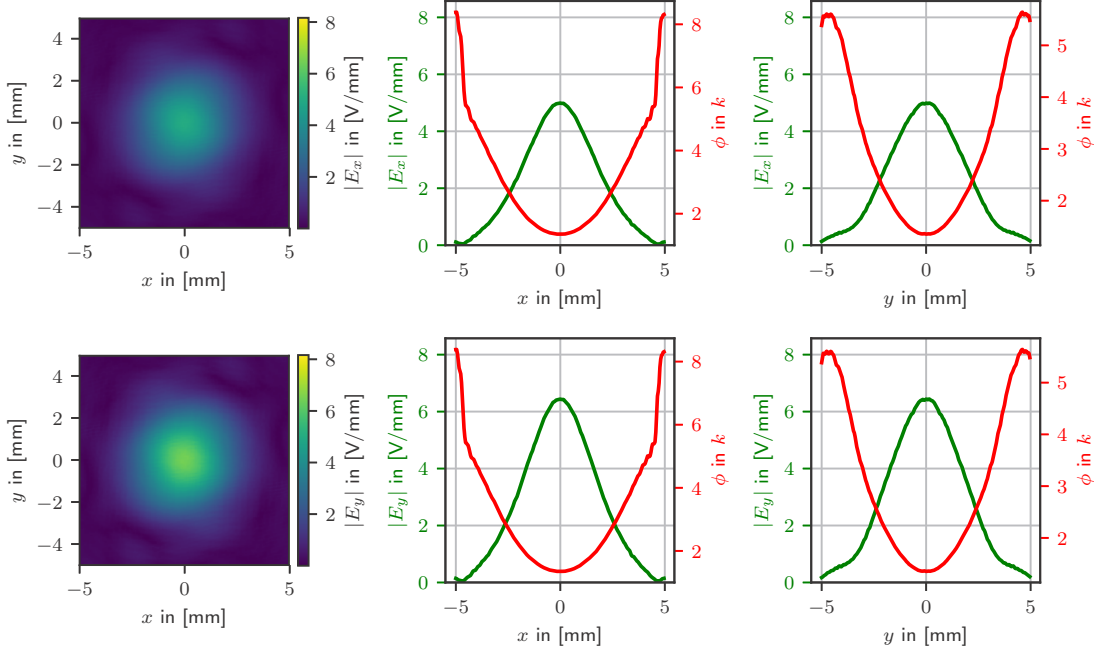


Figure 3.8.: Electrical field distribution of the output beam and corresponding cross-sections. Instead of the thin disc, a plane mirror is used here. In the upper row, the component $|E_x|$, while in the lower row, the component $|E_y|$ is shown. The waist radius is $w = 2.6$ mm and the total power is $P = 0.85$ W. The wavelength is $\lambda = 1030$ nm.

In a next step, the impact of the active medium is included into the simulation. For a first demonstration, the radius of curvature of the rear surface is assumed to be $R = 100$ m. According to the used material, the small signal gain is set to $g_0 = 1.5 \text{ cm}^{-1}$ and the absorption coefficient to $\alpha = 0.2 \text{ cm}^{-1}$. The saturation intensity is set to $I_{sat} = 50 \text{ MW m}^{-2}$. The empirical additional phase is shown in Figure 3.11. As discussed in Section 3.1, the overall simulation of the system has to be repeated with an updated total intensity at the disk until the output power is constant. For the example configuration, the convergence of the relative difference between the output power of adjacent iterations is plotted in Figure 3.9.

After $N = 7$ iterations, the change in power is below 10^{-4} % rms and the system is assumed to be in steady-state.

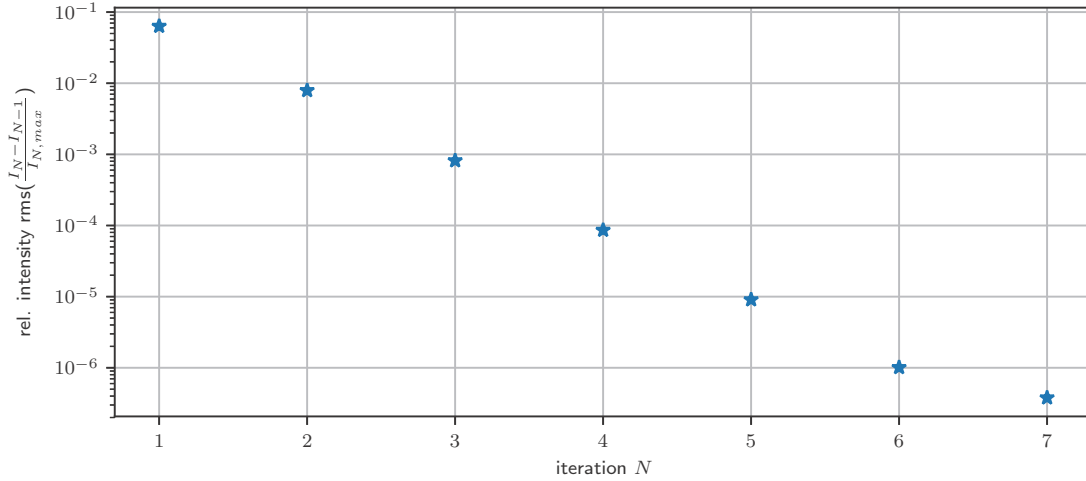


Figure 3.9.: Convergence of the relative change of the output intensity compared to the previous iteration N .

In Figure 3.10, the amplified beam is shown. In total, an increase in power by nearly a factor of six is achieved. Compared to the ideal Gaussian input beam, the quality of the beam is decreased to an M^2 factor of 1.18. One additional reason for the degradation is the usage of the curved, reflective disk surface under an oblique angle and the resulting astigmatism. The influence of edge diffraction at the components apertures is reduced due to the limited divergence of the beam and the reduced waist radius. To analyze the impact of the gain and the phase at the disk on the profile of the beam in more detail, the corresponding cross-sections are plotted in Figure 3.11.

Due to the higher intensity in the center of the disk and the corresponding saturation effects, the gain in this area is lower. Related to the waist radius of the beam, this leads to a broadening at each interaction. Furthermore, the profile of the beam is affected by the additional empirical phase. To partly compensate these effects, a spherical rear surface of the disk is selected. For different parameters and configurations, the change of the beams waist radius with the propagation distance is shown in Figure 3.12. While the beam is still diverging for the plane disk, a nearly constant waist radius can be achieved by a suitable selection of the radius of curvature.

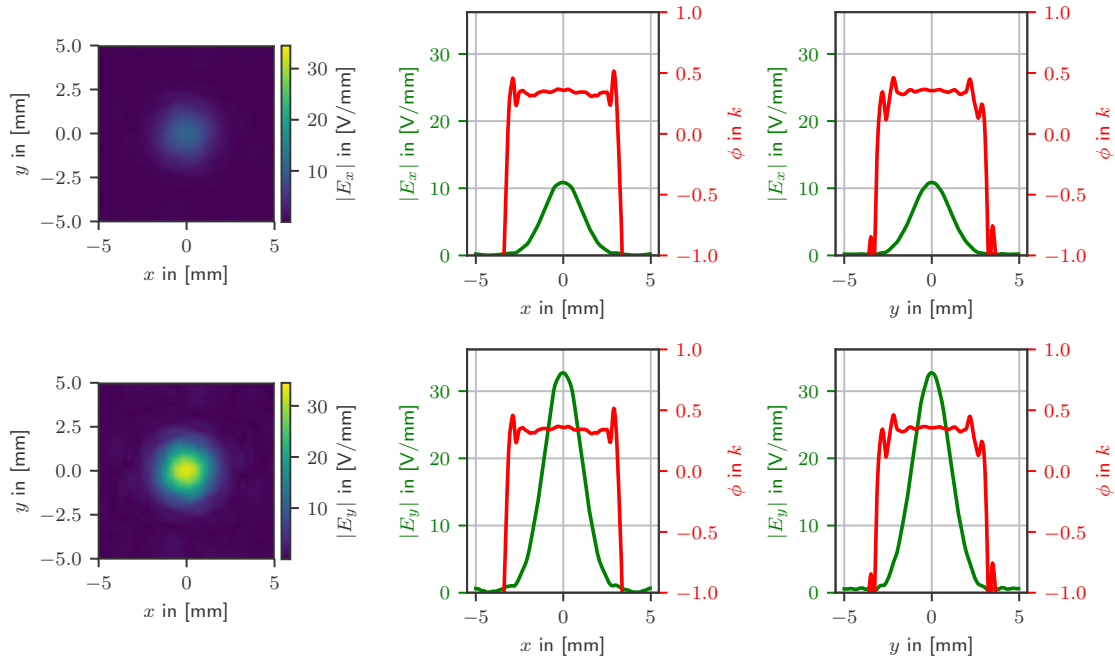


Figure 3.10.: Electrical field distribution of the output beam and corresponding cross-sections. The disk has a curved rear surface ($R = 100$ m) and the effects of the active medium are included. In the upper row, the component $|E_x|$, while in the lower row, the component $|E_y|$ is shown. The waist radius is $w = 1.5$ mm and the total power is $P = 5.97$ W. The wavelength is $\lambda = 1030$ nm.

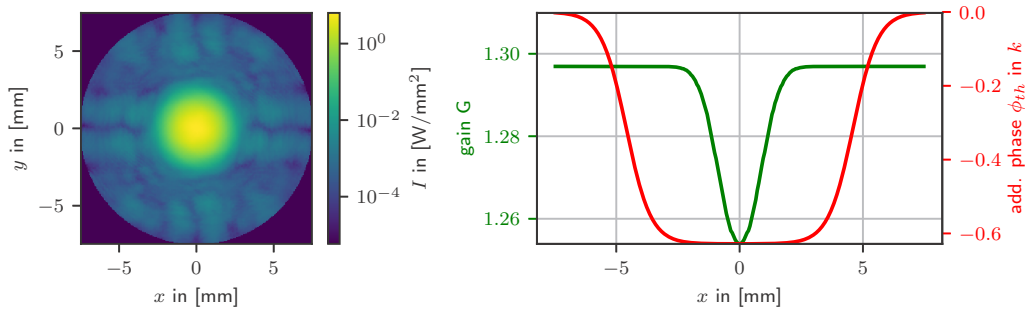


Figure 3.11.: Total intensity distribution at the disk (left) and cross-sections of the gain and the additional phase due to thermal effects (right).

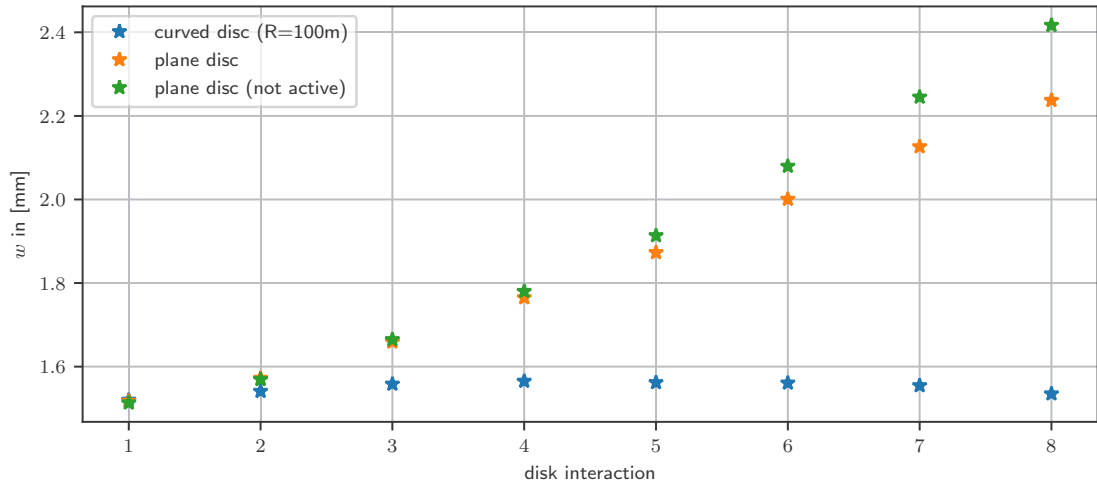


Figure 3.12.: Change of the beams waist radius w with the disk interactions for different configurations. The track between two interactions at the disk is around 1.25 m.

Based on the simulation, the impact of adjustment errors during the assembling process can be analyzed. Therefore, the nominal positions and orientation of the array mirrors are slightly disturbed by a statistical variation based on a normal distribution. For the position a standard deviation of $\sigma_{xyz} = 0.05$ mm is assumed. The standard deviation of the orientation is set to $\sigma_{\alpha} = 10''$. In Figure 3.13, the resulting light distribution at the detector is displayed. The quality of the beam is further decreased to an M^2 factor of 1.31. Due to the misalignment, the point of intersection of the beam at the disk changes with each round trip. This can be observed by investigating the total intensity at the disk in Figure 3.14. This can also lead to a higher amplification due to a more distributed stimulated emission and shifted saturation effects. For the selected example, the total power of the output beam is slightly increased compared to the ideal alignment of the mirrors.

Dependent on the application of the disk amplifier system, the simulation can be further extended to cover also short pulses and the corresponding dynamic effects within the active medium. Another possible extension to an even more holistic description would be the expansion of the empirical phase term by a detailed modeling of the thermal deformation and refractive index profile of the disc.

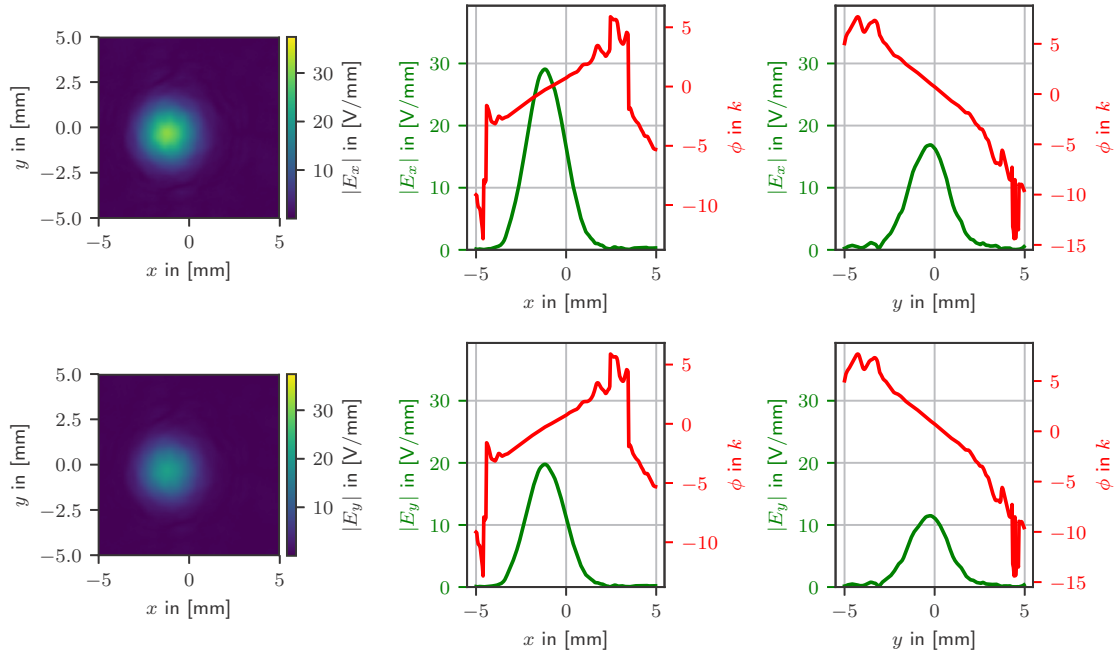


Figure 3.13.: Electrical field distribution of the amplified output beam and corresponding cross-sections. The array mirrors are statistically misaligned by standard deviations of $\sigma_{xyz} = 0.05$ mm and $\sigma_\alpha = 10''$. In the upper row, the component $|E_x|$, while in the lower row, the component $|E_y|$ is shown. The waist radius is $w = 1.5$ mm and the total power is $P = 6.18$ W. The wavelength is $\lambda = 1030$ nm.

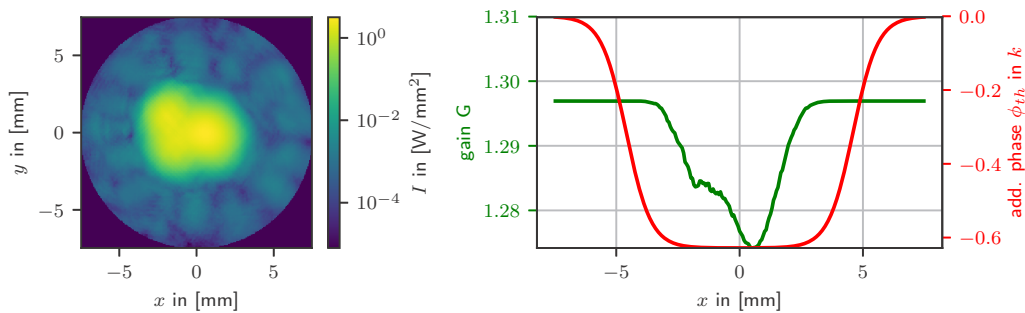


Figure 3.14.: Total intensity distribution at the disk (left) and cross-sections of the gain and the additional phase due to thermal effects (right). The array mirrors are slightly out of alignment.

4. Coherent light propagation between tilted planes

The propagation of light in a homogeneous medium between different components is a central part of a more holistic simulation of optical systems. While mostly the transport between parallel planes is considered, the evaluation of a coherent field distribution on arbitrarily rotated planes is of special interest, when dealing with an off-axis geometry. Also for the design of modern computer generated holograms (CGHs) [25], the calculation of the propagated electric field on a tilted plane plays an important role. In comparison to the extensively studied propagation between parallel planes, which is discussed in Section 2.1, fast Fourier transforms can not be applied directly due to an arising non-equidistant grid spacing. Several algorithms have been developed in the past dealing with this problem.

In Fraunhofer approximation, a solution was published by Patorski in 1983 [101], followed by several extensions based on the Fresnel condition [102–105]. The first solution incorporating the angular spectrum of plane waves was found by Tommasi et al. [106]. A major drawback of this algorithm is the necessity to deal with non-uniform and distorted sampling schemes in the Fourier domain. For the application of conventional fast Fourier transforms, a complex interpolation needs to be evaluated. During recent years, several further methods based on different interpolation strategies have been proposed [30–34]. Nevertheless, especially for large rotation angles, considerable inaccuracies coming from the interpolation can occur [35]. While this problem can be improved to a certain extent by using non-uniform fast Fourier transformations [84, 107], the optimal and application-dependent set of parameters and their efficient numerical implementation is subject of ongoing research [108]. A simple split-step propagation method is used in [109] to evaluate the field on a plane rotated around one axis. The presented algorithm is based on a similar idea, but does not use the Fresnel approximation and is valid for general rotations.

In this chapter a new approach is presented for the propagation of coherent field distributions between nonparallel planes. For the evaluation, neither explicit complex interpolations nor nonuniform Fourier transformations (NFFT), so an interpolation based on Gaussian gridding, are needed. In principle, the proposed approach is based on the idea that a general rotation can be decomposed into three individual elementary transformations according to Euler [110]. First, the field is rotated in the original plane, what can be efficiently evaluated by three shearing operations. Second, the actual wave propagation for a plane tilted around one axis is evaluated, using the angular spectrum of plane waves. Finally, another in-plane rotation of the electric field follows. In total, this leads to a quasi-fast complexity $\mathcal{O}(N^3 \log N)$ that is applicable for practical use. Besides that, the overall accuracy is independent of the rotation angle and only limited by the sampling conditions of the angular spectrum of plane waves, discussed in Section 2.1. The algorithm is formulated for vectorial fields and a flexible scaling of the output coordinates by using the chirp z-transform [48].

The chapter is organized as follows. In Section 4.1, a new algorithm for propagating electric fields on tilted planes is derived and analyzed. After the idea of decomposing the general rotation is described, the individual steps of two in-plane transformations and a quasi-fast propagation will be discussed. The first section concludes with an analysis of the mathematical complexity and run time. To demonstrate the usefulness of the developed approach, two application-related examples are studied in Section 4.2 and Section 4.3. At the end of this chapter, a comparison to the Rayleigh-Sommerfeld-integral and interpolation-based solutions is performed.

Parts of the results presented in this chapter are published in [111].

4.1. Development and analysis of a quasi-fast algorithm

In general, the orientation of the final plane of interest is connected to the original plane by a rotation. If the same origin for both planes is assumed, the final coordinate system $(x_4, y_4, z_4)^\top$ is obtained by applying the appropriate rotation on the initial coordinates $(x_1, y_1, z_1)^\top$

$$\begin{pmatrix} x_4 \\ y_4 \\ z_4 \end{pmatrix} = \mathbf{R} \begin{pmatrix} x_1 \\ y_1 \\ z_1 \end{pmatrix}, \quad (4.1)$$

where \mathbf{R} is a 3×3 matrix.

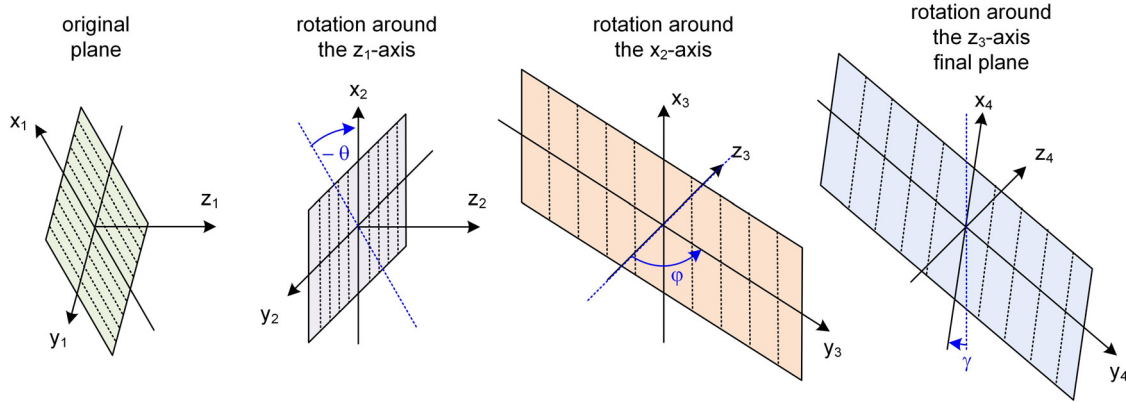


Figure 4.1.: Decomposition of the rotation from the original (green) to the final plane (blue) into three individual transformations. First, a rotation around the z_1 -axis by θ , second, around the x_2 -axis by φ and third, around the final z_3 -axis by γ .

The presented algorithm is based on a decomposition of this general rotation. According to Euler, any rotation can be described by three sequential rotations around specific axes [110]. A suitable decomposition, from the viewpoint of field propagation, is sketched in Figure 4.1. Equation 4.1 can be expressed by

$$\begin{pmatrix} x_4 \\ y_4 \\ z_4 \end{pmatrix} = \mathbf{R}_{z_3}(\gamma)\mathbf{R}_{x_2}(\varphi)\mathbf{R}_{z_1}(\theta) \begin{pmatrix} x_1 \\ y_1 \\ z_1 \end{pmatrix}, \quad (4.2)$$

with the individual rotation matrices

$$\mathbf{R}_{z_1}(\theta) = \begin{pmatrix} \cos \theta & -\sin \theta & 0 \\ \sin \theta & \cos \theta & 0 \\ 0 & 0 & 1 \end{pmatrix}, \quad (4.3a)$$

$$\mathbf{R}_{x_2}(\varphi) = \begin{pmatrix} 1 & 0 & 0 \\ 0 & \cos \varphi & -\sin \varphi \\ 0 & \sin \varphi & \cos \varphi \end{pmatrix}, \quad (4.3b)$$

$$\mathbf{R}_{z_3}(\gamma) = \begin{pmatrix} \cos \gamma & -\sin \gamma & 0 \\ \sin \gamma & \cos \gamma & 0 \\ 0 & 0 & 1 \end{pmatrix}. \quad (4.3c)$$

First, the initial field in the x_1y_1 -plane is rotated around the z_1 -axis by an angle θ , which corresponds to an in-plane rotation. The second rotation is around the x_2 -axis by φ and followed by the third and final in-plane rotation around the z_3 -axis by γ , what leads to the final coordinate system. In principle, the second step does not necessarily have to be around the x -axis but can be alternatively around the y -axis. In summary, the final field in the tilted plane of interest can be calculated by three operations, two in-plane rotations around the respective z -axes and one rotation around the intermediate x -axis, combined with the actual propagation along z . Without loss of generality, in a homogeneous, isotropic media, the following steps are formulated without the temporal component of the monochromatic, electric field $\mathcal{E}(x, y, z, t) = \mathbf{E}(x, y, z) \exp(-i\omega t)$ and for a single component only $E = E_i$. A rotation of a two-dimensional and complex field distribution in the same plane can be performed efficiently and accurate by three shearing operations [112–114]. Compared to the evaluation by a direct interpolation of the real and imaginary part of the complex field, neither sampling issues are arising nor an unwrapping process is necessary. The decomposition is visualized in Figure 4.2, where the successively applied shearing matrices are expressed as

$$\mathbf{S}_x(a) = \begin{pmatrix} 1 & a \\ 0 & 1 \end{pmatrix}, \quad (4.4a)$$

$$\mathbf{S}_y(b) = \begin{pmatrix} 1 & 0 \\ b & 1 \end{pmatrix}, \quad (4.4b)$$

$$\mathbf{S}_x(c) = \begin{pmatrix} 1 & c \\ 0 & 1 \end{pmatrix}. \quad (4.4c)$$

The shearing parameters a , b and c are dependent on the actual rotation angle θ

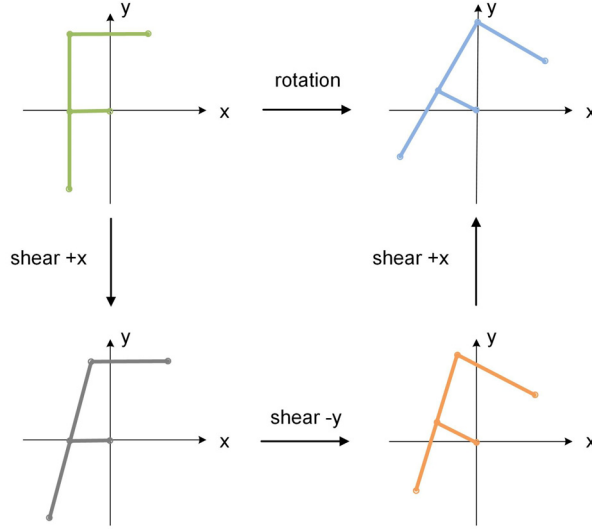


Figure 4.2.: Decomposition of an in-plane rotation into three successively applied shearing transformations.

and can be calculated by

$$\begin{aligned}
 a &= c = -\tan \frac{\theta}{2}, \\
 b &= \sin \theta.
 \end{aligned}
 \tag{4.5}$$

Each of the shearing operations is evaluated by the usage of the shift theorem of the Fourier transformation

$$\begin{aligned}
 \mathbf{S}_x(a)\{E(x, y)\} &= E(x + ay, y) \\
 &= \mathcal{F}_{\nu_x}^{-1} \{ \mathcal{F}_x \{E(x, y)\} \exp(iayk_x) \}, \\
 \mathbf{S}_y(b)\{E(x, y)\} &= E(x, y + bx) \\
 &= \mathcal{F}_{\nu_y}^{-1} \{ \mathcal{F}_y \{E(x, y)\} \exp(ibxk_y) \}.
 \end{aligned}
 \tag{4.6}$$

This evaluation is efficient and exact on a regular grid provided sufficient zero padding is applied [115]. To analyze the accuracy, an anamorphic Gaussian profile is rotated in the xy -plane step by step until it meets its initial orientation after 360° . The deviations between the twelve times rotated sample and the original

distribution are shown in Figure 4.3. The residual rms deviation is found to be $1.52 \cdot 10^{-15}$.

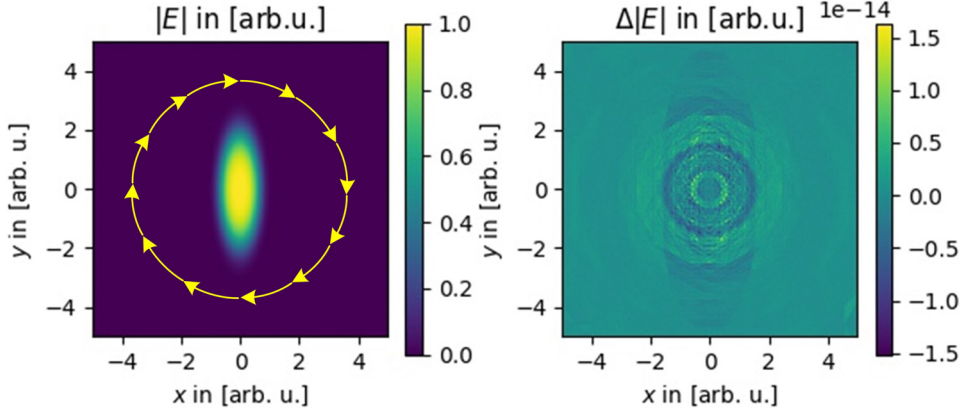


Figure 4.3.: Gaussian field distribution, which is rotated in-plane by twelve times 30° (left), and resulting deviations to the initial profile (right).

While the different components of the electric field can be rotated in the same plane by this algorithm, the obtained field vector is still expressed in the initial coordinate system. Therefore, the same rotation matrix \mathbf{R}_z needs to be applied to it. In general, this step is necessary for each of the three transformations, but can be combined to a single one by using the general rotation \mathbf{R} . Taking into account that the component E_z can be calculated based on the others E_x and E_y for a transverse field [28], the following relation holds

$$\begin{pmatrix} E_{x_4} \\ E_{y_4} \end{pmatrix} = \mathcal{F}^{-1} \left[\mathbf{T} \begin{pmatrix} \mathcal{F}[E_{x_1}] \\ \mathcal{F}[E_{y_1}] \end{pmatrix} \right], \quad (4.7)$$

$$\mathbf{T} = \begin{pmatrix} r_{11} - r_{13} \frac{k_x}{k_z} & r_{12} - r_{13} \frac{k_y}{k_z} \\ r_{21} - r_{23} \frac{k_x}{k_z} & r_{22} - r_{23} \frac{k_y}{k_z} \end{pmatrix},$$

where the transformation matrix \mathbf{T} is composed by the entries r_{ij} of the rotation matrix \mathbf{R} and the corresponding wave vector [34]. The inverse Fourier transformation is applied component-wise.

The residual transformation of the electric field is the rotation around the x_2 -axis. The layout of this step is illustrated in Figure 4.5. In general, this transformation corresponds to a y -dependent propagation of the field distribution along a specific

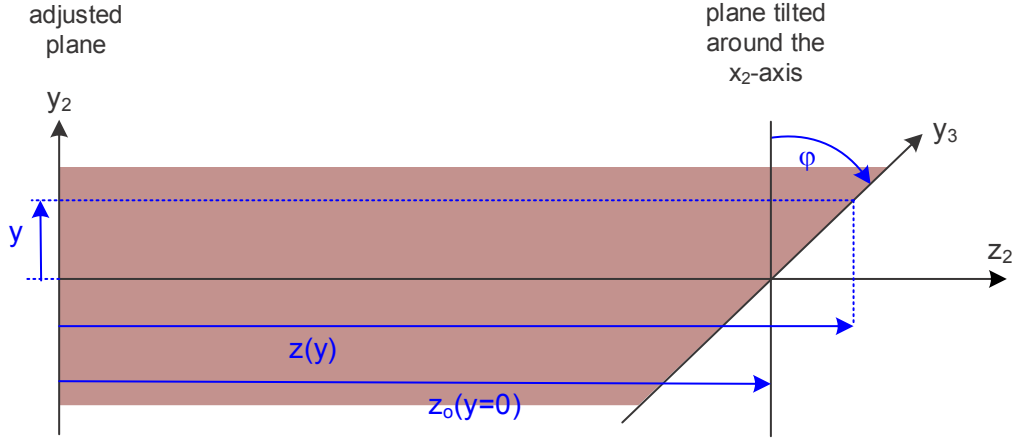


Figure 4.4.: Sketch of the rotation around the x_2 -axis by φ , which corresponds to a free-space propagation of the field distribution along the distance $z(y_2)$ into the tilted x_3y_3 -plane.

distance $z(y_2)$, which is given by the following relation

$$x_3 = x_2, \quad (4.8a)$$

$$y_2 = y_3 \cos \varphi, \quad (4.8b)$$

$$z(y_2) = y_2 \tan(\varphi) + z_0. \quad (4.8c)$$

Here, z_0 is an additional propagation distance which can be included in this step dependent on the actual application. For the evaluation of the electric field in the tilted plane, the propagation based on the angular spectrum of plane waves is modified, which is introduced and discussed in Section 2.1.1. According to Equation 2.21, the electric field at the position z is given by

$$E(x, y, z) = \iint E(k_x, k_y, 0) \exp(izk_z) \exp(i(xk_x + yk_y)) dk_x dk_y, \quad (4.9)$$

where $E(k_x, k_y, 0)$ is the spectrum of the electric field and $\exp(izk_z)$ is the propagation kernel, describing the propagation of a plane wave in a homogeneous medium

along a given distance. Inserting Equation 4.8c, the electric field at the tilted plane, but in the initial coordinate system, is given by

$$E(x_2, y_2, z_3) = \iint E(k_{x_2}, k_{y_2}, z_2) \exp(iz(y_2)k_{z_2}) \exp(i(y_2k_{y_2} + x_2k_{x_2})) dk_{x_2} dk_{y_2}. \quad (4.10)$$

After a separation of the integrals into the different dimensions and discretization, it becomes clear that this equation can be solved by a fast Fourier transformation along k_{x_2} and by a summation along k_{y_2}

$$E(x_2, y_2, z_3) = \mathcal{F}_{k_{x_2}}^{-1} \left[\sum_{k_{y_2}} E(k_{x_2}, k_{y_2}, z_2) \exp(iz(y_2)k_{z_2}) \exp(iy_2k_{y_2}) \Delta k_{y_2} \right]. \quad (4.11)$$

While details about the mathematical complexity and runtime will be discussed at the end of this section, as a next step, Equation 4.10 will be generalized for coordinates x_3 and y_3 independent of x_2 and y_2 . A flexible scaling of the coordinates is necessary for certain applications, for example in order to maintain the resolution when evaluating the light on a strongly tiled plane. As highlighted in Section 2.1, this can be realized along the x -dimension by replacing the Fourier transformation by the inverse chirp z -transform or by a scaled convolution [29]. For the y -coordinates, the connection between the two coordinates y_2 and y_3 in Equation 4.8c is substituted into the summation of Equation 4.11

$$E(x_3, y_3, z_3) = \text{chirpz}_{k_{x_2}}^{-1} \left[\sum_{k_{y_2}} E(k_{x_2}, k_{y_2}, z_2) \exp(iz(y_3 \cos \varphi)k_{z_2}) \exp(iy_3 \cos \varphi k_{y_2}) dk_{y_2} \right]. \quad (4.12)$$

An important aspect, when propagating electric fields especially on strongly tilted planes, is a correct handling of the occurring linear phase. In order to reduce the requirements on the lateral sampling, linear phases are included analytically according to the properties of the Fourier transformation. Details are given in Section 2.1.

In principle, Equation 4.11 is accurate even for large tilt angles as long as the usual

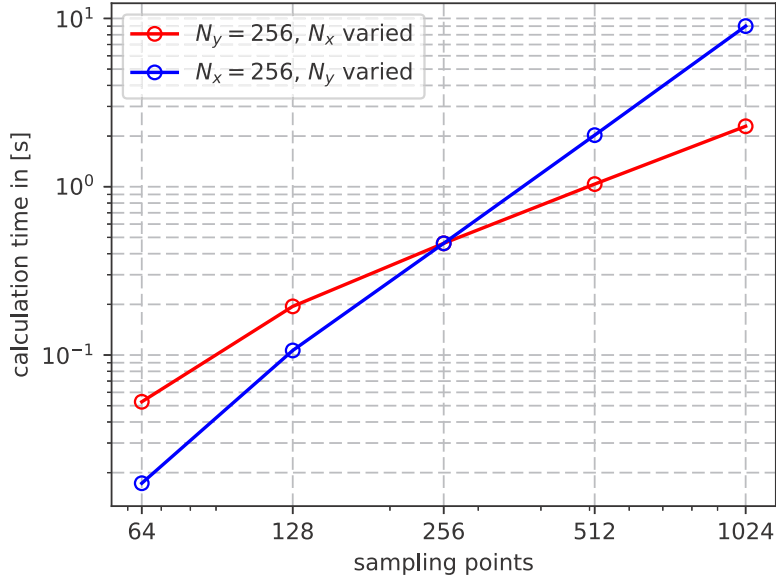


Figure 4.5.: Calculation time of the x -rotation dependent on different sampling points N_x and N_y . The sampling points along y are fixed for the red line, while for the blue line, N_x is kept constant.

requirements of the expansion into plane waves are fulfilled. From a viewpoint of runtime, the proposed algorithm is quasi-fast. This corresponds to a fast evaluation along one dimension by using the Fourier or chirp-z transformation and a comparably slower calculation of the direct summation about the second dimension. Thus, the overall complexity is $\mathcal{O}(N^3 \log N)$. The behavior of the different runtimes for the individual dimensions is shown in Figure 4.5. For an impression on the absolute performance on a typical computer (Intel i7, 2.4Ghz) and to demonstrate the usefulness for practical applications, the runtimes of the different evaluation steps are compared for several sampling configurations in Table 4.1. So far, all algorithms are implemented in Python [75] and can be optimized by an implementation into a more efficient compiled programming language.

Before several examples are studied, the proposed algorithm for evaluating the electric field on a tilted plane is summarized in terms of an implementation:

1. Decomposition of the general rotation into the angles θ , φ and γ according to Figure 4.1.

2. Zero padding of the initial field to $2N \times 2N$ and evaluation of the first in-plane transformation around θ by Equations 4.6.
3. Evaluation of the quasi-fast propagation on the tilted plane about the x axis according to Equation 4.11 and subtraction of the linear phase.
4. Final in-plane rotation of the field distribution according to (2.) around the angle γ .

Table 4.1.: Run times in seconds of the two rotation (propagation) routines and the total algorithm, together with the corresponding times of the two-dimensional FFT and the chirp- z transformation for comparison. N_x and N_y are the numbers of sampling points.

N_x N_y	= FFT	chirp- z	z -rot.	x -rot. (prop.)	total
64	0.0005	0.0017	0.0031	0.0052	0.012
128	0.0016	0.0097	0.011	0.029	0.051
256	0.010	0.045	0.076	0.461	0.615
512	0.044	0.225	0.352	4.51	5.20
1024	0.208	0.908	1.43	34.1	36.7

4.2. Example I: Gaussian Beam on a folding mirror

As a first example, a Gaussian beam is evaluated on a plane tilted around the y -axis by $\varphi = 35^\circ$. This can be for example a folding mirror. The normalized and radial symmetric Gaussian profile is defined with a waist of 0.25 mm on an equidistant grid with a sampling of 1024×1024 and lateral dimensions of 2 mm by 2 mm. The beam is assumed to be linear polarized ($|E_x| = |E_y|$). The initial phase of the beam is defined to be planar, while the wavelength is set to be $\lambda = 1 \mu\text{m}$. The lateral coordinates of the final plane are the same as for the initial distribution. According to the previous section, the overall transformation is decomposed into a rotation of the input field by 90° around the z_1 -axis, by 25° around the x_2 -axis and finally by another -90° around the z_3 -axis.

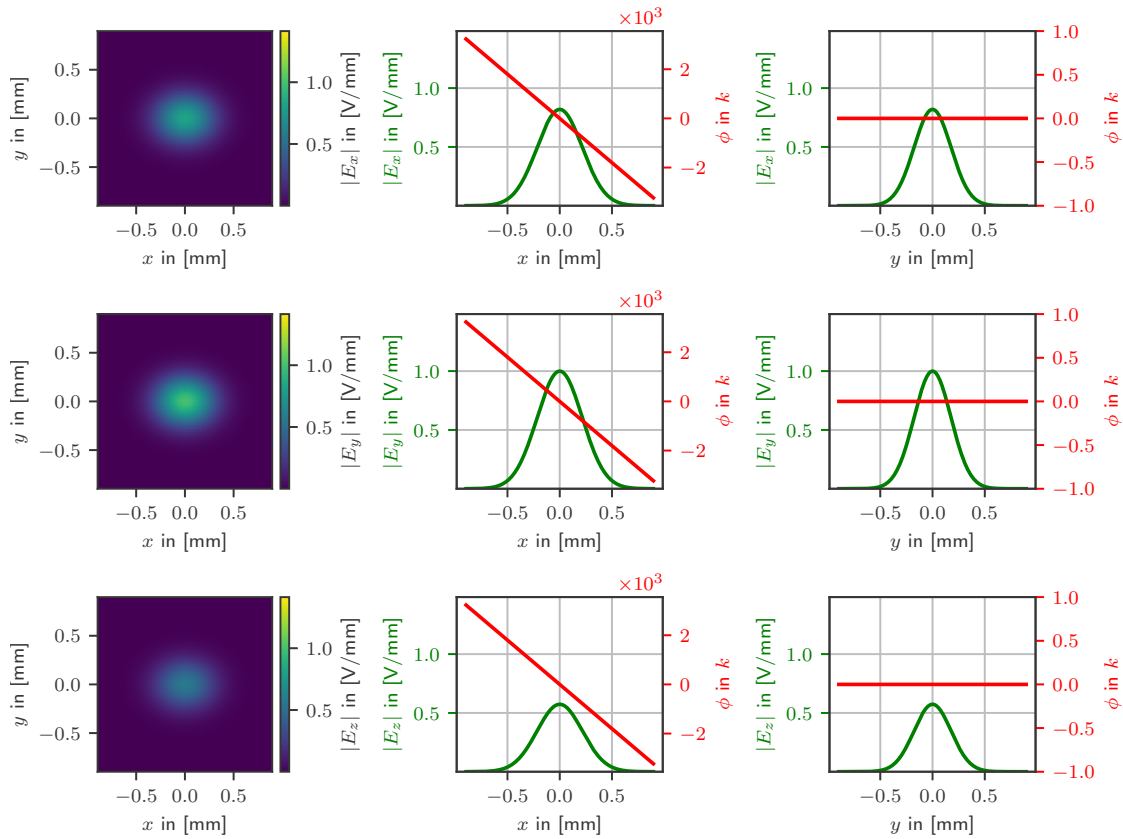


Figure 4.6.: Electric field distribution and corresponding cross-sections of a Gaussian beam on a folding mirror ($\varphi = 35^\circ$). In the upper row, the component $|E_x|$, while in the lower rows, the component $|E_y|$ and $|E_z|$ are shown. The corresponding phase is displayed in the cross-sections. The waist radius in the x direction is $w_x = 0.31$ mm and $w_y = 0.25$ mm in the y direction. The wavelength is $\lambda = 1$ μm .

The resulting electric field, amplitude and phase of the different components are shown in Figure 4.6. In the cross sections, a decrease of the amplitude $|E_x|$ by around 18% is observed, while the amplitude of the other transverse component $|E_y|$ is not affected and $|E_z|$ is increased. The reason is found in the orientation of the rotation axis. So the y -axis, and therefore $|E_y|$, stays the same, while the other components are influenced according to Equation 4.7. A consequence of the x -dependent propagation distance is the widening of the waist of the Gaussian beam by 20% along the x direction. In the same dimension, a linear dependency of the phase on the lateral coordinate x is seen, which corresponds to the tilt.

So far, the phase of the initial beam was assumed to be constant. In Figure 4.7, the two-dimensional phase is evaluated on a tilted plane ($\varphi_x = 0.3^\circ$) for different input profiles of the phase and illustrated qualitatively. In general, when light is investigated on a tilted plane, a linear contribution of the phase is observed, as it is seen in Figure 4.6 and Figure 4.7(a) for the collimated beam with its flat phase. If the input phase is set to be curved, an overlay with the linear contribution is the result and a chirp is noticed. This is demonstrated for a curved initial phase in Figure 4.7(d) and for cylindrical wavefronts in Figure 4.7(b) and (c) along different sections.

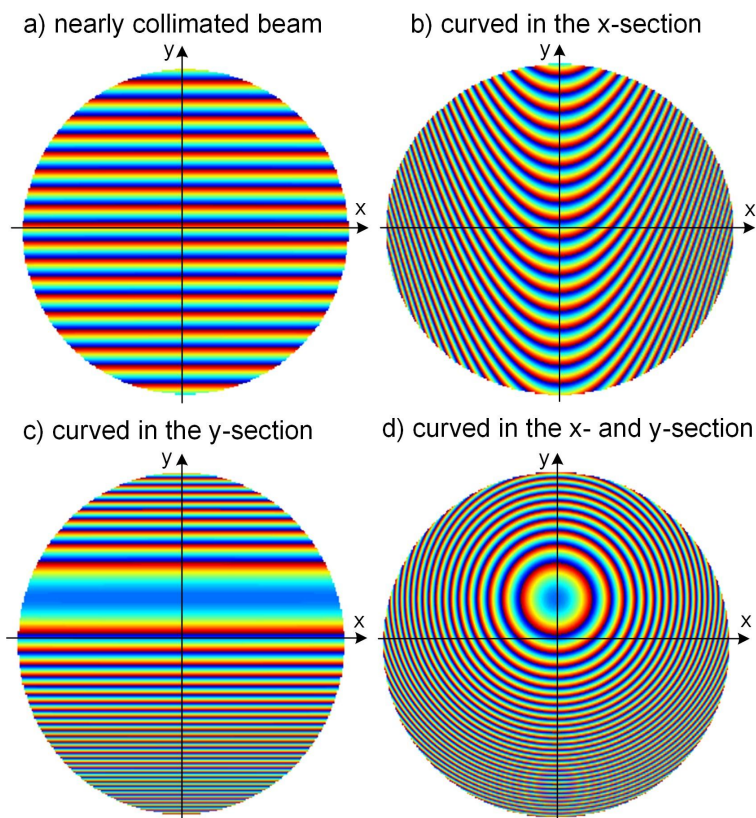


Figure 4.7.: Phase distribution (wrapped) on a slightly tilted plane ($\varphi = 0.3^\circ$) for different input beams.

4.3. Example II: Intensity distribution on a high-order Littrow grating

One advantage of the proposed algorithm is the good performance for large rotation angles. Therefore, as another example, the intensity profile on a plane under grating incidence ($\varphi = 88^\circ$) is studied. This scenario is of special interest for the simulation of high-order Littrow gratings [109]. As input beam, a nearly top-hat profile with a width of 3 mm by 3 mm is defined. The wavelength is set to be $\lambda = 1 \mu\text{m}$. The results are shown in Figure 4.8.

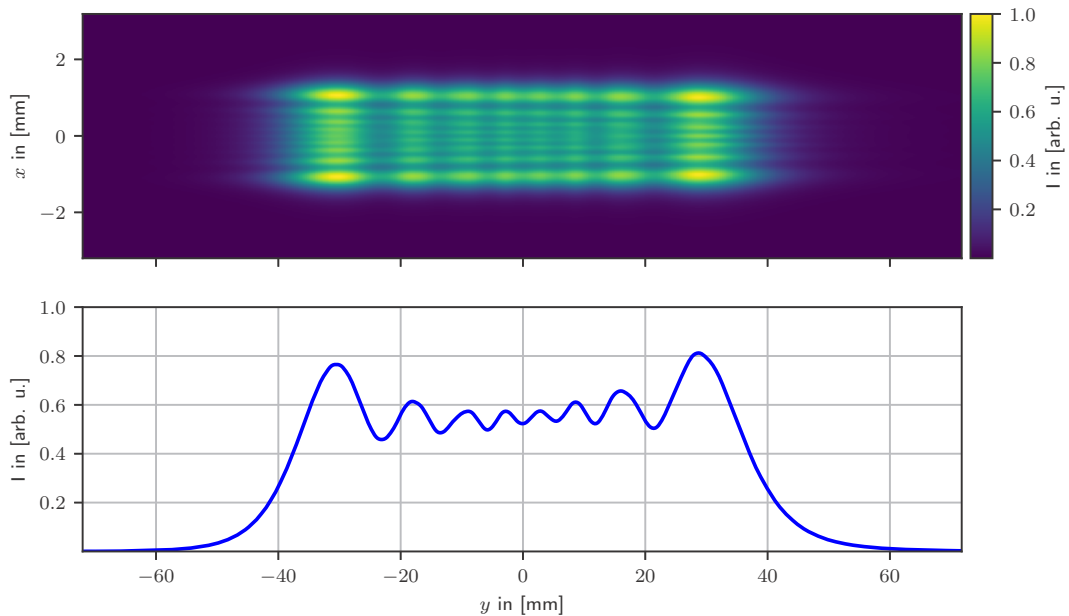


Figure 4.8.: Intensity distribution and corresponding cross-section of a nearly top-hat beam on a strongly tilted plane ($\varphi = 88^\circ$). The intensity is normalized to its maximum and the wavelength is $\lambda = 1 \mu\text{m}$. The x - and y -axis scales different.

To display the full field, the scaling of the y coordinates is enlarged due to the strong tilt and the corresponding projection. In the cross section along the unaffected x -axis, the classical Fresnel diffraction pattern is observed. In contrast, we get a deviation from this pattern dependent on the y coordinate that comes from an increasing propagation distance. As a result of the different sign of the propagation

distance relative to the center of the final plane, the pattern is different for positive and negative y coordinates. The right part of the plane ($y > 0$), which is closer to the origin of the input beam, has a narrower width and a higher intensity compared to the left part ($y < 0$).

4.4. Comparison to interpolation based methods

The scope of this section is to compare the proposed method to other algorithms based on interpolation. Before two exemplary field distributions for different tilt angles are evaluated and compared, the validity of the proposed method even for large tilt angles is demonstrated by a verification with the Rayleigh-Sommerfeld integral. Furthermore, general differences between the studied approaches are discussed and highlighted.

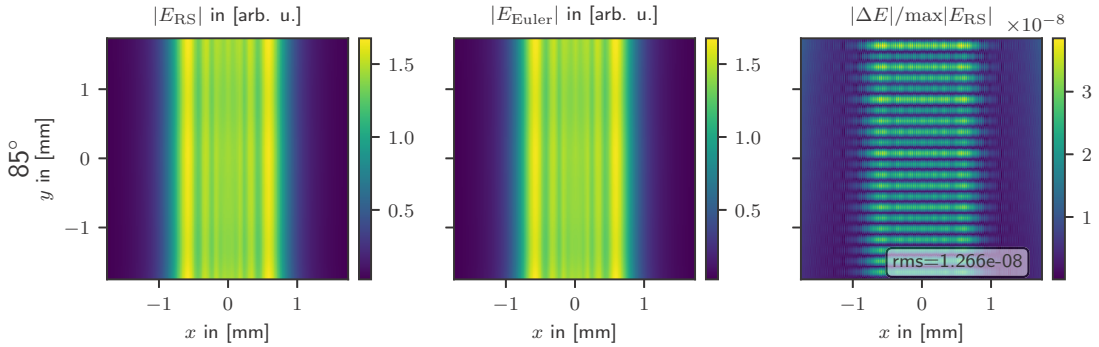


Figure 4.9.: Electric field distributions of a top-hat beam on a tilted plane ($\varphi = 85^\circ$). The result calculated by the Rayleigh-Sommerfeld integral $|E_{RS}|$ (left) is compared to the result evaluated by the proposed method $|E_{Euler}|$ (center). The relative deviations $|\Delta E|/\max|E_{RS}|$ and the corresponding rms error are displayed in the right figure. The wavelength is $\lambda = 1 \mu\text{m}$ and the sampling is 251 by 251 points.

In Figure 4.9, the electric field distribution of a top-hat beam on a tilted plane ($\varphi = 85^\circ$) is compared for an evaluation by the proposed method $|E_{Euler}|$ and by the Rayleigh-Sommerfeld diffraction integral $|E_{RS}|$ [27]. The wavelength is $\lambda = 1 \mu\text{m}$ and the distance between the initial and the final plane is 100 mm to fulfill the requirements of the Rayleigh-Sommerfeld integral [116]. The low relative deviations $|\Delta E|/\max|E_{RS}|$ with an rms error of 1.266×10^{-8} shows the validity of the quasi-fast

method based on the Euler decomposition. Residual are mainly numerical errors coming from the discretized evaluation of the chirp z-transform.

In [33, 35], the propagation theory for evaluating the electric field on tilted planes by using interpolation is discussed. In order to allow for an efficient calculation by using the fast Fourier transformation, a complex interpolation of the spectrum of the initial distribution onto a non-equidistantly spaced grid is necessary. Instead of the accurate but time consuming interpolation by sinc-functions, typically an approximation by cubic-functions is used [34]. As a consequence, inaccuracies are expected, especially for large tilt angles. The proposed algorithm based on the decomposition of the rotations is due to the quasi-fast complexity in principle not as efficient, but independent on the rotation angle. Another advantage is that the numerical implementation is rather simple and there is no need for defining any application specific parameters, which are dependent on the initial field. Further, the sufficient selection of the interpolation method and corresponding parameters can be a critical point, especially when using non-equidistant Fourier transformations, so an interpolation by Gaussian gridding [108].

In Figure 4.10, a Gaussian beam with a waist radius of $w_0 = 0.3$ mm and a wavelength of $\lambda = 1$ μ m is propagated onto planes with increasing tilt angle $\varphi = [0^\circ, 27^\circ, 53^\circ, 80^\circ]$. The distance between the initial and the tilted plane is 100 mm. For the evaluation of the propagation, two different methods are used. In the left column, the electric field distribution calculated by the proposed method $|E_{\text{Euler}}|$ is shown. To the right, the field is evaluated based on a complex, cubic interpolation of the spectrum $|E_{\text{cubic}}|$. While the amplitude and phase distribution of a Gaussian beam are rather smooth, the complex interpolation becomes more critical for other field distributions. Therefore, the same comparison is made for a square-shaped top-hat beam with a width of 1.7 mm. Again, the distance between the initial and the tilted plane is 100 mm and the wavelength is $\lambda = 1$ μ m. The results are shown in Figure 4.11. The relative deviations $|\Delta E|/\max|E_{\text{Euler}}|$ are increasing stronger for large tilt angles compared to the Gaussian distribution. For a tilt angle of $\varphi = 53^\circ$, the error is already up to 0.23% of the maximum signal $\max|E_{\text{Euler}}|$. For a tilt angle of $\varphi = 80^\circ$, the error is further increased up to 38% and demonstrates the inaccuracy of the interpolation based algorithm for large tilt angles. In summary, the algorithms based on interpolation are preferred for limited angles due to a better efficiency. For an application where a high accuracy is needed or especially for large angles, the

proposed method is advantageous.

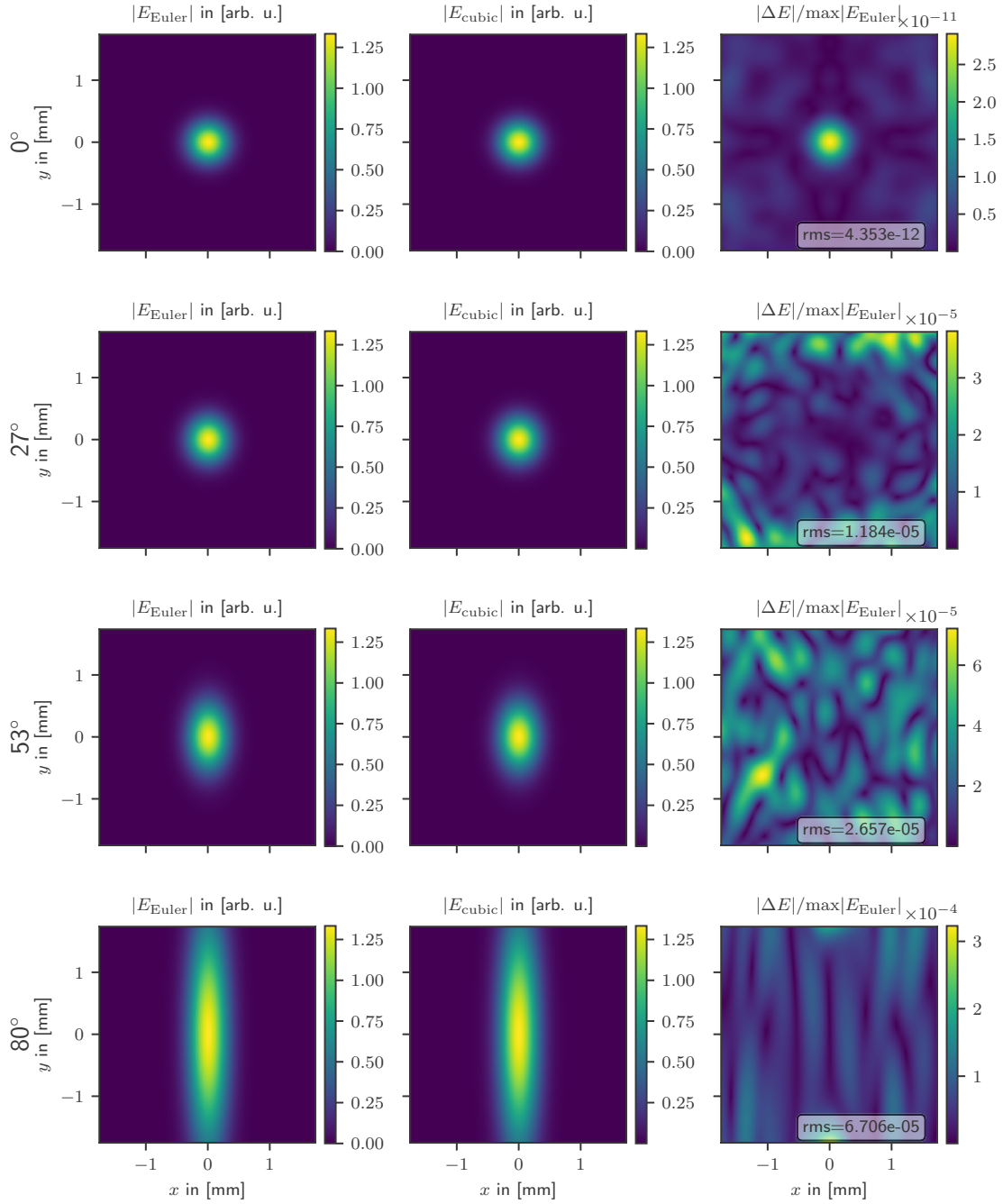


Figure 4.10.: Electric field distributions of a Gaussian beam on a tilted plane for different angles ($\varphi = [0^\circ, 27^\circ, 53^\circ, 80^\circ]$). The results calculated by the proposed method $|E_{\text{Euler}}|$ (left column) are compared to the results evaluated based on cubic interpolation $|E_{\text{cubic}}|$ (central column). The relative deviations $|\Delta E|/\max|E_{\text{Euler}}|$ and the corresponding rms error are displayed in the right column. The wavelength is $\lambda = 1 \mu\text{m}$.

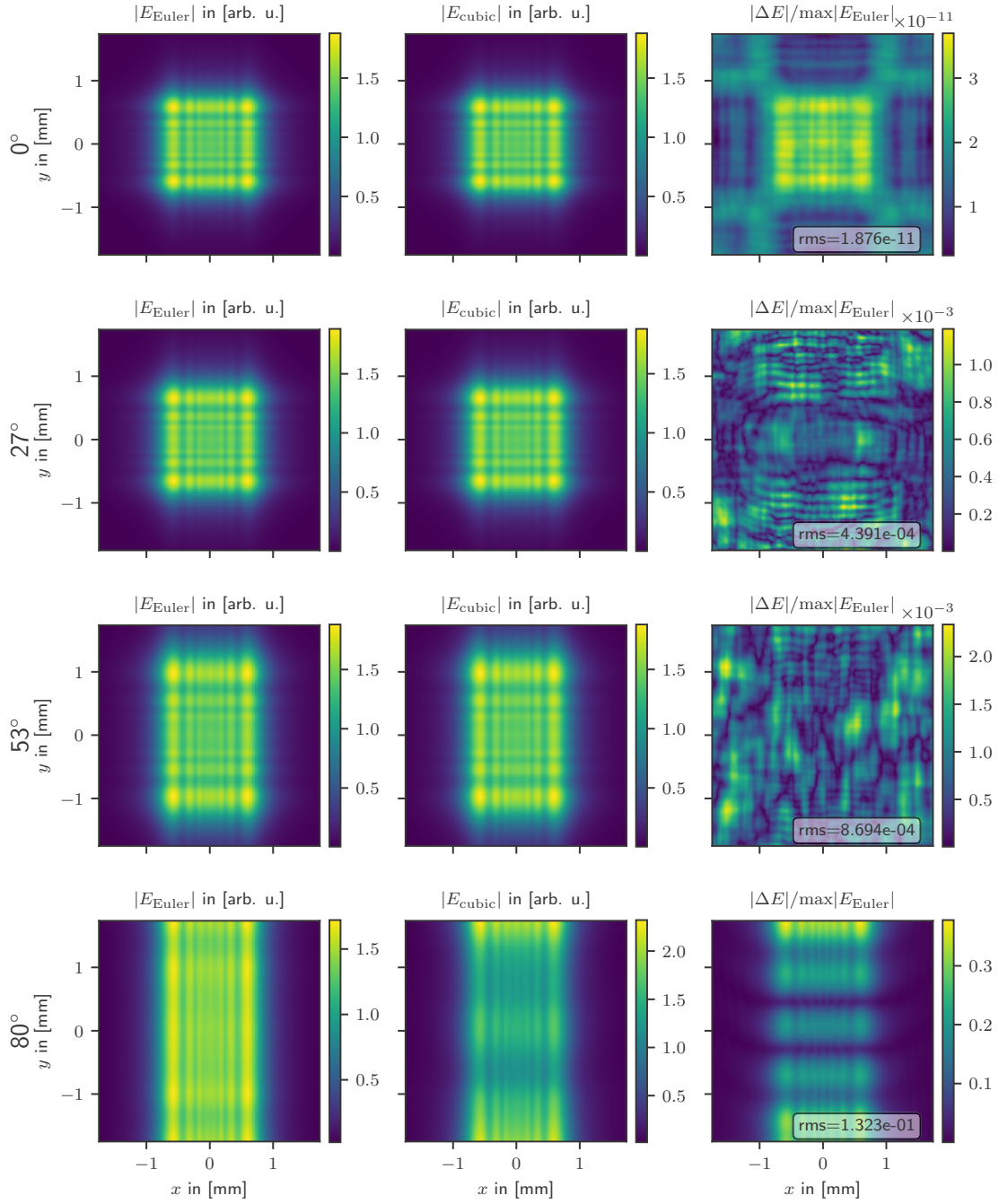


Figure 4.11.: Electric field distributions of a top-hat beam on a tilted plane for different angles ($\varphi = [0^\circ, 27^\circ, 53^\circ, 80^\circ]$). The results calculated by the proposed method $|E_{\text{Euler}}|$ (left column) are compared to the results evaluated based on cubic interpolation $|E_{\text{cubic}}|$ (central column). The relative deviations $|\Delta E|/\max|E_{\text{Euler}}|$ and the corresponding rms error are displayed in the right column. The wavelength is $\lambda = 1 \mu\text{m}$.

5. Simulation and analysis of imaging systems including real freeform components

While the design and modeling of many optical components, as plane or spherical mirrors and lenses, by simple, ideal surface descriptions lead to a satisfactory result, in recent years, modern systems often include optical components differing from this structure. For example, additive manufactured lightweight mirrors [117], printed diffractive Elements [118] and objective lenses [6], or freeform components, produced by diamond-turning [9,119] are becoming increasingly available. However, the realization is associated with manufacturing errors, such as surface imperfections or deformations. This often remains to be a limiting factor for the performance of the final application. The consideration of this impacts will lead to a more holistic simulation and enables the performance prediction of the system as a whole.

With increasing availability of the manufacturing technologies, especially surfaces without remaining symmetry are becoming an exiting opportunity in optical design. Apart from illumination and beam profiling systems, freeform surfaces can be found more and more also in imaging applications [120–122]. The additional degrees of freedom enable more compact, high-performance systems with off-axis geometries [123,124]. The manufacturing typically involves single point diamond-turning in combination with additional polishing methods [9,125,126]. Apart from micro roughness, more localized figure errors and characteristic, regular ripples within the mid-spatial frequency range (MSF) arise due to the limited accuracy of the turning process [13,127]. In Figure 5.1, the qualitative power spectral density (PSD) of a typical, manufactured surface profile is shown. While the resolution is usually affected by the low spatial frequency errors, the contrast is reduced due to deviations, such as roughness, with a high spatial frequency [65]. The impact of the range in between,

for example the regular MSF ripples, is more system dependent. Especially when dealing with shorter wavelengths, the deviations of the produced to the ideal surface profile are still a limiting problem. Currently, there exist a few comprehensive approaches for the analysis of different fabrication processes [36, 37], the theoretical description of surface deformations on the point spread function (PSF) [38] and the modulation transfer function (MTF) [39–42]. In order to close the gap between the optical design, the manufacturing process and the adjustment procedure, there remains a need for a more holistic description of even complex systems with multiple freeform components.

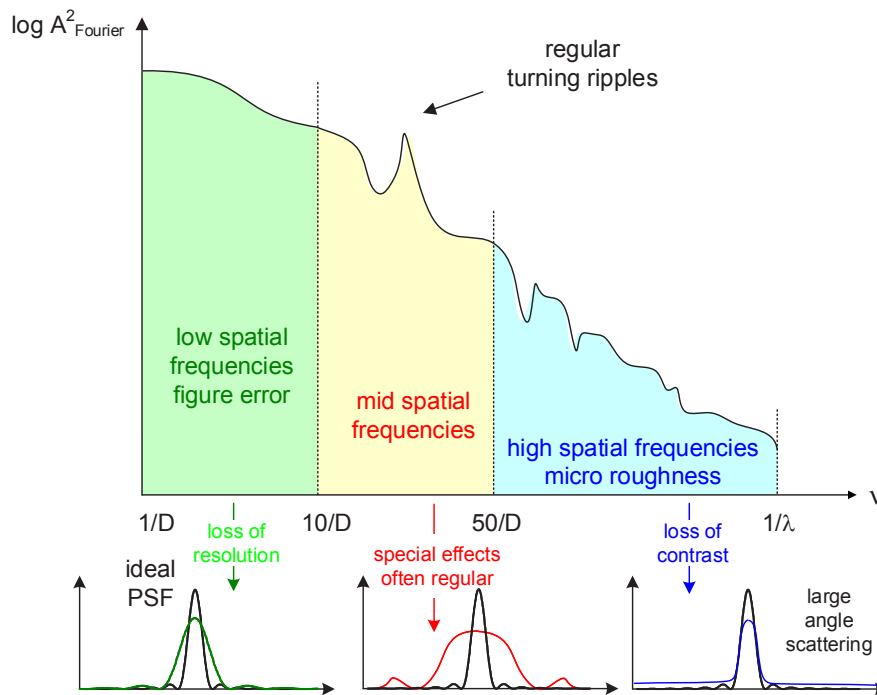


Figure 5.1.: Qualitative power spectral density (PSD) of a typical, manufactured surface profile. For a one-dimensional representation, the PSD is averaged along the azimuthal dimension. The spatial frequency ranges are only rough estimates and are defined relative to the surface diameter D and the wavelength λ . The impacts on the point spread function (PSF) are sketched below. [65]

The presented approach is based on an analytic description of the real, manufactured surface profiles. Lateral shifted radial basis functions (RBFs) are used to include more localized figure errors. In addition, the critical MSF ripples are covered by a new approach based on the PSD of the surface imperfections. By a limited number of coefficients and parameters, not only an efficient simulation by ray-tracing but

also a comprehensive tolerancing analysis is realized. Parts of the approach for the description, especially the selection of a suitable set of parameters for the RBFs, were developed within the authors masters thesis [73], but are introduced briefly in the first section for a better understanding. Within this work the approach is enhanced to a more holistic simulation of even complex systems and the verification is made based on a demonstrator for imaging applications.

The chapter is structured as follows. In Section 5.1, the new approach for the description of real freeform components, manufactured by diamond-turning, is presented and discussed. The concept for a more holistic simulation of real optical systems including the surface imperfections is realized afterwards in Section 5.2. Therefore, an afocal, anamorphic imaging telescope in the visible wavelength range is introduced and used as a demonstrator system. Its manufactured optical surfaces, four freeform-shaped mirrors, are described by the introduced approach and included into the simulation. The residual deviations and general limits of the description are discussed. In Section 5.3, the simulation result is analyzed and compared to the measured wavefront for different field angles. The solution is verified by also taking the uncertainties of the adjustment into account. The chapter concludes with two tolerancing scenarios. In the first example, the analytic descriptions are used for analyzing the impact of the figure error. The regular ripples structures are varied in amplitude and frequency in the second case study.

Parts of the results, presented in this chapter, are published in [128] and [129].

5.1. Surface description of diamond-turned freeform components

After the manufacturing of the freeform surface, reflective or refractive, with respect to the optical design, the sag of the component is measured. This can be for example realized by interferometry [81,130,131]. In order to address the quality of the surface, the deviations $z_{\text{dev}}(x, y)$ between the ideal $z_{\text{ideal}}(x, y)$ and the real profile $z_{\text{real}}(x, y)$ are evaluated

$$z_{\text{dev}}(x, y) = z_{\text{real}}(x, y) - z_{\text{ideal}}(x, y). \quad (5.1)$$

In Figure 5.2, the deviations of a typical freeform surface, manufactured by diamond-turning, are shown. Apart from figure error with a peak-to-valley value of $0.4\ \mu\text{m}$, characteristic, regular ripples are observed. The specific structure results from a combination of environmental influences, such as changes in temperature and pressure, and vibrations between the manufacturing machine and the optical surface. Typically, the center of the periodic structure coincides with the pivot of the turning process. The spiral tool path, with a pitch in the range of 6 to $75\ \mu\text{m}$, is usually not resolved in the measurement [119, 132]. In the corresponding one-dimensional PSD of the surface imperfections, see Figure 5.5, regular ripples can be identified by several peaks for specific spatial frequencies ν .

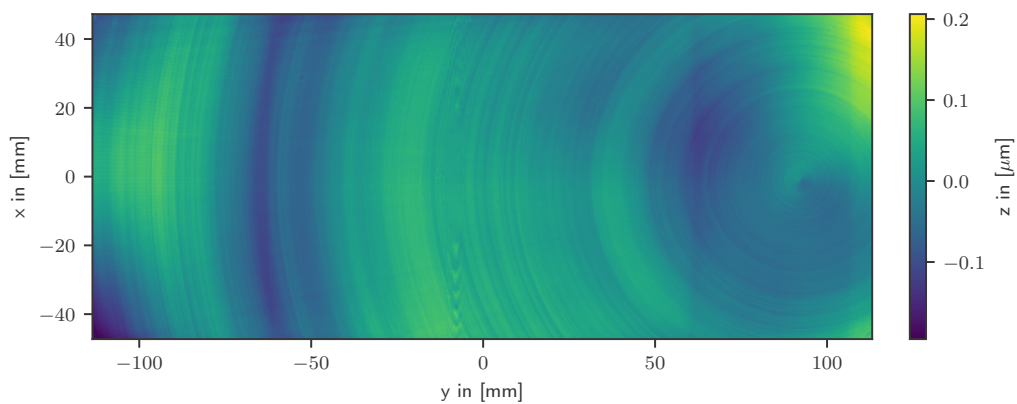


Figure 5.2.: Manufacturing deviations of a typical freeform surface, produced by diamond-turning. The rms error is 72 nm.

The approach to include these imperfections into the design and simulation of the optical system is based on an analytic description of the real surface profile, which allows for a simulation by ray-tracing and a tolerancing analysis with respect to the measured profiles. The goal is to find such a continuous function $f(x, y)$ that approximates the measured data. For M measurements $z_i(x_i, y_i)$ this ideally implies

$$f(x_i, y_i) \approx z_i, \quad i = 1, \dots, M. \quad (5.2)$$

The description of the ideal surface is given by the optical design. Typically, a set of global polynomials is used here, which are introduced and discussed in Section 2.3. Due to their lack in localized finite support, an appropriate approximation of the manufacturing deviations is not possible with a reasonable number of coef-

ficients [65]. Therefore, an alternative set of functions is necessary to include the imperfections. In this new approach, lateral shifted RBFs, for example Gaussian functions $\phi_{\text{RBF}}(x, y)$ with a certain shape factor ϵ_n , distributed on a grid (x_n, y_n) , are used to describe the more localized figure errors,

$$z_{\text{fig}}(x, y) = \sum_n c_n \cdot \phi_{\text{RBF}}(x - x_n, y - y_n, \epsilon_n). \quad (5.3)$$

Details on the selection of an optimal set of parameters (x_n, y_n, ϵ_n) and coefficients c_n are given in Section 2.3. In addition, the regular ripples are approximated by a linear combination of radial symmetric rings with a certain amplitude a_n , b_n and spatial frequency k_n . The functions are defined in polar coordinates by

$$z_{\text{MSF}}(r, \varphi) = \sum_n (a_n \sin(k_n r) + b_n \cos(k_n r)) \cdot \cos(m_n(\varphi + \varphi_0)) \cdot \gamma_n(r), \quad (5.4)$$

$$r = \sqrt{(x - x_c)^2 + (y - y_c)^2}, \quad (5.5)$$

where (x_c, y_c) corresponds to the pivot of the manufacturing process. To not only describe radial symmetric structures, the equation includes an azimuthal dependent term with order m_n and offset φ_0 . To overcome the singularity at $r = 0$, an additional function $\gamma(r)$ is necessary, which can be the complement of a Gaussian function. While the coefficients a_n and b_n are determined by using least squares, the spatial frequencies of the rings are determined, by evaluating the PSD in the one-dimensional or in an extended, azimuthal dependent two-dimensional approach [133]. The entire approach is illustrated in Figure 5.3. In summary, the description of the real surface is composed by global polynomials for the ideal profile, RBFs for the figure error and additional MSF-functions to describe the residual, regular ripples.

The results for the example surface profile are given in Figure 5.4. Not only the figure error but also the periodic ripples are described by the presented approach. Residual and not covered are mostly unstructured deviations with an rms error of 3 nm. In principal, they may still be included as an additional optical path length [41, 134] or by statistical methods used in Chapter 6. In the corresponding PSD, see Figure 5.5, the low spatial frequencies are covered by the RBFs, while the

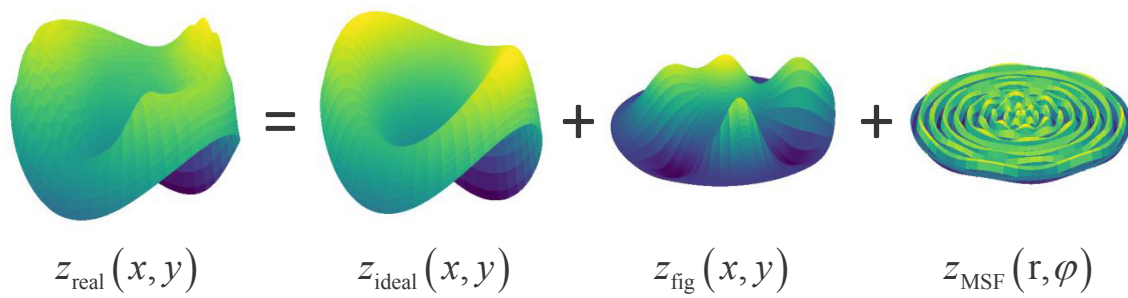


Figure 5.3.: Sketch of the approach. The real surface z_{real} is composed by global polynomials for the ideal profile z_{ideal} , RBFs for the figure error z_{fig} and additional MSF-functions to describe the regular ripples z_{MSF} .

range is further extended by the additional set of functions for the critical MSF errors. Specific deviations for the particular surface, such as the horizontal lines, are discussed within the next section after the demonstrator system is introduced.

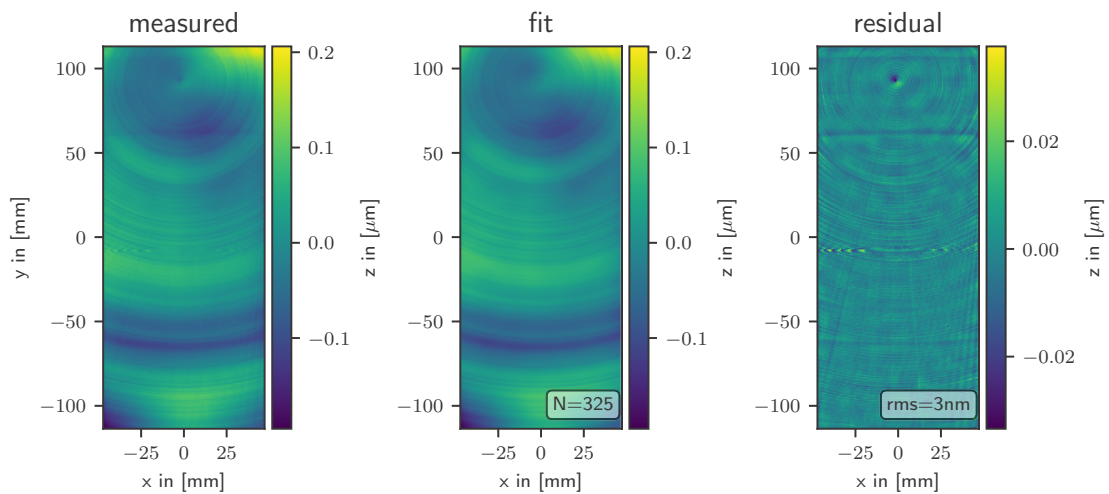


Figure 5.4.: Approximation of the manufacturing deformations for the exemplary freeform surface by 250 RBFs and 75 additional MSF-functions. The residual deviations are shown in the right figure. The scaling of the x - and y -axis is not equal.

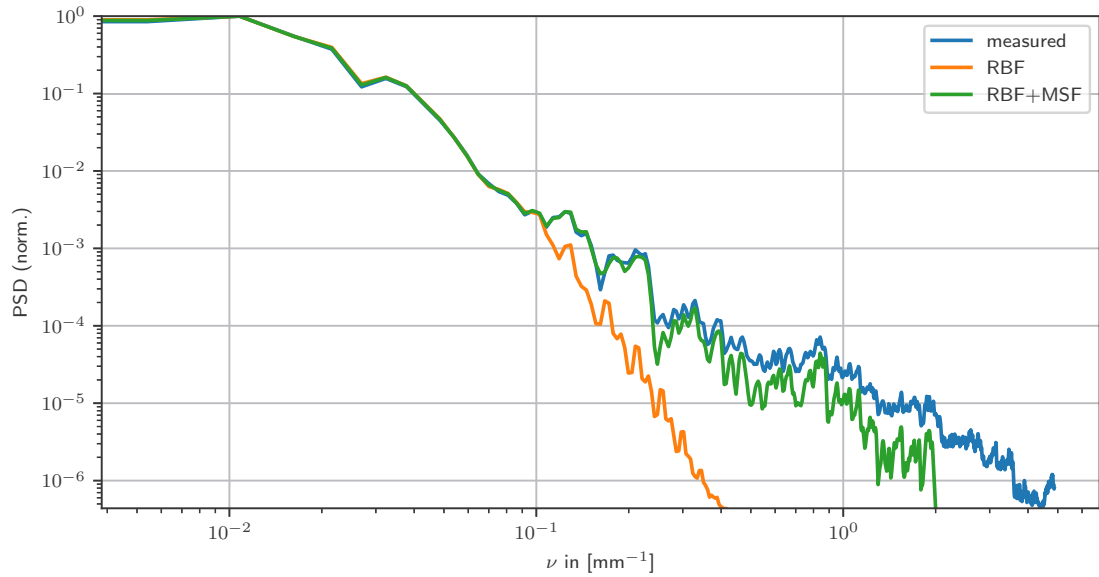


Figure 5.5.: Normalized power spectral density (PSD) for the measured surface deformations (blue) of the example freeform surface, the corresponding fit based on 250 RBFs (orange) and with additional 75 MSF-functions (green).

5.2. Holistic simulation of an afocal, anamorphic imaging telescope in the visible wavelength range

In this section, a solution for a more holistic simulation of real optical imaging systems is presented by including the influence of the manufactured components. For this purpose, a demonstrator system will be introduced before integrating the surface deviations based on the approach described in the previous section.

The chosen example system, an afocal, anamorphic imaging telescope [43], was developed, manufactured and assembled by the Fraunhofer IOF, Jena. The goal of this setup is to image a rectangular shaped entrance pupil (200 mm × 50 mm) on a square exit pupil (60 mm × 60 mm). Typically, these instruments are used in space application as front optics for subsequent spectrometers [135]. The field of view of the obscuration-free telescope is $\pm 3.22^\circ$ along the x-axis and $\pm 0.47^\circ$ along the y-axis. The optical design for the visible wavelength range is based on four reflective surfaces and illustrated in Figure 5.6. The surface of each of the four mirrors is

described by an off-axis, anamorphic asphere [136]. Nevertheless, the individual components are considered to be freeforms due to fact that the aspheres are used off-axis and that in each case two mirrors are manufactured on the same substrate which leads to an overall free-shaped surface [119]. The advantage of producing two mirrors on a common body, what can be seen in the mechanical layout in Figure 5.6, is a reduction of the degrees of freedom for the alignment and therefore an easier assembling process. Both aluminum substrates are manufactured by ultra-precise diamond-turning.

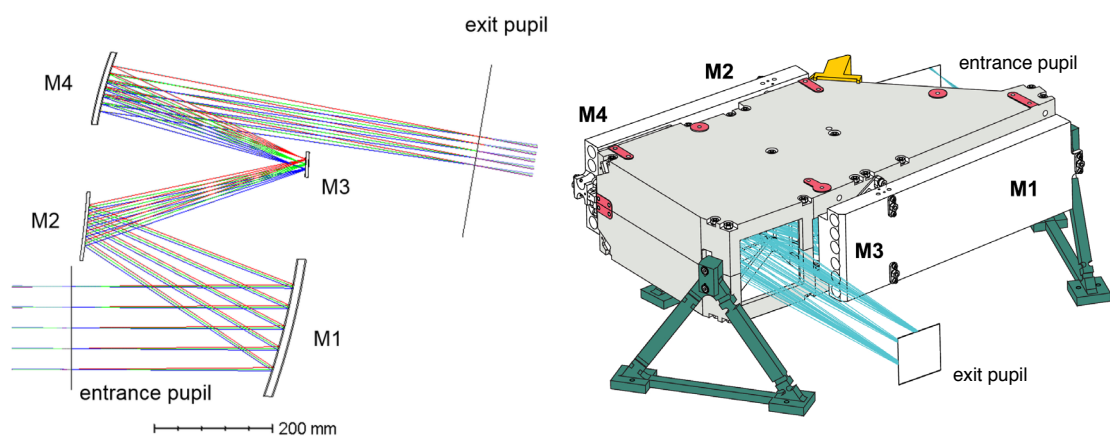


Figure 5.6.: Optical (left) and mechanical layout (right) of the afocal, anamorphic imaging telescope. The system is based on four freeform mirrors M1 to M4. [43]

To simulate the impact of the surface deformations, the real surface profiles need to be reimplemented into the optical design. Therefore, the measured surface profiles are analyzed and described according to the approach introduced in Section 5.1. The interferometrically measured deviations between the real and the ideal surface, the corresponding analytic fit and residual deviations are shown in Figure 5.7. To achieve an overall rms-error within the range of a few nanometers, only around 200 to 300 functions (RBF and MSF) are necessary, which allows for a fast simulation by ray tracing later. It should be noted that the overall performance of the approach is strongly dependent on the quality of the corresponding measurement. In discussion with the engineers responsible for the manufacturing, for example, the horizontal lines on the first mirror or the central bump on the last surface are identified to

be artifacts of the measurements. This will be verified later when comparing the simulation results with the experimental data.

As a final step to allow for a more holistic simulation of the overall system, the analytic surface profiles of the real components are implemented back into the optical design. Based on geometrical optics, the impact of the real components is simulated by ray-tracing. Due to the analytic description with a limited number of coefficients, the intersection points and new directions on the surface can be efficiently determined. If much smaller surface structures are included, diffraction effects need to be considered [134]. One possibility for the implementation is to use a user-defined surface together with a dynamic link library (DLL) in Zemax OpticStudio [22]. Within this work, the new software distribution based on Python is used, presented in Chapter 3. While the overall performance of the ray-tracing is not as efficient, the advantages are, a more flexible definition of the individual coordinate systems and a direct implementation of the real surface descriptions. In summary, this allows for a comprehensive tolerancing analysis, what will be shown later. However, Zemax OpticStudio is used for a verification of the ray-tracing engine, which is shown to be identical within the numerical accuracy [90]. In comparison to the ideal system, the number of traced rays per second is decreased by only 39 %, evaluated on a typical computer (Intel i7, 4x2.5 GHz, 16 Gb memory).

5.3. Results and verification

Based on the approach, presented in the previous section, the performance of the example system can be analyzed by common tools, i.e., the MTF or the geometric spot diagram. In this work, the discussion is mainly focused on an evaluation of the wavefront in the exit pupil, what is common as a performance criterion for high-performance systems. To avoid redundancy, the results are displayed and discussed for different fields of view along the y -axis. However, the evaluation along the x -axis follows the same scheme.

As a first step, the anamorphic telescope is simulated under ideal conditions by taking only the designed surface profiles and a perfect adjustment of the individual components into account. A wavelength of 632.8 nm is selected to allow later in this section for a comparison with measured data, obtained by a helium-neon laser. In

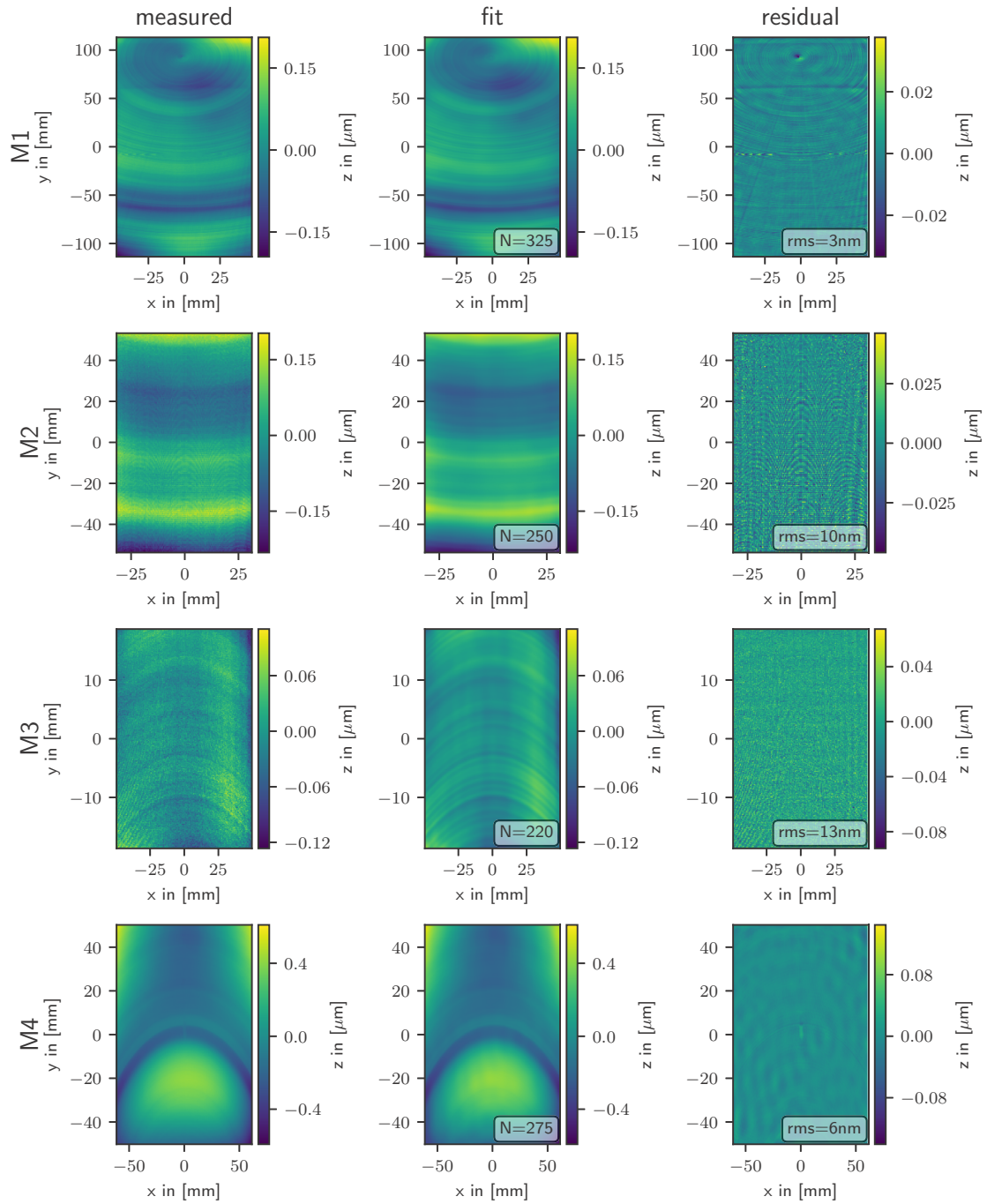


Figure 5.7.: Measured surface deformations for the mirrors M1 to M4 (left column). The corresponding fit and the residual deviations to the measurements are presented in the central and right column, respectively. The rms-error and the total number of functions N are included in the corresponding figures (M1: 250 RBFs + 75 MSFs, M2: 200 RBFs + 50 MSFs, M3: 170 RBFs + 50 MSFs and M4: 200 RBFs + 75 MSFs). The scaling of the x - and y -axis is not equal.

Figure 5.8, the optical path difference (OPD) in the exit pupil is displayed for three different fields along the y -axis. The intersection angle of the central field is 0° at the entrance pupil. For the two outer fields, the angles are $\pm 0.235^\circ$. By comparing the individual OPDs, the ideal system is corrected quite homogeneous for the different fields of view. The rms errors of the wavefront are between 43 nm and 44 nm. The peak-to-valley errors of the two outer fields differ slightly from the value of 385 nm for the central field. For an incident angle of 0.235° and -0.235° , they are 257 nm and 496 nm, respectively. Remaining is mostly astigmatism. For the specific wavelength, the rms errors are below 0.1λ . Therefore, the studied telescope can be considered to be diffraction-limited under ideal conditions [56].

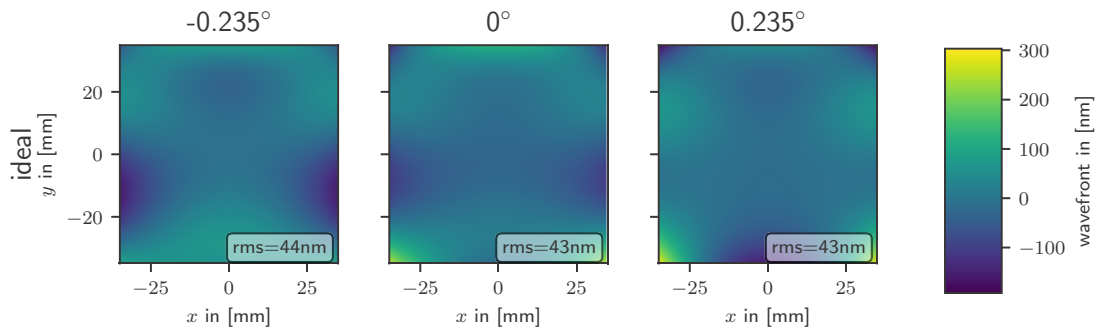


Figure 5.8.: Simulated wavefront of the setup under ideal conditions for incident angles of -0.235° , 0° and 0.235° . The rms errors are included in the corresponding figures. The wavelength is $\lambda = 632.8$ nm.

So far, only ideal components have been considered. In a next step, the manufacturing deformations are included according to the previous Section 5.2. The resulting, simulated real wavefronts are shown in the upper row of Figure 5.9 for the different fields of view. By investigating the OPD for the central field, the presented approach is capable of describing not only the influence of the figure error but also the impact of the periodic MSF-ripples coming from the manufacturing by diamond turning. One characteristic feature in the OPD is the horizontal 'blue bow' in the center. By comparing the surface deformations of the different mirrors in Figure 5.7, nearly the same 'blue bow' is found on the last mirror M4. The manufacturing errors of this mirror are almost directly mapped onto the wavefront because it is closest to the exit pupil. For an increased field angle, the structures coming from the field correlated surfaces are shifted along the corresponding axis. In comparison to the results under ideal conditions in Figure 5.8, a strong performance degradation is observed for all fields. The rms errors of the individual field angles, 0.235° , 0° and -0.235° ,

are increased to 233 nm, 308 nm and 342 nm, respectively. In total, this corresponds to performance decay up to a factor of around seven.

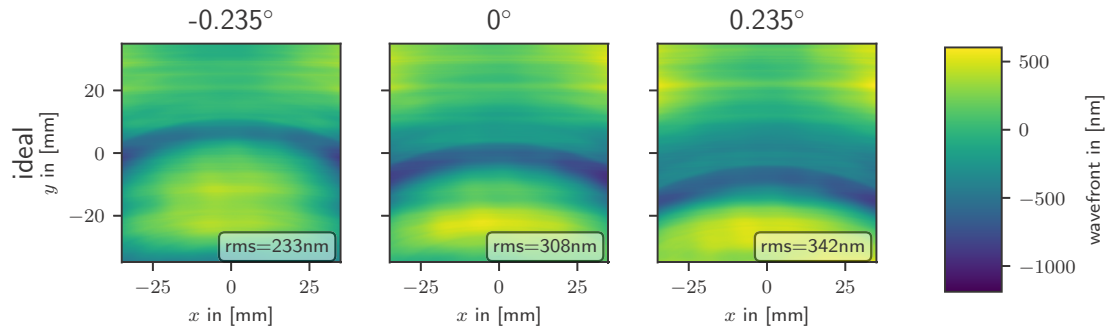


Figure 5.9.: Simulated wavefront of the setup under real conditions for incident angles of -0.235° , 0° and 0.235° . The rms errors are included in the corresponding figures. The wavelength is $\lambda = 632.8$ nm.

For the sake of completeness, the corresponding geometric spot diagrams are shown in Figure 5.10. The rms-radius of the spot is increased by a factor of six to 0.06 mrad for the central field of view. The degradation along the y -axis is observed to be dominant. A possible reason for this, is the present symmetry along the y -axis of the surface deformations induced by the shifted turning centers during the manufacturing process.

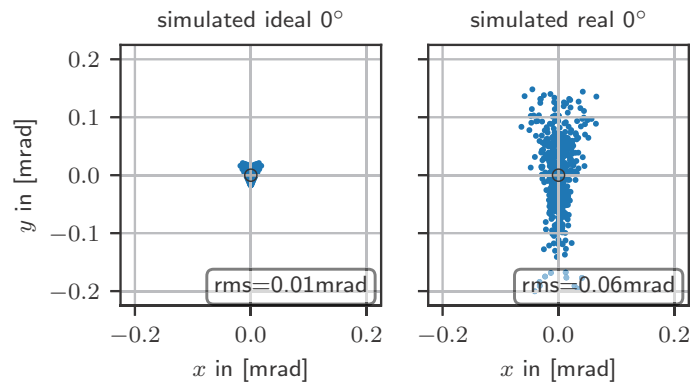


Figure 5.10.: Simulated geometric spot diagram of the setup under ideal (left) and real conditions (right) for the central field of view. The black circle represents the Airy-radius. The rms radii are included in the corresponding figures and the wavelength is $\lambda = 632.8$ nm.

The anamorphic telescope was assembled and adjusted by the Fraunhofer IOF, Jena.

Afterwards, the wavefronts in the exit pupil of the system were interferometrically measured in a double pass arrangement. The light source is a Helium-Neon laser with a wavelength of 632.8 nm. By a quantitative comparison with the experimental data, the approach should be verified for tolerancing and an easier alignment.

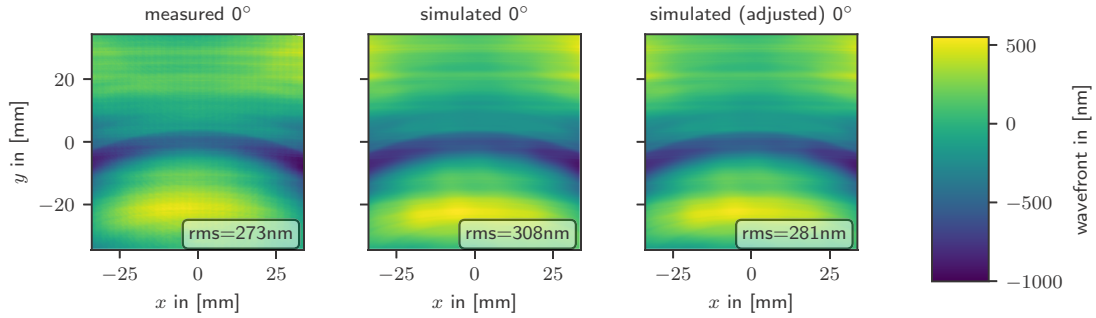


Figure 5.11.: Measured (left) and simulated wavefront (center) of the afocal telescope for the central field of view. The impact of the manufactured components is included. In addition, an adjustment (shift and tilt) of the two substrates is made (right). The rms errors are included in the corresponding figures. The wavelength is $\lambda = 632.8$ nm.

In Figure 5.11, the measurement of the OPD is compared with the simulated wavefront for the central field. Without any further adjustments, so based on the ideal, as designed coordinates, the rms error of the measured OPD (rms = 273 nm) is lower compared to the simulation (rms = 308 nm). This could be explained by the fact that the final system is adjusted in order to minimize the rms value of the wavefront and thus, certain aberrations are balanced by a shift or tilt of the components. In order to further improve the correlation, a shift and a tilt between the two mirror bodies M1M3 and M2M4 is included into the simulation. The result is displayed in the outer right wavefront of Figure 5.11. Qualitatively, not only a good match of the figure error but also of the characteristic MSF structures is achieved. Quantitatively, the deviation between the adjusted simulation and the corresponding measurement is only 2.9% with respect to the rms error. The results for all studied, individual fields of view are represented in Figure 5.12. Again, the simulation is allowed for an adjustment, shift and tilt, of the two substrates. The values are obtained by a simple optimization supported by the flexible coordinate systems defined in the software platform introduced in Chapter 3.

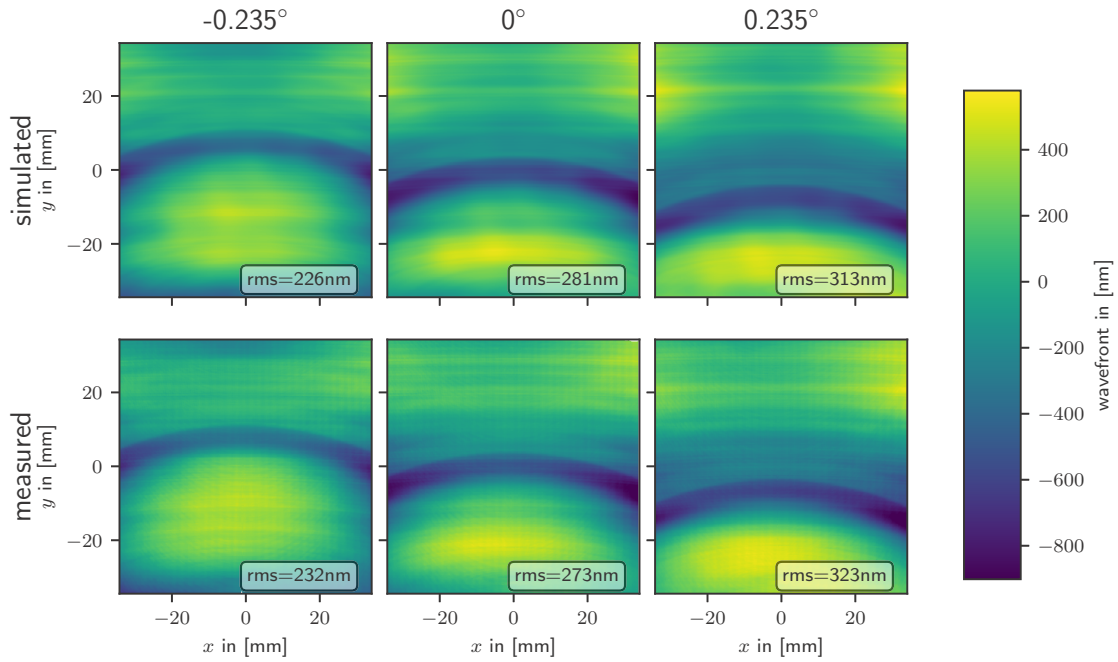


Figure 5.12.: Simulated wavefronts under real conditions for incident angles of -0.235° , 0° and 0.235° (top row) and corresponding measurement (bottom row) of the assembled setup. The rms errors are included in the corresponding figures. The wavelength is $\lambda = 632.8$ nm.

Besides a good qualitative match for the two outer fields, the deviation of the rms error is only 2.6 % and 3.0 %, for an incident angle of 0.235° and -0.235° , respectively. Another criterion, typically used for the comparison between two images, is the normalized correlation [137]. For all fields of view, a normalized correlation over 98 % is achieved. Possible reasons for the low residual deviations are measurement errors not only of the surface profiles but also of the experimental evaluation of the wavefront. Further, the alignment process of the system is incorporated with a certain error. So far, only a tilt and a shift of the shared mirror bodies M1M3 and M2M4 is considered.

In summary, the overall good qualitative and quantitative correlation between the simulation and the measurement shows the benefits of a more holistic simulation approach. Further, the achieved result verifies the developed approach for a comprehensive tolerancing and specification of the surface shapes. This is demonstrated and discussed within the next section.

5.4. Tolerance analysis

The analytic representation of the real optical surfaces, introduced in Section 5.1, allows for a comprehensive shape tolerancing of the components. By a systematic variation of the individual description coefficients, the influence of the corresponding surface deformation on the optical performance can be simulated. This can be done independently for both the figure and the MSF errors. In comparison to existing tolerancing methods, which are dragging the phase difference along the original rays [41, 134], the presented approach is not limited on the surface height of the features and the positioning of the individual components. In the following, two simple examples for a possible tolerancing analysis are studied based on the manufactured surfaces of the anamorphic imaging telescope.

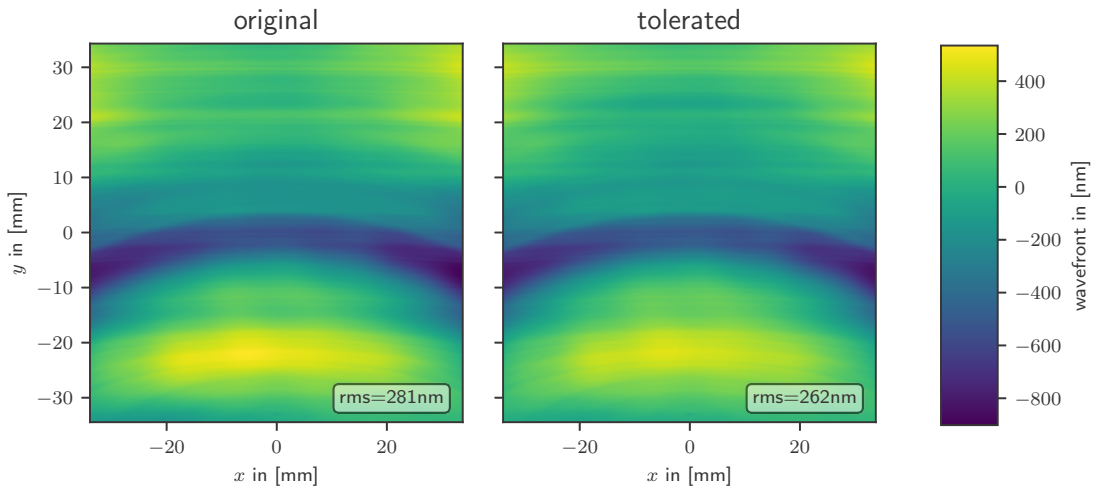


Figure 5.13.: Simulated wavefront of the original setup (left) and with a by 50% reduced figure error of the mirrors M1 and M3, manufactured on the same substrate (right). The rms errors are included in the corresponding figures. The wavelength is $\lambda = 632.8$ nm.

The first case study focuses on the figure error. Therefore, the figure error of the first and the third mirror, which are manufactured during the same process on a common substrate, is assumed to be reduced by 50% in height. This can be achieved by either a statistical variation of the RBF coefficients or by simply reducing all coefficient c_n by the same factor. In Figure 5.13, the result with a reduced figure error is compared to the original wavefront for the central field. While the MSF-ripples are

not affected, the overall rms-error is reduced by 7%. The dominating influence on the figure error is still the surface deviation of the last mirror M4.

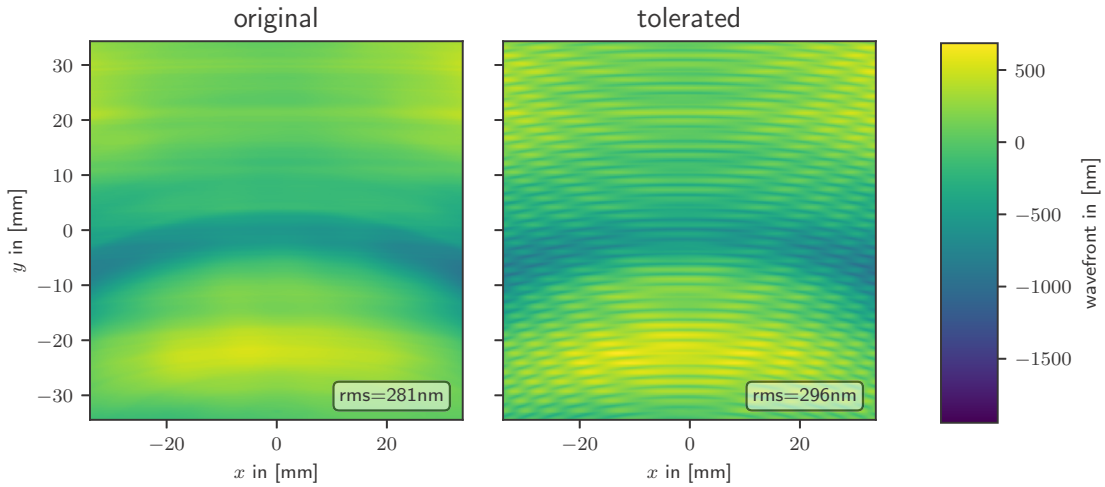


Figure 5.14.: Simulated wavefront of the original setup (left) and for artificial MSF-structures ($a = 50 \text{ nm}$, $\nu = 0.5 \text{ mm}^{-1}$) on the mirrors M2 and M4, manufactured on the same substrate (right). The rms errors are included in the corresponding figures. The wavelength is $\lambda = 632.8 \text{ nm}$.

The tolerancing of the regular ripple structures can be done by a variation of the coefficients a_n and b_n for certain spatial frequencies. In Figure 5.14, the result is presented for artificial surface ripples on the mirrors M2 and M4. The center of the ripples on the common substrate is defined to be the same as that of the diamond-turning process. The amplitude of the ripples is set to $a = 50 \text{ nm}$ and the spatial frequency to $\nu = 0.5 \text{ mm}^{-1}$. The rms-error is increased to 296 nm. Dependent on the position of the individual surface relative to the systems pupil, sum- and difference-frequencies of the ripples arise in the wavefront [138].

In addition, common errors during the alignment process, such as tilt and decenter, can be included, as demonstrated in Section 5.3. An even more comprehensive surface analysis can be for example realized by a statistical variation of the surface description according to a Monte-Carlo-simulation [139].

6. Holistic simulation of a table-top scattering setup

Within this chapter, it is demonstrated that a more refined approach for the simulation of modern optical systems offers new opportunities in performance prediction and the foundation for further improvements of the system. As an example system, a compact setup for angle resolved light scattering (ARS) measurements is selected, which was developed and assembled by the Fraunhofer IOF, Jena [140]. In Figure 6.1, the high sensitive optical roughness sensor (HOROS) is shown. The underlying concept is the detection and analysis of the light, which is scattered at a sample. During the fabrication of optical components, this kind of technology enables the fast and contactless assessment of imperfections, such as roughness or local defects, on thin-film coatings and substrates [45, 141, 142]. The challenge for the realization and the simulation is the necessary sensitivity over several orders of magnitude in intensity.

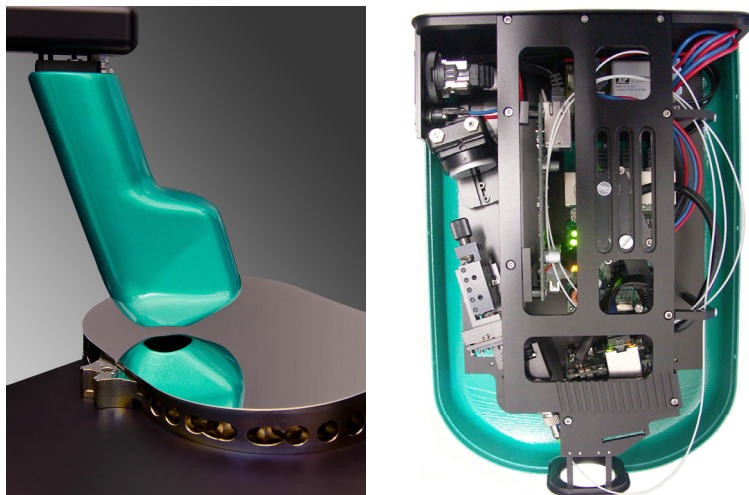


Figure 6.1.: High sensitive optical roughness sensor (HOROS) [140].

Relevant physical aspects for the performance prediction of the setup are the propagation of the light through the optical system and the scattering at relevant components. A critical point, which is assumed to have an influence on the small angle scattering, is the beam quality of the used light source. In the HOROS setup, a fiber coupled laser diode with a micro-focus module is installed. In order to include the impact of the technological aspects of the light source into the simulation of the system, the field of the monochromatic beam is reconstructed by a modified phase retrieval approach based on the transport of intensity equation [46]. Their application has been already successfully demonstrated for the evaluation of adaptive optics [143] and coherent phase microscopy [144]. Based on a simple and flexible setup, an accuracy comparable to a Hartmann-Shack-Sensor [145] is achieved. In contrast to algorithms relying on the inverse Fourier transform (IFTA) [146], convergence problems dependent on the application are avoided. Another technical aspect, which is investigated in this work, is the integration of a cover glass to protect the system in industrial applications. Here, multiple reflections of the light need to be considered. Apart from this, the final result of the setup is obtained by signal processing algorithms. With respect to Chapter 3, an overview of the addressed points for a more holistic simulation of the HOROS setup is given in Table 6.1.

	physical effects	real light sources	real manufactured components	signal processing
HOROS scattering setup	x	x	x	x

Table 6.1.: Overview of selected key aspects, addressed in the simulation of the HOROS table-top scattering system.

This chapter is structured as follows. In Section 6.1, the characterization of the used laser light source based on a modified phase retrieval approach is presented, the experimental results are analyzed and an estimate for the achieved accuracy is given. Then, the overall simulation concept of the system is outlined and several modules, such as the applied signal processing, are studied in more detail. At the end of Section 6.2, the results of the simulation are discussed. In Section 6.3, a cover glass to protect the system and the corresponding multiple reflections are included. The obtained scattering distributions are compared to experimental data.

Parts of the results are in preparation for publication.

6.1. Characterization of the real light source by phase retrieval

Before the experimental setup and the results for the used light source of the scattering setup are discussed, the basic approach to reconstruct the phase of a coherent beam is presented based on several measurements of the intensity distribution at different positions. For this purpose, the transport of intensity equation (TIE), derived from the paraxial wave equation in Section 2.1.2,

$$-k \frac{\partial I(\mathbf{r})}{\partial z} = \nabla_{\perp} I(\mathbf{r}) \cdot \nabla_{\perp} \phi(\mathbf{r}) + I(\mathbf{r}) \nabla_{\perp}^2 \phi(\mathbf{r}) \quad (6.1)$$

is used, where $I(\mathbf{r})$ is the intensity, $\phi(\mathbf{r})$ is the phase and ∇_{\perp} is the lateral nabla operator. Instead of solving the differential equation by direct numerical integration, in this work, Equation 6.1 is reformulated into a problem specific system of linear equations in order to allow for a numerical robust solution. Therefore, the phase in the plane of reconstruction $z = z_0$ is decomposed into the paraxial properties of a typical laser beam consisting of tilt and curvature, and residual higher order terms

$$\phi(x, y, z_0) = \phi_{\text{tilt}}(x, y) + \phi_{\text{curv}}(x, y) + \phi_{\text{res}}(x, y), \quad (6.2)$$

$$= k(t_x x + t_y y) + k \left(\frac{c_x}{2} x^2 + \frac{c_y}{2} y^2 \right) \quad (6.3)$$

$$+ \sum_n c_n \varphi_{\text{RBF}}(x - x_n, y - y_n, \epsilon_n). \quad (6.4)$$

The tilt and curvature terms are determined by evaluating the first and second moments. The residual higher order terms are described by lateral shifted RBFs $\varphi_{\text{RBF}}(x - x_n, y - y_n, \epsilon_n)$, which are introduced in Section 2.3. Here, Gaussian functions, distributed on a Fibonacci grid, are used. In comparison to global polynomials, the critical definition of the norm radius and the handling at the boundary are avoided [67]. By inserting the linear combination of RBFs into Equation 6.1, a system of linear equations is achieved

$$\begin{aligned}
-k \frac{\partial I(\mathbf{r})}{\partial z} \Big|_{z=z_0} &= k [\partial_x I(x, y) t_x + \partial_y I(x, y) t_y] \\
&+ k [\partial_x I(x, y) c_x x + \partial_y I(x, y) c_y y + I(x, y) c_x + I(x, y) c_y] \\
&+ \sum_{n=1}^N c_n [\partial_x I(x, y) \partial_x \varphi_{\text{RBF}}(x - x_n, y - y_n, \epsilon_n) \\
&\quad + \partial_y I(x, y) \partial_y \varphi_{\text{RBF}}(x - x_n, y - y_n, \epsilon_n) \\
&\quad + I(x, y) \partial_{xx} \varphi_{\text{RBF}}(x - x_n, y - y_n, \epsilon_n) \\
&\quad + I(x, y) \partial_{yy} \varphi_{\text{RBF}}(x - x_n, y - y_n, \epsilon_n)].
\end{aligned} \tag{6.5}$$

To retrieve the phase in the desired plane, the linear system is solved for the coefficients c_n by a LSQ approximation according to Section 2.3.

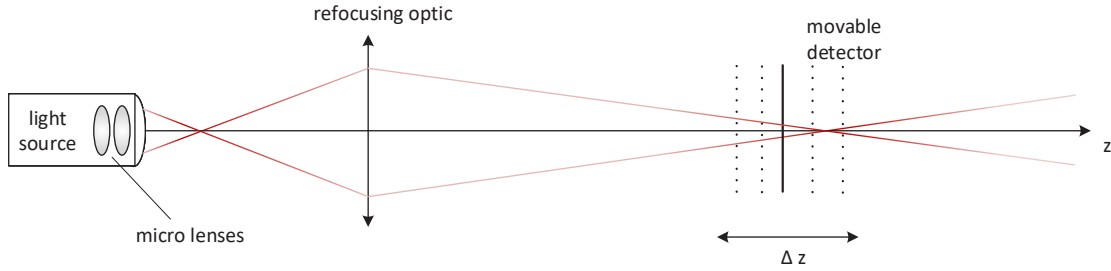


Figure 6.2.: Paraxial layout of the experimental setup. The light beam to retrieve is transformed by a refocusing optics onto a movable detector. The intensity distribution is captured in several planes along the z -axis.

In the HOROS setup, a laser diode (λ -mini, RGB-Photonics GmbH, Kelheim) is used. The wavelength is measured to be $\lambda = 662.5 \text{ nm}$ at $P = 1 \text{ mW}$ with a spectral width of $\Delta\lambda_{\text{FWHM}} = 0.7 \text{ nm}$, which is neglected in the following considerations. The monochromatic light is coupled into a single-mode fiber for homogenization before it is collimated and focused by a compact lens module (60FC-4-M12-33, Schäfter+Kirchoff GmbH, Hamburg). Due to the fact that the necessary specifications for including the focusing module into the simulation are not known, the phase and intensity in a selected plane are reconstructed. In order to characterize the light source by the TIE, the intensity needs to be measured in several planes along z . In Figure 6.2, the experimental setup is sketched. The light beam to retrieve is transformed by a refocusing optic to enhance the lateral resolution of the field

distribution on the detector and the axial resolution along z . The latter is limited by the specifications of the dynamic stage (M-ILS300LM-S, Newport Corporation, Irvine), which is used to shift the detector. Optimal parameters for the positioning and the refocusing optics are evaluated theoretically in [144] and in [46,147] based on synthetic data. For the particular example, 100 images are recorded within a range of $\Delta z = \pm 15$ mm close to the beams focus. For the magnification of the beam, a doublet with a focal length of $f = 50$ mm is used (AC254-050-A, Thorlabs GmbH, Dachau), which additional aberrations are later considered in the reconstruction process. The intensity is captured by a 12-bit camera (SP928, Ophir Spiricon Europe GmbH, Darmstadt) with a pixel size of $3.69 \mu\text{m}$ by $3.69 \mu\text{m}$. In order to reduce the noise and enhance the dynamic range of the images, multiple measurements are averaged and several different exposures are combined by a high-dynamic-range (HDR) algorithm [148]. Afterwards, Equation 6.5 is solved with $N = 5000$ RBFs for the measured data. To minimize the influence of the residual noise, the derivatives of the intensity are numerically evaluated by a slowly oscillating Savitzky-Golay filter [149]. The result is verified by a free-space propagation, introduced in Section 2.1, of the retrieved field into different planes along z and subsequent comparison to the measured intensities. By capturing an additional stack of images, the range for verification Δz is extended to 300 mm.

In Figure 6.3, the result of the retrieval process is shown. In the upper row, the measured intensities along z , and in the center row, the propagated intensities based on the retrieved field are displayed for comparison. The residual deviations $\Delta I(x, y)$ with an intensity weighted rms error up to 8 % are shown below. Similar to [150,151], the quantitative measure is defined by

$$\text{rms}(\Delta I(x, y)) = \sqrt{\frac{\iint \Delta I(x, y)^2 I_w(x, y) dx dy}{\iint I_w(x, y) dx dy}}, \quad (6.6)$$

where the weighting function $I_w(x, y)$ corresponds to the measured intensity. The corresponding, centered cross-sections of the measured and retrieved beams are presented in Figure 6.4. Along the entire axial range, a good qualitative and quantitative match is achieved. By investigating the oscillation of the intensity on the optical axis before the focus of the beam, spherical aberrations are identified.

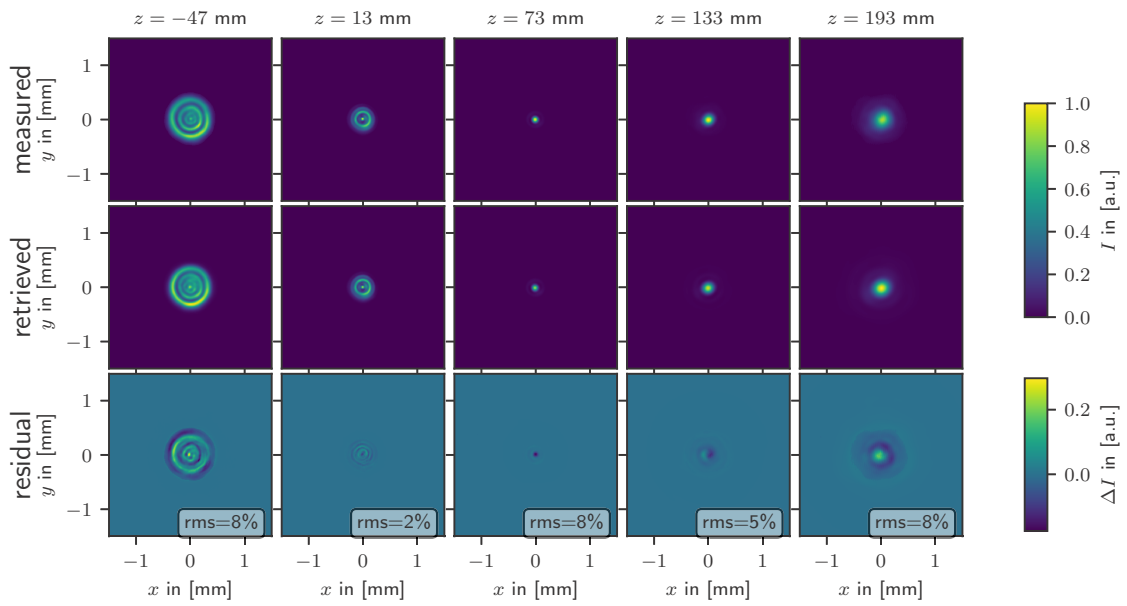


Figure 6.3.: Measured intensity of the real light source at different positions along the z -axis and corresponding distributions based on the retrieved field. The values are normalized in each plane on the maximum intensity. The residual deviations with the corresponding weighted rms error are shown in the bottom row.

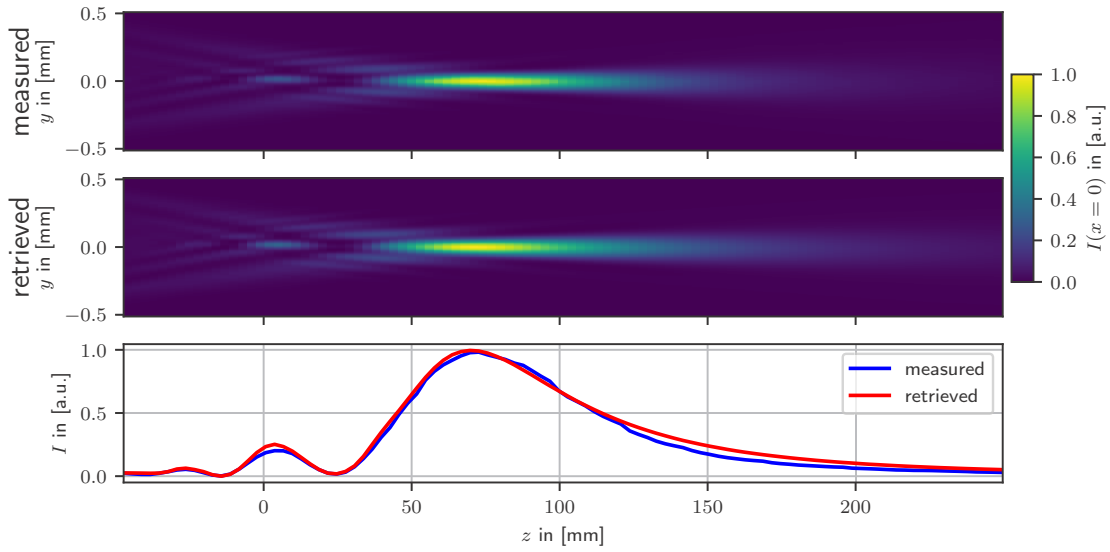


Figure 6.4.: Two-dimensional cross-sections $I(x = 0, y, z)$ of the measured intensity of the real light source and the retrieved beam. The values are normalized on the maximum intensity. Below, the corresponding one-dimensional cross-sections $I(x = 0, y = 0, z)$ are plotted.

Before estimating the accuracy of the procedure and discussing residual deviations in detail, the retrieved field is propagated back into the plane of interest, where it is used for further simulations. The influence of the refocusing optic is taken into account by geometrical optics. In Figure 6.5, the characterized field in the focal plane of the particular light source is shown. Due to symmetry observations [81], spherical aberrations are identified by the radial rings around the peak of the field and astigmatism by the double plane symmetry of the distribution. Furthermore, coma is observed due to the asymmetry of the cross-sections. This is confirmed, by a Zernike-Fringe fit of the wavefront at the last surface of the micro-focus module [152]. The result for the primary aberrations is shown in Table 6.2. Possible reasons for the perturbed beam are residual imperfections coming from the manufacturing and the alignment of the compact lens module. Especially, the distance between the two micro lenses, indicated in Figure 6.2, and the orientation of the second lens are difficult to handle.

In general, the noise of the captured images is the most critical parameter for the quality of the procedure. In general, the noise is handled by an averaging over several images, a subtraction of the background signal and the combination of multiple

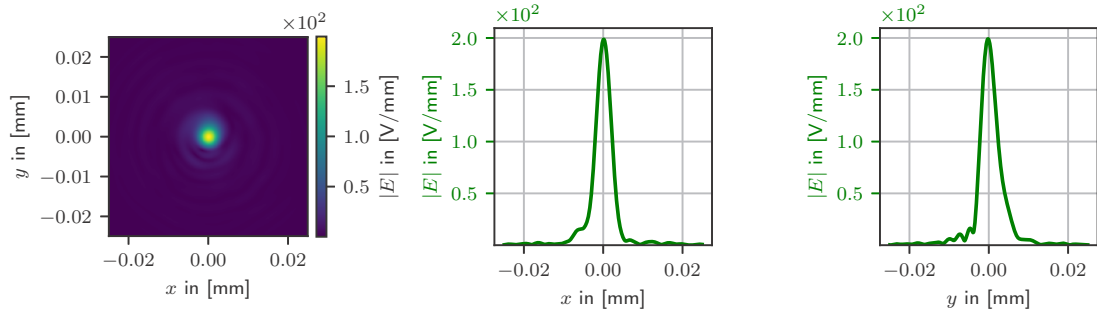


Figure 6.5.: Electric field distribution of the retrieved light source close to the focal plane and corresponding cross-sections. The total power is normalized to $P = 1$ mW and the wavelength is $\lambda = 662.5$ nm.

astigmatism	coma	spherical aberrations
$c_5 = -0.07\lambda$	$c_7 = -0.06\lambda$	$c_9 = +0.38\lambda$
$c_6 = -0.02\lambda$	$c_8 = -0.18\lambda$	

Table 6.2.: Primary aberrations based on a Zernike-Fringe fit of the wavefront at the exit surface of the real light source. The norm radius is $R_n = 2.5$ mm.

exposures by the HDR-algorithm. For phase retrieval algorithms, it is common, to estimate the accuracy by an evaluation of synthetic data, perturbed by noise [46,144]. Therefore, a Gaussian intensity profile with an aberrated phase, comparable to the studied example, is propagated into several planes z_i . Afterwards, the TIE is solved based on the synthetic intensities, perturbed with different levels of additive + and multiplicative * noise, defined by a centered normal distribution N with standard deviation σ ,

$$I_p(x, y, z_i) = I(x, y, z_i) \cdot (1 + N(\sigma_*)) + \max [(I(x, y, z_i)) \cdot N(\sigma_+)]. \quad (6.7)$$

Here, the additive term models white noise and the multiplicative part accounts for nonlinearities and blooming effects of the detector. In order to address the quality of the characterization, the retrieved field is then compared to the original data, 150 mm apart from the plane of retrieval to include the influence of the free-space propagation. In Figure 6.6, the signal weighted rms error of the intensity and of the wavefront deviations are plotted for different noise levels. The constant small error for low noise levels is coming from the evaluation of the system of linear equations

and the numerical free-space propagation. The additive noise is observed to be more critical than the multiplicative noise. According to Figure 6.3, an rms error in intensity between 2 and 8 % is achieved. Therefore, the accuracy of the approach is estimated based on the results for synthetic data in Figure 6.6 to be around $\lambda/100$. If a higher accuracy is necessary, the noise needs to be better controlled. For example, a wavefront error around $\lambda/1000$ corresponds to a noise level below 10^{-6} .

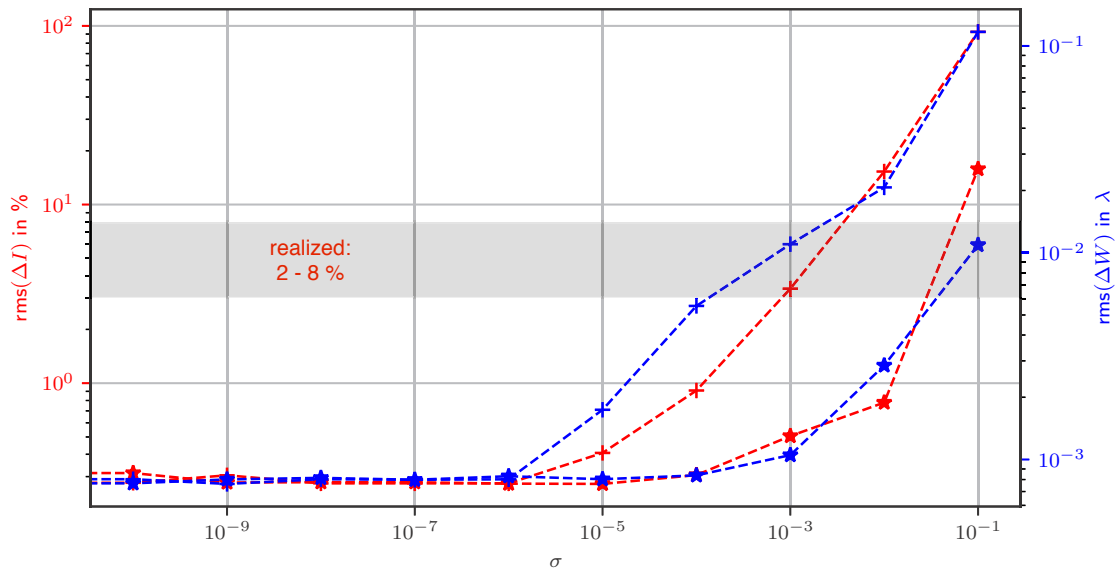


Figure 6.6.: Intensity weighted rms errors of the wavefront deviations $\text{rms}(\Delta W)$ (blue) and the intensity deviations $\text{rms}(\Delta I)$ (red) for different additive (+) and multiplicative (*) noise levels σ , evaluated 150 mm apart from the plane of retrieval to include the influence of the free-space propagation.

Further deviations might arise due to the final propagation of the retrieved field into the plane of interest. Based on estimated alignment-uncertainties of the used refocusing optic, the possible impact on the final result is evaluated by ray tracing simulations. For a tilt of $\pm 0.5^\circ$ and a decenter of ± 0.1 mm, the final accuracy of the retrieved coma and astigmatism is expected to be better than $\lambda/25$. If a higher accuracy is necessary for the application, the usage of a better corrected refocusing optic, such as a microscopic lens, is recommended. Residual manufacturing imperfections are not considered so far, but can be included in the future.

6.2. Simulation concept of the system

The simulation of the compact scattering setup is based on the concept for a more holistic description, which is introduced in Chapter 3. In Figure 6.7 (left), the optical layout of the system is sketched. The monochromatic light beam, emitted by a fiber coupled laser diode, is focused with a compact objective lens onto a pinhole, which acts as a spatial filter. To obtain the scattered reflected light of the sample in the far field, the light distribution at the pinhole is imaged by a spherical shaped mirror on a matrix detector apart from the sample. To avoid direct reflexes, the detector is tilted by 28° towards the incoming beam. Corresponding distances are given within Figure 6.7 (left).

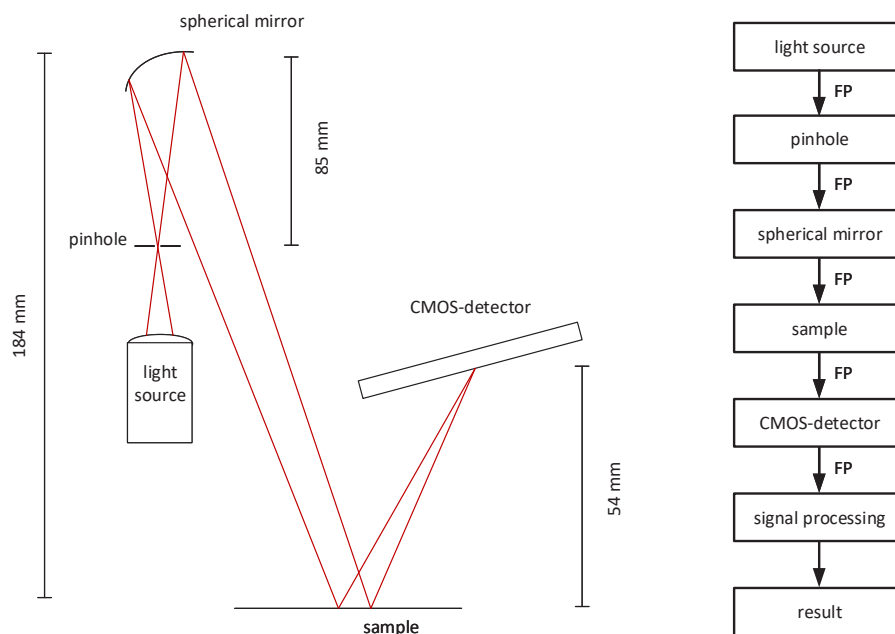


Figure 6.7.: Optical (left) and simulation (right) layout of the example system. FP denotes free-space propagation.

The layout of the simulation is sketched in Figure 6.7 (right) with regard to Chapter 3. So far, the sequence of calculation corresponds to a linear arrangement. This will become more complex in Section 6.3, when a cover glass is inserted above the sample. In the following, the used methods and assumptions within the individual modules are briefly discussed. The connection of the individual components is handled by free-space propagation algorithms based on the angular spectrum of plane

waves, which are introduced in Section 2.1.

Light source

For the integration of the real light source, the final result of Section 6.1 is used. The characterization by phase retrieval overcomes the problem of incomplete known data of the used laser diode and compact lens module. Furthermore, also technological aspects, such as manufacturing imperfections or a misalignment are now included. A circular aperture is part of the micro-focus module to allow for a flexible adjustment of the numerical aperture of the source. In addition, a linear polarizer is installed in the experimental setup. Therefore, the beam is defined to be linear polarized. To study the impact of the real light source, an ideal Gaussian beam with a waist of $w_0 = 2.5 \mu\text{m}$ is defined according to Equation 3.2 for comparison. All results are based on a total power of $P = 1 \text{ mW}$.

Pinhole

A pinhole with a diameter of $150 \mu\text{m}$ is used as a spatial filter, which ideally blocks all stray light from the light source. In the simulation, the pinhole is considered by a circular aperture mask. Manufacturing imperfection and possible scattering within the hole are not included so far.

Spherical mirror

The spherical mirror with a radius of curvature of $r = 125 \text{ mm}$ and a clear aperture of 15 mm is modeled according to Section 3.2. From the viewpoint of optical design, the optimal shape of the tilted mirror (3°), in order to prevent an aberration of the beam, would be an ellipse, which allows for perfect stigmatic imaging. As a consequence, the near angle scattered light around the specular reflex would be better accessible. However, the residual roughness of the manufactured substrate, and therefore the parasitic contribution to the scattered light, would be larger compared to a highly polished spherical mirror. Based on the investigations in [153], the last component before the sample, which is the considered mirror, has the largest impact on the signature and the final sensitivity of the system. Therefore, the scattering of the

field at the mirror is included according to Section 6 based on the assumption of a perfectly conducting substrate. For the highly polished surface, the condition of small surface height variations is fulfilled and thus, the vector perturbation theory is applied. The statistical scattering amplitude is evaluated up to the second order by flattening the field and the mirror in paraxial approximation. In Figure 6.8, measured PSDs of the mirror are presented, which are obtained by the Fraunhofer IOF Jena in different setups and combined to a model PSD [154]. The result is used for the scattering simulations in this work.

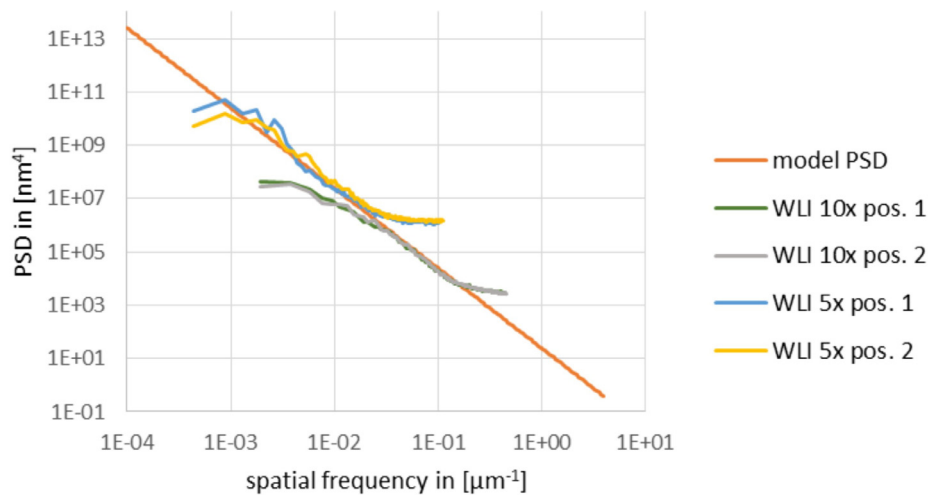


Figure 6.8.: Measured PSDs of the spherical mirror and corresponding model PSD [154]. The surface is characterized at two positions by white-light interferometry (WLI) with different magnifications.

Sample

In principle, the scattering at the sample can be handled according to the methods described for the spherical mirror. Instead of the SPM, for local surface defects, the tangent plane approximation, which is introduced in Section 6, can be applied [45]. Within this work, the focus is on the evaluation of the systems signature. For corresponding measurements, a super polished silicon wafer is used, whose additional scattering is not included so far but can be part of future research if corresponding surface measurements are provided.

CMOS-detector and signal processing

In contrast to goniometer based setups [155], the scattered light is captured without scanning procedures by a matrix detector (MV1-D2080-160G2, Photonfocus AG, Lachen) with a corrected non-linear response [140]. The resolution is 2080 by 2080 pixels with a pitch of 8 μm .

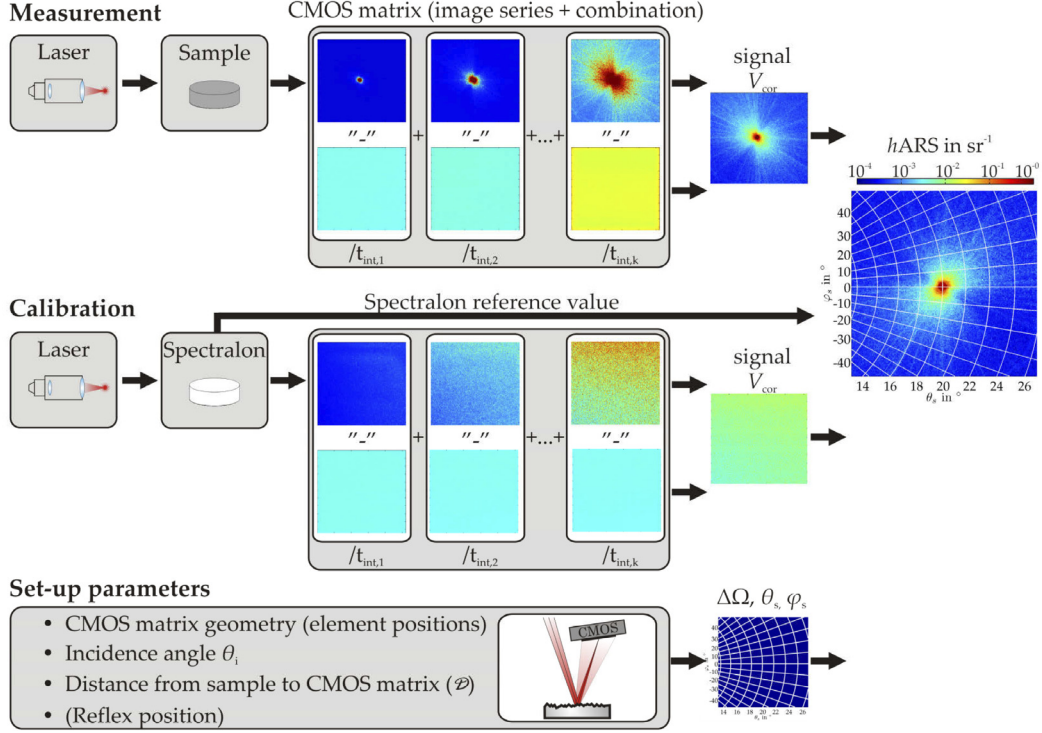


Figure 6.9.: Illustration of the applied signal processing in the HOROS setup. [140]

The overall scheme of the signal processing is shown in Figure 6.9. Due to the limited dynamic range of the detector, the final distribution is obtained by a combination of several images with different exposure times according to [148]. Here, the background noise is subtracted for each individual exposure. The ARS is then finally calculated by [156]

$$\text{ARS}(\theta_s, \phi_s) = \frac{\Delta P_s(\theta_s, \phi_s)}{P_i \Delta\Omega_s}, \quad (6.8)$$

where the scattered power ΔP_s is proportional to the signal of the detector V_{cor} .

The scattering angles, θ_s and ϕ_s , and the solid angle $\Delta\Omega_s$ are determined based on the geometries of the detector with respect to the sample. Unfortunately, the total input power on the detector P_i cannot be measured directly because the high intensity in the focal spot exceeds the saturation level of the detector. Instead, a calibration with a known ARS distribution is performed to get a signal proportional to the input power. Based on the final scattering distribution, the PSD of the sample is then evaluated under the limitations of the SPM for single metallic or dielectric surfaces by [157]

$$PSD(\nu_x, \nu_y) = \frac{\lambda^4}{16\pi^2 \cos^2 \theta_s \cos \theta_i Q} ARS(\theta_s, \phi_s), \quad (6.9)$$

$$\nu_x = \frac{1}{\lambda}(\sin \theta_s \cos \phi_s - \sin \theta_i), \quad (6.10)$$

$$\nu_y = \frac{1}{\lambda}(\sin \theta_s \sin \phi_s). \quad (6.11)$$

Here, θ_i is the incident angle on the surface and Q is a factor dependent on the sample, the geometry of the setup and the polarization of the light [59]. Finally, the rms roughness σ_r , which is typically used as a quantitative measure for the surface quality [158], is calculated by

$$\sigma_r = \sqrt{\iint PSD(\nu_x, \nu_y) d\nu_x d\nu_y}. \quad (6.12)$$

The region around the specular reflex is excluded by calculating its position and defining a minimum considered spatial frequency.

In summary, the simulation follows the same signal processing concept except for the calibration procedure by a reference sample. This impact is not included in the following results.

In a first step, the differences between the ideal and the real light source are analyzed. Therefore, the simulation is performed making use of the full numerical aperture without shutting down the circular aperture of the light source. In Figure 6.10, the ARS distributions at the detector in an area around the focal spot are shown for comparison. In both distributions, an asymmetrical shape, which is

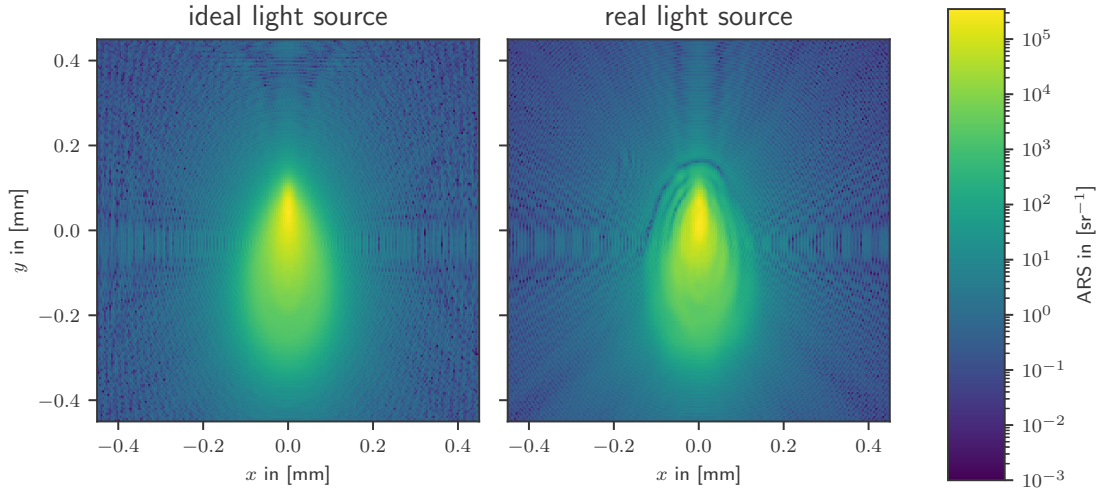


Figure 6.10.: Two-dimensional simulated ARS distributions of the setup based on the ideal and the real light source. A subarea of the detector around the focal spot is selected. The coordinates of the detector corresponds to scattering angles between $\theta_s = 17.6^\circ$ and 18.4° , and $\phi_s = -1.6^\circ$ and 1.6° , relative to the sample.

perpendicular to the rotation axis of the mirror, is observed. This comes from the reflection at the spherical mirror under a finite angle and the resulting coma aberrations. In contrast to the ideal Gaussian beam, the spot of the real light source is further disturbed by the aberrations introduced due to the micro-focus module. In principle, the additional spherical aberrations lead to the pronounced rings. It is worth mentioning, that the diffraction structures along the axes are influenced to a certain degree by artifacts coming from the discretization of the circular apertures [159]. In the current configuration, the sensitivity of the system for detecting the scattered light of the sample, is mainly limited by the aberrations origin from the tilted spherical mirror and not by the impact of the real light source. This will become different, if an elliptical substrate is used instead of the spherical one. Assuming a perfect substrate without any manufacturing deformations, the near angle sensitivity will be more influenced by the aberrations of the real source.

In contrast to previous studies, the assembled setup is used with a reduced numerical aperture to overcome the described problems and to increase the sensitivity. Therefore, the diaphragm behind the light source is shut down and thus, the size of the focal spot at the pinhole is increased. As a consequence of the almost uniform illumination, the field at the pinhole corresponds now to an Airy instead of a nearly

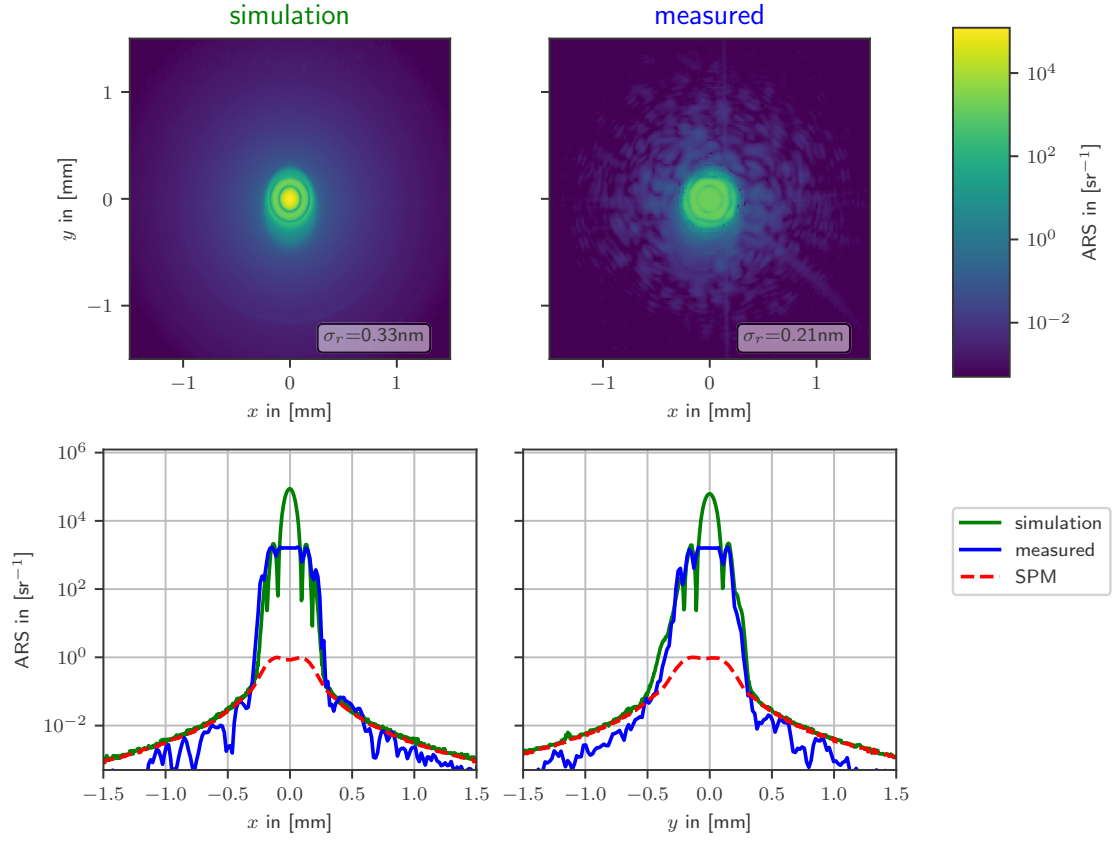


Figure 6.11.: Two-dimensional simulated and measured ARS distributions of the setup and evaluated rms roughness σ_r . A subarea of the detector around the focal spot is selected. The corresponding cross-sections are shown in the bottom row and the contribution of the scattering is indicated (red). The coordinates of the detector corresponds to scattering angles between $\theta_s = 16.5^\circ$ and 19.5° , and $\phi_s = -5.6^\circ$ and 5.6° , relative to the sample.

Gaussian distribution. In an optimal configuration, the Airy distribution is cut at its first minimum by the pinhole in order to reduce edge diffraction and get a small spot at the detector. Due to the reduced numerical aperture, the aberrations of the tilted spherical mirror and diffraction effects at its aperture are reduced. As a major drawback of this configuration, the theoretically achievable near angle sensitivity is declined due to the increased width of the specular reflex. In general, the reduction of the numerical aperture corresponds to a trade-off between increasing the final spot size and eliminating the aberrations from the spherical mirror and the impact of the light source. In Figure 6.11 (upper right), the measured ARS distribution, which was provided by the Fraunhofer IOF Jena, is shown for the described configuration. The data are clipped at a certain maximum intensity because of the limited exposure times of the used matrix detector. By analyzing the number of rings of the observed ARS, the diameter of the used pinhole is found to be too large. Instead of cutting the Airy distribution at its first minimum, the first and part of the second maximum can be seen. In addition, the pinhole seems to be decentered, what will be confirmed by the simulation. In Figure 6.11 (upper left), the corresponding result is presented. To better match the experimental results, the pinhole is shifted by $8\ \mu\text{m}$ along the y -axis in the simulation. The sensitivity of the system around the specular reflex is limited by a decreasing contribution, which is observed to be below $10^{-1}\ \text{sr}^{-1}$. This originates from the residual edge diffraction at the pinhole and the scattered light from the rough surface of the spherical mirror, whose impact is indicated in the corresponding cross-sections. While the overall shape of the simulated ARS coincides with the measured results, the observed pattern around the focal spot cannot be reproduced. One reason for this is the application of the azimuthal averaged, one-dimensional PSD, leading to an incoherent description of the scattering. Especially in the near angle domain, which corresponds to the low spatial frequencies of the PSD, the neglect of the phase is assumed to be critical. While the detailed evaluation of the accuracy of the used scattering models goes beyond the scope of this work, this should be investigated during further research. Furthermore, the contribution of the scattered intensity is almost linearly dependent on the measured PSD according to Equations 2.46 and 6.9. As a consequence, possible measurement errors have a large influence on the results. For the particular example, certain deviations, especially for low spatial frequencies, are expected according to the difference between the individual PSDs in Figure 6.8. This may also explain the differences between the simulated and the measured rms roughness. In addition, also the residual surface deviations of the used silicon wafer may have a

certain influence here, which can be included if certain measurements are provided. For a quantitative comparison of the focal spot, the recording of unclipped data would be necessary. This could be realized by the implementation of variable neutral density filters into the setup. Apart from this, further improvements could be achieved by including more possible alignment uncertainties, such as the positioning and orientation of the individual components. Before the results are summarized, the impact of a cover glass above the sample is studied.

6.3. Integration of a cover glass

For industrial applications, a cover glass becomes necessary to protect the system from environmental influences. Besides additional stray light, a major drawback of this implementation are multiple reflexes at the plane plate, which perturb the detected ARS distribution. As a final step, a cover glass is included into the simulation. In Figure 6.12 (left), the optical layout of the system, protected by a cover glass, is shown. In addition to the main specular reflex (dark red), several exemplary reflexes, external and internal, are indicated (light red). According to Chapter 3, the corresponding simulation layout is presented in Figure 6.12 (right). Dependent on the order of reflection within the cover glass, the resulting reflected or transmitted field is either propagated to the sample or the detector. Finally, the individual fields are superposed. Due to an incoherent description of the scattering, their individual intensity distributions are added.

The modeling of the cover glass follows the explanations in Section 3.2 for a plane plate. In addition, the field is split at each interface between two media into a reflected and transmitted part dependent on the properties of the cover glass. Up to a certain order, the individual fields are then further propagated through the system. For first investigations, an uncoated borosilicate float glass [160] with a thickness of 1 mm was selected by the Fraunhofer IOF Jena. The plane plate is positioned parallel to the sample in a distance of 5 mm. The additional scattering from the cover glass is not included into the simulation so far.

The results of the simulation are presented in Figure 6.13. For a first discussion, only external reflections at the plane plate are included. The lower spot at $y = -4$ mm correspond to the direct reflection of the incident beam at the cover glass. According

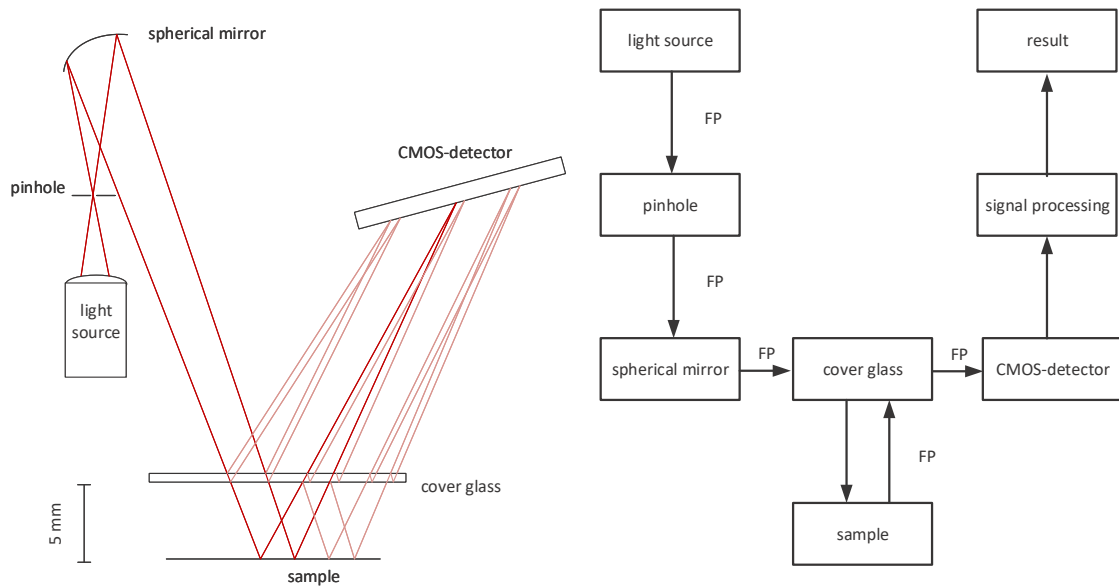


Figure 6.12.: Sketch of the optical (left) and the simulation (right) layout of the system, protected by a cover glass. In addition to the main specular reflex (dark red), several exemplary reflexes, external and internal, are indicated (light red).

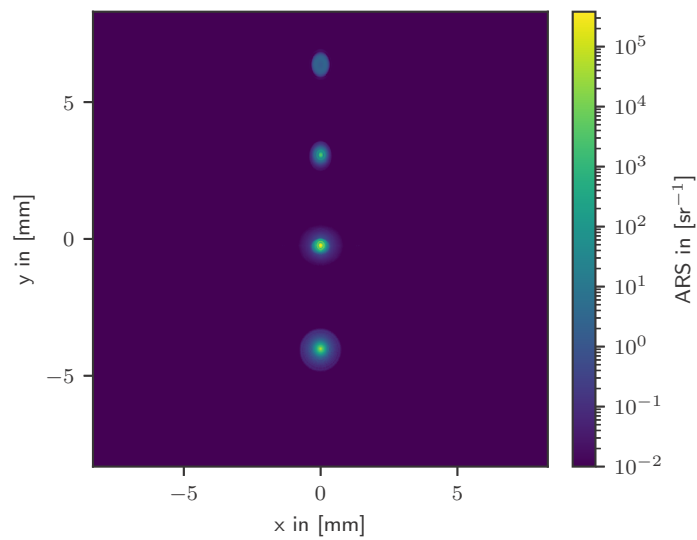


Figure 6.13.: Two-dimensional simulated ARS distributions of the setup with a cover glass. Only external reflections at the cover glass are included. The coordinates of the detector corresponds to scattering angles between $\theta_s = 9^\circ$ and 26° , and $\phi_s = -44^\circ$ and 44° , relative to the sample.

to the properties of the used material, the polarization of the light and an incident angle of 18° , the reflected power is around 4% of the total power of the incident beam. The reflex at $y = 3$ mm originates from a reflection at the cover glass after the beams interaction with the sample. With respect to the reflectivity of the sample, its power is around 0.4% of the incident power and is further decreased to 6×10^{-3} % if another reflection at the cover glass is considered.

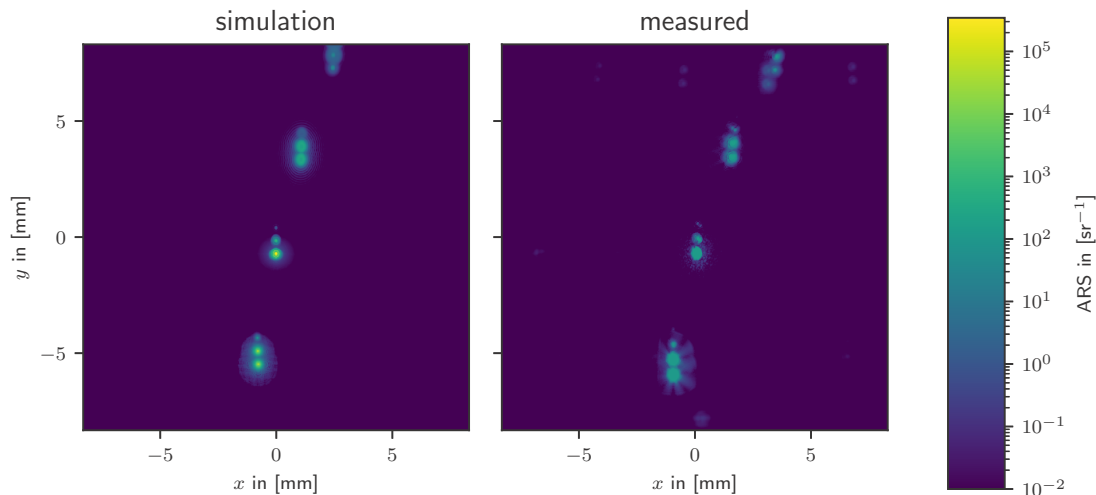


Figure 6.14.: Two-dimensional simulated and measured ARS distributions of the setup. The coordinates of the detector corresponds to scattering angles between $\theta_s = 9^\circ$ and 26° , and $\phi_s = -44^\circ$ and 44° , relative to the sample.

In Figure 6.14, the measured ARS distribution for the discussed configuration is shown. Unfortunately, the provided measurements are clipped at a certain intensity and the power calibration in this setup is quite critical. Therefore, the comparison with the simulation results is limited to a qualitative discussion. In order, to match the positions of the individual spots, the positioning and orientation of the cover glass is kept variable and optimized within the simulation. In this way, the plane plate is found to be shifted along the z -axis by 2 mm and tilted around its x - and y -axis by 0.2° and 0.6° , respectively. Not only for the external reflections but also for the multiple reflections within the cover glass, a qualitative performance prediction of the real system is achieved. While the same sources for deviations as discussed in Section 6.2 apply, additional reflections from the housing and the detector are not considered. The results could be further improved by taking more, unclipped measurements into account and optimizing additional degrees of freedom for the adjustment of the setup.

6.4. Summary

In this chapter, the capabilities of a more holistic simulation approach were demonstrated and refined performance predictions of the compact scattering sensor were achieved. Based on a modified phase retrieval approach, the illumination field behind the fiber-coupled laser diode and subsequent micro-focus module was characterized and its impact on the system analyzed. Furthermore, the scattered light at the spherical mirror was considered in the wave-optical simulation relying on perturbation theory. To access the ARS distribution and the final rms roughness, digital post-processing was included into the simulation. Finally, the use of a cover glass and resulting multiple reflections were studied. By a comparison to measured data, several points for further improvement of the simulation were investigated:

- So far, the provided measurements are clipped at a certain maximum intensity due to the limitations of the detector. This could be realized by the implementation of variable neutral density filters into the setup.
- The accuracy of available scattering models should be investigated during further research. Especially for small scattering angles, the transition between coherent and incoherent modeling is of interest.
- Improved surface measurements would allow for a more accurate simulation. For example, the approach for low and mid spatial frequencies, presented in Chapter 5, could be applied.

However, the presented results for a comprehensive simulation of the table-top scattering setup form the foundation for an extensive analysis and offer new possibilities for further optimization and improvement of the system:

- The impact of an elliptical mirror to reduce the aberrations can be virtually evaluated.
- Different light sources can be studied to improve the sensitivity.
- Optimal anti-reflection coatings for the cover glass can be investigated.
- A mechanical suppression of the reflexes by additional apertures or the digital removal by signal processing can be tested.

7. Conclusion and outlook

In this thesis, new approaches, which lead to a more holistic simulation of optical systems, were introduced and discussed. Based on several examples, it was successfully demonstrated that the concept of an aggregation of individual simulation models and the integration of technological aspects lead to an improved performance prediction and offers new opportunities. In the following, the major deliverables of this work are briefly summarized. In Chapter 3, a modular framework for a holistic description and simulation of modern optical systems was presented and exemplary filled for a thin-disk multipass amplifier. Physical effects, such as gain and absorption in the active medium, and a heat-induced deformation of the disk are taken into account and the degradation of the beam quality due to a misalignment was quantified. Afterwards, several new approaches for a more holistic model were presented. A new, quasi-fast algorithm for the coherent field propagation between tilted planes, which is based on a decomposition of the general rotation matrix, was introduced and compared to state-of-the-art solutions. A high accuracy, even for large rotation angles, was demonstrated based on several examples. In Chapter 5, performance limiting manufacturing errors of diamond-turned freeform surfaces are included into the simulation of an imaging system. The new approach is based on an analytic description of the measured surfaces with a priori knowledge of typical deformation profiles, which enables the performance prediction of even complex systems as a whole. For demonstration, an afocal, anamorphic imaging telescope was selected and the approach was verified by a comparison with measured wavefronts. Furthermore, the capabilities for a comprehensive analysis of the impact of figure errors and regular mid-spatial frequencies were pointed out by a variation of the surfaces coefficients. Based on the simulation of a table-top scattering setup, the more holistic approach was shown to offer new opportunities in performance prediction and the foundation for further improvements of the system. Not only physical effects, such as diffraction or scattering at rough surfaces, but also digital post-processing algorithms as well as real properties of the used light source were included. There-

fore, a modified approach for the characterization of coherent light beams based on the TIE was presented and applied. Furthermore, an estimate on the realized accuracy was given. The achieved results were qualitatively compared to measured scattering distributions and residual deviations were discussed. In summary, it was demonstrated that the comprehensive models allow for rather accurate performance predictions and enable fast virtual prototyping of new setups.

Motivated by the results of this thesis, there are several interesting points which can be addressed within future research. The simulation of the thin-disk multipass amplifier could be further improved by an extended modeling of the active medium, which takes polarization effects into account and regards the impact of thermal heating in more detail. Apart from this, also the consideration of temporal effects and the characterization of the input beam by the presented approach would be of interest. While a comparison with interpolation-based methods is already included within this thesis, the evaluation of possible differences between the introduced approach for the light propagation on tilted planes and algorithms relying on NFFTs could be part of future research. In addition, the approach for the description of real components could be further extended to other manufacturing technologies apart from diamond turning, such as molding or additive manufacturing. Furthermore, a comprehensive tolerancing analysis based on a statistical variation of the coefficients would be useful for the design process of modern, freeform-based systems. With regard to the simulation of the table-top scattering setup, several points are addressed in the corresponding sections, which should be clarified by improved measurements. Especially in the near angle domain, it is recommended to check the limits of available scattering models for different applications by a comprehensive experimental comparison. Additionally, the system can be further optimized based on the achieved results. For example, the evaluation of the impact of an elliptical mirror, different anti-reflection coatings or improved software algorithms could be part of future investigations. Apart from this, a possible extension of the approach for the characterization of real light sources to partially coherent laser beams would be of interest for many applications.

Bibliography

- [1] A. F. Fercher, W. Drexler, C. K. Hitzenberger, and T. Lasser, “Optical coherence tomography-principles and applications,” *Reports on progress in physics*, vol. 66, no. 2, p. 239, 2003.
- [2] X. Lu, O. Rodenko, Y. Zhang, and H. Gross, “Efficient simulation of autofluorescence effects in microscope lenses,” *Applied Optics*, vol. 58, no. 13, pp. 3589–3596, 2019.
- [3] S.-S. Schad, T. Gottwald, V. Kuhn, M. Ackermann, D. Bauer, M. Scharun, and A. Killi, “Recent development of disk lasers at trumpf,” in *Solid State Lasers XXV: Technology and Devices*, vol. 9726, p. 972615, International Society for Optics and Photonics, 2016.
- [4] W. Gao and T. Milster, “Strehl ratio for optical systems with ultrafast illumination,” *Optics express*, vol. 26, no. 14, pp. 18028–18042, 2018.
- [5] N. G. Worku and H. Gross, “Gaussian pulsed beam decomposition for propagation of ultrashort pulses through optical systems,” *Journal of the Optical Society of America A*, vol. 37, no. 1, pp. 98–107, 2020.
- [6] T. Gissibl, S. Thiele, A. Herkommer, and H. Giessen, “Two-photon direct laser writing of ultracompact multi-lens objectives,” *Nature Photonics*, vol. 10, no. 8, p. 554, 2016.
- [7] M. Vaezi, H. Seitz, and S. Yang, “A review on 3d micro-additive manufacturing technologies,” *The International Journal of Advanced Manufacturing Technology*, vol. 67, no. 5-8, pp. 1721–1754, 2013.
- [8] L. Stuerzebecher, F. Fuchs, U. D. Zeitner, and A. Tuennermann, “High-resolution proximity lithography for nano-optical components,” *Microelec-*

tronic Engineering, vol. 132, pp. 120–134, 2015.

- [9] F. Z. Fang, X. D. Zhang, A. Weckenmann, G. X. Zhang, and C. Evans, “Manufacturing and measurement of freeform optics,” *CIRP Annals - Manufacturing Technology*, vol. 62, no. 2, pp. 823–846, 2013.
- [10] M. Beier, S. Scheiding, A. Gebhardt, R. Loose, S. Risse, R. Eberhardt, and A. Tünnermann, “Fabrication of high precision metallic freeform mirrors with magnetorheological finishing (mrf),” in *Optifab 2013*, vol. 8884, p. 88840S, International Society for Optics and Photonics, 2013.
- [11] N. Heidler, E. Hilpert, J. Hartung, H. von Lukowicz, C. Damm, T. Peschel, and S. Risse, “Additive manufacturing of metal mirrors for tma telescope,” in *Optical Fabrication, Testing, and Metrology VI*, vol. 10692, p. 106920C, International Society for Optics and Photonics, 2018.
- [12] E. Hilpert, J. Hartung, H. von Lukowicz, T. Herffurth, and N. Heidler, “Design, additive manufacturing, processing, and characterization of metal mirror made of aluminum silicon alloy for space applications,” *Optical Engineering*, vol. 58, no. 9, p. 092613, 2019.
- [13] G. W. Forbes, “Never-ending struggles with mid-spatial frequencies,” in *SPIE Optical Measurement Systems for Industrial Inspection*, vol. 9525, p. 95251B, SPIE, 2015.
- [14] Q. Wu, F. Merchant, and K. Castleman, *Microscope image processing*. Academic Press, Inc., 2008.
- [15] H. Deschout, T. Lukes, A. Sharipov, D. Szlag, L. Feletti, W. Vandenberg, P. Dedecker, J. Hofkens, M. Leutenegger, and T. Lasser, “Complementarity of palm and sofi for super-resolution live-cell imaging of focal adhesions,” *Nature communications*, vol. 7, p. 13693, 2016.
- [16] N. Fitzgerald, *On extending depth of field in fast photographic lenses*. Ph.D Thesis, National University of Ireland, Galway, 2019.
- [17] V. Domnenko, T. Ivanova, and M. Gantvorg, “New object-oriented model of an arbitrary optical system,” in *SPIE Optical Design and Engineering*, vol. 5249, pp. 608–615, SPIE, 2004.

- [18] G. N. Lawrence, “Integrating geometrical and physical optics with the lens-group operator method,” in *SPIE Interantional Symposium on Optical Science, Engineering, and Instrumentation*, vol. 3780, pp. 56–65, SPIE, 2019.
- [19] T. D. Milster, “Physical optics simulation in matlab for high-performance systems,” *Optical Review*, vol. 10, no. 4, pp. 246–250, 2003.
- [20] H. Schimmel, T. Paul, and F. Wyrowski, “Concepts for modern optics software,” in *SPIE Optical Systems Design*, vol. 5962, pp. 59620C–59620C–8, SPIE, 2005.
- [21] F. Wyrowski and M. Kuhn, “Introduction to field tracing,” *Journal of Modern Optics*, vol. 58, no. 5-6, pp. 449–466, 2011.
- [22] Zemax, *OpticStudio 18.7 User Manual*. Zemax LLC, 2018.
- [23] Synopsys, *Code V Reference Manuals*. 2016.
- [24] *Wyrowski Photonics UG, Wyrowski Virtual Lab Fusion*. 2019.
- [25] U. D. Zeitner and M. Banasch, “The making of a computer-generated hologram-ernst-bernhard/kley the technology for fabricating computer-generated holograms is demanding and requires advanced lithographic techniques,” *Photonics Spectra*, vol. 42, no. 12, p. 58, 2008.
- [26] S. Horiuchi, S. Yoshida, and M. Yamamoto, “Investigation of light propagation methods used to calculate wave-optical psf,” in *SPIE Optical Systems Design*, vol. 9630, pp. 963013–963013–7, SPIE, 2015.
- [27] J. W. Goodman, *Introduction to Fourier optics*. Roberts and Company Publishers, 2005.
- [28] M. Born, E. Wolf, A. Bhatia, D. Gabor, A. Stokes, A. Taylor, P. Wayman, and W. Wilcock, *Principles of Optics: Electromagnetic Theory of Propagation, Interference and Diffraction of Light*. Cambridge University Press, 2000.
- [29] V. Nascov and P. C. Logofătu, “Fast computation algorithm for the rayleigh-sommerfeld diffraction formula using a type of scaled convolution,” *Applied Optics*, vol. 48, no. 22, pp. 4310–4319, 2009.

- [30] N. Delen and B. Hooker, “Free-space beam propagation between arbitrarily oriented planes based on full diffraction theory: a fast fourier transform approach,” *Journal of the Optical Society of America A*, vol. 15, no. 4, pp. 857–867, 1998.
- [31] N. Delen and B. Hooker, “Verification and comparison of a fast fourier transform-based full diffraction method for tilted and offset planes,” *Applied Optics*, vol. 40, no. 21, pp. 3525–3531, 2001.
- [32] L. Onural, “Exact solution for scalar diffraction between tilted and translated planes using impulse functions over a surface,” *Journal of the Optical Society of America A*, vol. 28, no. 3, pp. 290–295, 2011.
- [33] K. Matsushima, “Formulation of the rotational transformation of wave fields and their application to digital holography,” *Applied Optics*, vol. 47, no. 19, pp. D110–D116, 2008.
- [34] S. Zhang, D. Asoubar, C. Hellmann, and F. Wyrowski, “Propagation of electromagnetic fields between non-parallel planes: a fully vectorial formulation and an efficient implementation,” *Applied Optics*, vol. 55, no. 3, pp. 529–538, 2016.
- [35] K. Matsushima, H. Schimmel, and F. Wyrowski, “Fast calculation method for optical diffraction on tilted planes by use of the angular spectrum of plane waves,” *Journal of the Optical Society of America A*, vol. 20, no. 9, pp. 1755–1762, 2003.
- [36] O. Faehnle, M. Doetz, and O. Dambon, “Analysis of critical process parameters of ductile mode grinding of brittle materials,” *Advanced Optical Technologies*, vol. 6, no. 5, pp. 349–358, 2017.
- [37] M. Pohl and R. Börret, “Simulation of mid-spatials from the grinding process,” *Journal of the European Optical Society: Rapid Publications*, vol. 11, p. 16010, 2016.
- [38] J. M. Tamkin, W. J. Dallas, and T. D. Milster, “Theory of point-spread function artifacts due to structured mid-spatial frequency surface errors,” *Applied Optics*, vol. 49, pp. 4814–4824, 2010.

- [39] J. M. Tamkin, T. D. Milster, and W. J. Dallas, “Theory of modulation transfer function artifacts due to mid-spatial-frequency errors and its application to optical tolerancing,” *Applied Optics*, vol. 49, pp. 4825–4835, 2010.
- [40] W. B. Wetherell, “Effects of mirror surface ripple on image quality,” in *SPIE Image Quality*, vol. 0310, pp. 77–93, SPIE, 1981.
- [41] R. N. Youngworth and B. D. Stone, “Simple estimates for the effects of mid-frequency surface errors on image quality,” *Applied Optics*, vol. 39, p. 2198, 2000.
- [42] R. J. Noll, “Effect of mid-spatial and high-spatial frequencies on optical-performance,” *Optical Engineering*, vol. 18, no. 2, pp. 137–142, 1979.
- [43] M. Beier, *Fertigung und Kompensation von metalloptischen Hochleistungsspiegelsystemen für den visuellen Spektralbereich*. Ph.D Thesis, Friedrich-Schiller-Universität Jena, 2017.
- [44] J.-P. Negel, A. Loescher, A. Voss, D. Bauer, D. Sutter, A. Killi, M. A. Ahmed, and T. Graf, “Ultrafast thin-disk multipass laser amplifier delivering 1.4 kw (4.7 mj, 1030 nm) average power converted to 820 w at 515 nm and 234 w at 343 nm,” *Optics express*, vol. 23, no. 16, pp. 21064–21077, 2015.
- [45] T. Herffurth, S. Schröder, M. Trost, A. Duparré, and A. Tünnermann, “Comprehensive nanostructure and defect analysis using a simple 3d light-scatter sensor,” *Applied Optics*, vol. 52, no. 14, pp. 3279–3287, 2013.
- [46] M. R. Teague, “Deterministic phase retrieval: a green’s function solution,” *JOSA*, vol. 73, no. 11, pp. 1434–1441, 1983.
- [47] B. E. Saleh and M. C. Teich, *Fundamentals of photonics*. John Wiley and Sons, 2019.
- [48] L. Rabiner, R. Schafer, and C. Rader, “The chirp z-transform algorithm,” *IEEE Transactions on Audio and Electroacoustics*, vol. 17, no. 2, pp. 86–92, 1969.
- [49] L. Bluestein, “A linear filtering approach to the computation of the discrete fourier transform,” *NEREM Record*, pp. 218–219, 1968.

- [50] H. Gross, “Cascaded diffraction in optical systems. part i: Simulation model,” *JOSA A (accepted)*, 2019.
- [51] H. Gross, “Cascaded diffraction in optical systems. part ii: Example calculations,” *JOSA A (accepted)*, 2019.
- [52] D. Asoubar, S. Zhang, F. Wyrowski, and M. Kuhn, “Efficient semi-analytical propagation techniques for electromagnetic fields,” *Journal of the Optical Society of America A*, vol. 31, no. 3, pp. 591–602, 2014.
- [53] Z. Wang, S. Zhang, O. Baladron-Zorita, C. Hellmann, and F. Wyrowski, “Application of the semi-analytical fourier transform to electromagnetic modeling,” *Optics express*, vol. 27, no. 11, pp. 15335–15350, 2019.
- [54] J. Stamnes, *Waves in focal regions. Propagation, diffraction and focusing of light, sound and water waves*. Series on Optics and Optoelectronics, Bristol: A. Hilger, 1986.
- [55] D. Asoubar, S. Zhang, F. Wyrowski, and M. Kuhn, “Parabasal field decomposition and its application to non-paraxial propagation,” *Optics Express*, vol. 20, no. 21, pp. 23502–23517, 2012.
- [56] H. Gross, *Handbook of optical systems, volume 2: Physical image formation*. John Wiley & Sons, 2006.
- [57] A. v. Pfeil, F. Wyrowski, A. Drauschke, and H. Aagedal, “Analysis of optical elements with the local plane-interface approximation,” *Applied Optics*, vol. 39, no. 19, pp. 3304–3313, 2000.
- [58] A. Voronovich, *Wave scattering from rough surfaces*. Springer Series on Wave Phenomena, Springer, 1999.
- [59] J. C. Stover, *Optical scattering: measurement and analysis*, vol. 2. Bellingham: SPIE optical engineering press, 1995.
- [60] T. M. Elfouhaily and C.-A. Guérin, “A critical survey of approximate scattering wave theories from random rough surfaces,” *Waves in Random Media*, vol. 14, no. 4, pp. R1–R40, 2004.
- [61] J. W. S. B. Rayleigh, *The theory of sound*, vol. 2. Macmillan, 1896.

- [62] S. O. Rice, “Reflection of electromagnetic waves from slightly rough surfaces,” *Communications on pure and applied mathematics*, vol. 4, no. 2-3, pp. 351–378, 1951.
- [63] A. Beckmann, Petr; Spizzichino, *The Scattering of Electromagnetic Waves from Rough Surfaces*. Norwood: Artech House, Inc., 1987.
- [64] A. Broemel, C. Liu, Y. Zhong, Y. Zhang, and H. Gross, “Freeform surface descriptions. part ii: application benchmark,” *Advanced Optical Technologies*, vol. 6, no. 5, pp. 337–347, 2017.
- [65] H. Gross, A. Brömel, M. Beier, R. Steinkopf, J. Hartung, Y. Zhong, M. Oleszko, and D. Ochse, “Overview on surface representations for freeform surfaces,” in *Optical Systems Design 2015: Optical Design and Engineering VI*, vol. 9626, p. 96260U, International Society for Optics and Photonics, 2015.
- [66] C. A. Micchelli, *Interpolation of scattered data: distance matrices and conditionally positive definite functions*, pp. 143–145. Springer, 1984.
- [67] A. Broemel, U. Lippmann, and H. Gross, “Freeform surface descriptions. part i: Mathematical representations,” *Advanced Optical Technologies*, vol. 6, no. 5, pp. 327–336, 2017.
- [68] G. Fasshauer, *Meshfree Approximation Methods with MATLAB*. World Scientific, 2007.
- [69] H. Wendland, “Piecewise polynomial, positive definite and compactly supported radial functions of minimal degree,” *Advances in computational Mathematics*, vol. 4, no. 1, pp. 389–396, 1995.
- [70] G. Fasshauer and M. McCourt, “Stable evaluation of gaussian radial basis function interpolants,” *SIAM Journal on Scientific Computing*, vol. 34, no. 2, pp. A737–A762, 2012.
- [71] R. Swinbank and R. James Purser, “Fibonacci grids: A novel approach to global modelling,” *Quarterly Journal of the Royal Meteorological Society: A journal of the atmospheric sciences, applied meteorology and physical oceanography*, vol. 132, no. 619, pp. 1769–1793, 2006.

- [72] J. H. Halton, “Algorithm 247: Radical-inverse quasi-random point sequence,” *Communications of the ACM*, vol. 7, no. 12, pp. 701–702, 1964.
- [73] J. Stock, *Investigations on freeform surfaces under real conditions*. Masters Thesis, Friedrich-Schiller-Universität Jena, 2016.
- [74] X. Zhou, X. Huang, J. Bai, L. Zhao, J. Hou, K. Wang, and Y. Hua, “Representation of complex optical surfaces with adaptive radial basis functions,” *Applied optics*, vol. 58, no. 14, pp. 3938–3944, 2019.
- [75] G. Rossum, “Python reference manual,” report, CWI (Centre for Mathematics and Computer Science), 1995.
- [76] J.-P. Negel, A. Voss, M. A. Ahmed, D. Bauer, D. Sutter, A. Killi, and T. Graf, “1.1 kw average output power from a thin-disk multipass amplifier for ultra-short laser pulses,” *Optics letters*, vol. 38, no. 24, pp. 5442–5445, 2013.
- [77] A. Siegman, *Lasers*. University Science Books, 1986.
- [78] K. Klementiev and R. Chernikov, “Powerful scriptable ray tracing package xrt,” in *SPIE Optical Engineering and Applications*, vol. 9209, SPIE, 2014.
- [79] L. Samoylova, A. Buzmakov, O. Chubar, and H. Sinn, “Wavepropagator: interactive framework for x-ray free-electron laser optics design and simulations,” *Journal of Applied Crystallography*, vol. 49, no. 4, pp. 1347–1355, 2016.
- [80] N. Worku and H. Gross, “Vectorial field propagation through high na objectives using polarized gaussian beam decomposition,” in *Optical Trapping and Optical Micromanipulation XIV*, vol. 10347, p. 103470W, International Society for Optics and Photonics, 2017.
- [81] H. Gross, *Handbook of Optical Systems, Volume 5: Metrology of Optical Components and Systems*. John Wiley & Sons, 2012.
- [82] N. Lindlein and H. P. Herzig, “Design and modeling of a miniature system containing micro-optics,” in *International Symposium on Optical Science and Technology*, vol. 4437, pp. 1–13, 2001.
- [83] N. G. Worku, R. Hambach, and H. Gross, “Decomposition of a field with smooth wavefront into a set of gaussian beams with non-zero curvatures,”

- JOSA A*, vol. 35, no. 7, pp. 1091–1102, 2018.
- [84] Y.-H. Kim, G. H. Kim, H. Ryu, H.-Y. Chu, and C.-S. Hwang, “Exact light propagation between rotated planes using non-uniform sampling and angular spectrum method,” *Optics Communications*, vol. 344, pp. 1–6, 2015.
- [85] A. G. Fox and T. Li, “Modes in a maser interferometer with curved and tilted mirrors,” *Proceedings of the IEEE*, vol. 51, no. 1, pp. 80–89, 1963.
- [86] A. G. Fox and T. Li, “Resonant modes in a maser interferometer,” *Bell System Technical Journal*, vol. 40, no. 2, pp. 453–488, 1961.
- [87] B. Stroustrup, *The C++ Programming Language*. Addison-Wesley Professional, 2013.
- [88] V. Mnih, “Cudamat: a cuda-based matrix class for python,” *Department of Computer Science, University of Toronto, Tech. Rep. UTML TR*, vol. 4, 2009.
- [89] S. Behnel, R. Bradshaw, C. Citro, L. Dalcin, D. S. Seljebotn, and K. Smith, “Cython: The best of both worlds,” *Computing in Science and Engineering*, vol. 13, no. 2, p. 31, 2011.
- [90] J. Jiang, *X-Ray optical systems*. Masters Thesis, Friedrich-Schiller-Universität Jena, 2019.
- [91] B. D. Stone, “Tests for assessing beam propagation algorithms,” in *SPIE Optical Systems Design*, vol. 8171, p. 81710E, SPIE, 2011.
- [92] B. Andreas, G. Mana, and C. Palmisano, “Vectorial ray-based diffraction integral,” *Journal of the Optical Society of America A*, vol. 32, no. 8, pp. 1403–1424, 2015.
- [93] M. Tessmer and H. Gross, “Generalized propagation of light through optical systems. ii. numerical implications,” *Journal of the Optical Society of America A*, vol. 32, no. 12, pp. 2276–2285, 2015.
- [94] M. Tessmer and H. Gross, “Generalized propagation of light through optical systems. i. mathematical basics,” *Journal of the Optical Society of America A*, vol. 32, no. 2, pp. 258–266, 2015.

- [95] R. C. Jones, “A new calculus for the treatment of optical systems. description and discussion of the calculus,” *Journal of the Optical Society of America*, vol. 31, no. 7, pp. 488–493, 1941.
- [96] D. H. Goldstein, *Polarized light*. CRC press, 2016.
- [97] F. K. Kneubühl and M. W. Sigrist, *Laser*. Springer-Verlag, 2008.
- [98] A. Beer, “Bestimmung der Absorption des rothen Lichts in farbigen Flüssigkeiten,” *Ann. Physik*, vol. 162, pp. 78–88, 1852.
- [99] “11146-1 DIN EN ISO 11146: Laser und Laseranlagen–Prüfverfahren für Laserstrahlmessungen, Divergenzwinkel und Beugungsmaßzahlen,” *Berlin: Beuth*, 2005.
- [100] N. Hodgson and H. Weber, *Laser Resonators and Beam Propagation: Fundamentals, Advanced Concepts, Applications*, vol. 108. Springer, 2005.
- [101] K. Paturski, “Fraunhofer diffraction patterns of tilted planar objects,” *Optica Acta: International Journal of Optics*, vol. 30, no. 5, pp. 673–679, 1983.
- [102] C. Frère and D. Leseberg, “Large objects reconstructed from computer-generated holograms,” *Applied Optics*, vol. 28, no. 12, pp. 2422–2425, 1989.
- [103] K. Yamamoto, Y. Ichihashi, T. Senoh, R. Oi, and T. Kurita, “Calculating the fresnel diffraction of light from a shifted and tilted plane,” *Optics Express*, vol. 20, no. 12, pp. 12949–12958, 2012.
- [104] L. Yu, Y. An, and L. Cai, “Numerical reconstruction of digital holograms with variable viewing angles,” *Optics Express*, vol. 10, no. 22, pp. 1250–1257, 2002.
- [105] P. Modregger, D. Lübbert, P. Schäfer, R. Köhler, T. Weitkamp, M. Hanke, and T. Baumbach, “Fresnel diffraction in the case of an inclined image plane,” *Optics Express*, vol. 16, no. 7, pp. 5141–5149, 2008.
- [106] T. Tommasi and B. Bianco, “Computer-generated holograms of tilted planes by a spatial frequency approach,” *Journal of the Optical Society of America A*, vol. 10, no. 2, pp. 299–305, 1993.
- [107] C. Chang, J. Xia, J. Wu, W. Lei, Y. Xie, M. Kang, and Q. Zhang, “Scaled

- diffraction calculation between tilted planes using nonuniform fast fourier transform,” *Optics Express*, vol. 22, no. 14, pp. 17331–17340, 2014.
- [108] J. Keiner, S. Kunis, and D. Potts, “Using nfft 3—a software library for various nonequispaced fast fourier transforms,” *ACM Trans. Math. Softw.*, vol. 36, no. 4, pp. 1–30, 2009.
- [109] H. Gross, “Wave optical simulation of a spectral narrowed resonator,” vol. 7717, p. 77170T, SPIE Proc., 2010.
- [110] H. Goldstein, *Classical mechanics*. Pearson Education India, 1965.
- [111] J. Stock, N. G. Worku, and H. Gross, “Coherent field propagation between tilted planes,” *JOSA A*, vol. 34, no. 10, pp. 1849–1855, 2017.
- [112] R. W. Cox and T. Raoqiong, “Two- and three-dimensional image rotation using the fft,” *IEEE Transactions on Image Processing*, vol. 8, no. 9, pp. 1297–1299, 1999.
- [113] M. Unser, P. Thevenaz, and L. Yaroslavsky, “Convolution-based interpolation for fast, high-quality rotation of images,” *IEEE Transactions on Image Processing*, vol. 4, no. 10, pp. 1371–1381, 1995.
- [114] W. F. Eddy, M. Fitzgerald, and D. C. Noll, “Improved image registration by using fourier interpolation,” *Magnetic Resonance in Medicine*, vol. 36, no. 6, pp. 923–931, 1996.
- [115] K. G. Larkin, M. A. Oldfield, and H. Klemm, “Fast fourier method for the accurate rotation of sampled images,” *Optics Communications*, vol. 139, no. 1, pp. 99–106, 1997.
- [116] S. Mehrabkhani and T. Schneider, “Is the rayleigh-sommerfeld diffraction always an exact reference for high speed diffraction algorithms?,” *Optics Express*, vol. 25, no. 24, pp. 30229–30240, 2017.
- [117] E. Hilpert, J. Hartung, S. Risse, R. Eberhardt, and A. Tünnermann, “Precision manufacturing of a lightweight mirror body made by selective laser melting,” *Precision Engineering*, vol. 53, pp. 310–317, 2018.
- [118] S. Schmidt, S. Thiele, A. Herkommer, H. Giessen, and H. Gross, “Integrated

approach to realize top hat focal field distributions,” in *Imaging and Applied Optics 2017*, OSA Technical Digest (online), p. JTu5A.35, Optical Society of America, 2017.

- [119] M. Beier, J. Hartung, T. Peschel, C. Damm, A. Gebhardt, S. Scheiding, D. Stumpf, U. D. Zeitner, S. Risse, R. Eberhardt, and A. Tünnermann, “Development, fabrication, and testing of an anamorphic imaging snap-together freeform telescope,” *Applied Optics*, vol. 54, no. 12, pp. 3530–3542, 2015.
- [120] O. Cakmakci, S. Vo, H. Foroosh, and J. Rolland, “Application of radial basis functions to shape description in a dual-element off-axis magnifier,” *Optics Letters*, vol. 33, no. 11, pp. 1237–1239, 2008.
- [121] B. Chen and A. M. Herkommer, “Alternate optical designs for head-mounted displays with a wide field of view,” *Applied optics*, vol. 56, no. 4, pp. 901–906, 2017.
- [122] K. P. Thompson and J. P. Rolland, “Freeform optical surfaces: a revolution in imaging optical design,” *Optics and Photonics News*, vol. 23, no. 6, pp. 30–35, 2012.
- [123] J. Reimers, A. Bauer, K. P. Thompson, and J. P. Rolland, “Freeform spectrometer enabling increased compactness,” *Light: Science and Applications*, vol. 6, no. 7, p. e17026, 2017.
- [124] C. Liu, C. Straif, T. Flügel-Paul, U. D. Zeitner, and H. Gross, “Comparison of hyperspectral imaging spectrometer designs and the improvement of system performance with freeform surfaces,” *Applied Optics*, vol. 56, no. 24, pp. 6894–6901, 2017.
- [125] J. Hartung, M. Beier, and S. Risse, “Novel applications based on freeform technologies,” in *SPIE Optical Systems Design*, vol. 10692, p. 10, SPIE, 2018.
- [126] G. Yu, H. Li, and D. Walker, “Removal of mid spatial-frequency features in mirror segments,” *Journal of the European Optical Society: Rapid Publications*, vol. 6, p. 11044, 2011.
- [127] M. Maksimovic, “Optical tolerancing of structured mid-spatial frequency errors on free-form surfaces using anisotropic radial basis functions,” in *SPIE*

Optical Systems Design, vol. 9626, p. 14, SPIE, 2015.

- [128] J. Stock, A. Broemel, J. Hartung, D. Ochse, and H. Gross, “Description and reimplementation of real freeform surfaces,” *Applied Optics*, vol. 56, no. 3, pp. 391–396, 2017.
- [129] J. Stock, M. Beier, J. Hartung, S. Merx, and H. Gross, “Simulation and analysis of optical imaging systems including real freeform components,” *Advanced Optical Technologies*, vol. 8, no. 2, pp. 111–117, 2019.
- [130] C. Supranowitz, J.-P. Lormeau, C. Maloney, P. Murphy, and P. Dumas, “Freeform metrology using subaperture stitching interferometry,” in *Optics and Measurement International Conference 2016*, vol. 10151, p. 101510D, International Society for Optics and Photonics, 2016.
- [131] C. Supranowitz, P. Dumas, T. Nitzsche, J. D. Nelson, B. B. Light, K. Medicus, N. Smith, and R. B. Townell, “Fabrication and metrology of high-precision freeform surfaces,” in *Optifab 2013*, vol. 8884, p. 888411, International Society for Optics and Photonics, 2013.
- [132] C.-Y. Huang and R. Liang, “Modeling of surface topography in single-point diamond turning machine,” *Applied Optics*, vol. 54, no. 23, pp. 6979–6985, 2015.
- [133] T. Pertermann, J. Hartung, M. Beier, M. Trost, S. Schröder, S. Risse, R. Eberhardt, A. Tünnermann, and H. Gross, “Angular resolved power spectral density analysis for improving mirror manufacturing,” *Applied Optics*, vol. 57, no. 29, pp. 8692–8698, 2018.
- [134] K. Liang, G. W. Forbes, and M. A. Alonso, “Validity of the perturbation model for the propagation of msf structure in 2d,” *Optics Express*, vol. 27, no. 3, pp. 3390–3408, 2019.
- [135] P. Spanò, “Free-forms optics into astronomical use: the case of an all-mirror anamorphic collimator,” in *Advanced Optical and Mechanical Technologies in Telescopes and Instrumentation*, vol. 7018, p. 701840, International Society for Optics and Photonics, 2008.
- [136] V. N. Mahajan, “Orthonormal aberration polynomials for anamorphic opti-

- cal imaging systems with rectangular pupils,” *Applied optics*, vol. 49, no. 36, pp. 6924–6929, 2010.
- [137] J. Lewis, “Fast normalized cross-correlation,” *Industrial Light and Magic*, vol. 2011, 1995.
- [138] J. M. Tamkin and T. D. Milster, “Effects of structured mid-spatial frequency surface errors on image performance,” *Applied Optics*, vol. 49, pp. 6522–6536, 2010.
- [139] Q. Wang, D. Cheng, Y. Wang, H. Hua, and G. Jin, “Design, tolerance, and fabrication of an optical see-through head-mounted display with free-form surface elements,” *Applied Optics*, vol. 52, no. 7, pp. C88–C99, 2013.
- [140] T. Herffurth, *Light scattering and roughness analysis of optical surfaces and thin films*. Ph.D. Thesis, Friedrich-Schiller-Universität Jena, 2015.
- [141] A. von Finck, M. Hauptvogel, and A. Duparré, “Instrument for close-to-process light scatter measurements of thin film coatings and substrates,” *Applied Optics*, vol. 50, no. 9, pp. C321–C328, 2011.
- [142] A. von Finck, T. Herffurth, S. Schröder, A. Duparré, and S. Sinzinger, “Characterization of optical coatings using a multisource table-top scatterometer,” *Applied Optics*, vol. 53, no. 4, pp. A259–A269, 2014.
- [143] T. Gureyev, A. Roberts, and K. Nugent, “Phase retrieval with the transport-of-intensity equation: matrix solution with use of zernike polynomials,” *JOSA A*, vol. 12, no. 9, pp. 1932–1941, 1995.
- [144] L. Waller, L. Tian, and G. Barbastathis, “Transport of intensity phase-amplitude imaging with higher order intensity derivatives,” *Optics express*, vol. 18, no. 12, pp. 12552–12561, 2010.
- [145] B. C. Platt and R. Shack, “History and principles of shack-hartmann wavefront sensing,” *Journal of refractive surgery*, vol. 17, no. 5, pp. S573–S577, 2001.
- [146] J. R. Fienup, “Phase retrieval algorithms: a comparison,” *Applied optics*, vol. 21, no. 15, pp. 2758–2769, 1982.
- [147] F. Widiyasari, *Phase Retrieval for Laser Beam Characterization*. Masters The-

sis, Friedrich-Schiller-Universität Jena, 2019.

- [148] P. E. Debevec and J. Malik, “Recovering high dynamic range radiance maps from photographs,” in *ACM SIGGRAPH 2008 classes*, pp. 1–31, ACM, 2008.
- [149] A. Savitzky and M. J. Golay, “Smoothing and differentiation of data by simplified least squares procedures,” *Analytical chemistry*, vol. 36, no. 8, pp. 1627–1639, 1964.
- [150] V. N. Mahajan, “Strehl ratio of a gaussian beam,” *JOSA A*, vol. 22, no. 9, pp. 1824–1833, 2005.
- [151] D. Lowenthal, “Maréchal intensity criteria modified for gaussian beams,” *Applied optics*, vol. 13, no. 9, pp. 2126–2133, 1974.
- [152] J. Sasián, *Introduction to aberrations in optical imaging systems*. Cambridge University Press, 2013.
- [153] A. von Finck, *Table top system for angle resolved light scattering measurement*. Ph.D. Thesis, TU Ilmenau, 2014.
- [154] A. Duparre, J. Ferre-Borrull, S. Gliech, G. Notni, J. Steinert, and J. M. Bennett, “Surface characterization techniques for determining the root-mean-square roughness and power spectral densities of optical components,” *Applied optics*, vol. 41, no. 1, pp. 154–171, 2002.
- [155] F. D. Orazio Jr, W. K. Stowell, and R. M. Silva, “Instrumentation of a variable angle scatterometer (vas),” in *Scattering in Optical Materials II*, vol. 362, pp. 165–171, International Society for Optics and Photonics, 1983.
- [156] A. Duparré, “Light scattering techniques for the inspection of microcomponents and microstructures,” *Optical Inspection of Microsystems*, p. 103, 2018.
- [157] E. Church, H. Jenkinson, and J. Zavada, “Relationship between surface scattering and microtopographic features,” *Optical Engineering*, vol. 18, no. 2, p. 182125, 1979.
- [158] “Specifications Geometrical Product: Surface Texture: Areal Part 2: Terms, Definitions and Surface Texture Parameters,” *International Standard ISO*, pp. 25178–2, 2012.

- [159] C. J. Sheppard, "Pixellated circle," *Applied optics*, vol. 57, no. 27, pp. 7878–7882, 2018.
- [160] A. A. Wereszczak and C. E. Anderson Jr, "Borofloat and starphire float glasses: A comparison," *International Journal of Applied Glass Science*, vol. 5, no. 4, pp. 334–344, 2014.

A. Ehrenwörtliche Erklärung

Ich erkläre hiermit ehrenwörtlich, dass ich die vorliegende Arbeit selbständig, ohne unzulässige Hilfe Dritter und ohne Benutzung anderer als der angegebenen Hilfsmittel und Literatur angefertigt habe. Die aus anderen Quellen direkt oder indirekt übernommenen Daten und Konzepte sind unter Angabe der Quelle gekennzeichnet.

Bei der Auswahl und Auswertung folgenden Materials haben mir die nachstehend aufgeführten Personen in der jeweils beschriebenen Weise unentgeltlich geholfen:

- Prof. Dr. Herbert Gross hat das Promotionsvorhaben betreut. Er war an der Auswahl der Themen dieser Arbeit beteiligt und sowohl die Ergebnisse als auch die vorliegende Dissertation wurden mit ihm diskutiert.
- Dominik Bauer (Trumpf GmbH, Schramberg) ist stellvertretend genannt für die Konzeption und Entwicklung des Multipass Scheiben Verstärkers.
- Birk Andreas (PTB, Braunschweig) hat die Interpolations-basierte Methode für den Vergleich in Abschnitt 4.4 bereitgestellt.
- Matthias Beier (Fraunhofer IOF, Jena) ist stellvertretend genannt für die Konzeption und den Aufbau des Systems „VISTEL“. Die in Kapitel 5 gezeigten Messung wurden gemeinsam mit ihm aufgenommen.
- Tobias Herffurth und Marcus Trost (beide Fraunhofer IOF, Jena) haben die Messergebnisse in Kapitel 6 bereitgestellt. Die Modellierung des Streulichts an rauen Oberflächen basiert auf von ihnen bereitgestellten Implementierungen.
- Der Ansatz und experimentelle Aufbau zur Rekonstruktion der Phase wurden zusammen mit Sebastian Merx (IAP, Jena) realisiert. Geeignete Parameter wurden gemeinsam mit Fransiska Wideasari im Rahmen einer Masterarbeit evaluiert.

- Im Übrigen waren jeweils die Koautoren der aus dieser Arbeit entstandenen Veröffentlichungen, siehe Publikationsliste, an der Interpretation und Diskussion der Ergebnisse beteiligt.

Weitere Personen waren an der inhaltlich-materiellen Erstellung der vorliegenden Arbeit nicht beteiligt. Insbesondere habe ich hierfür nicht die entgeltliche Hilfe von Vermittlungs- bzw. Beratungsdiensten (Promotionsberater oder andere Personen) in Anspruch genommen. Niemand hat von mir unmittelbar oder mittelbar geldwerte Leistungen für die Arbeiten erhalten, die im Zusammenhang mit dem Inhalt der vorgelegten Dissertation stehen.

Die Arbeit wurde bisher weder im In- noch im Ausland in gleicher oder ähnlicher Form einer anderen Prüfungsbehörde vorgelegt.

Die geltende Promotionsordnung der Physikalisch-Astronomischen Fakultät ist mir bekannt.

Ich versichere ehrenwörtlich, dass ich nach bestem Wissen die reine Wahrheit gesagt und nichts verschwiegen habe.

Jena, den

Johannes Maximilian Stock

B. Liste der wissenschaftlichen Veröffentlichungen und Vorträge

Artikel in Fachzeitschriften (peer-reviewed)

1. J. Stock, M. Beier, J. Hartung, S. Merx und H. Gross, „Simulation and analysis of optical imaging systems including real freeform components” in *Advanced Optical Technologies* 8 (2), 111-117 (De Gruyter, 2019)
2. S. Merx, J. Stock und H. Gross, „Fast computation and characterization of perturbed Bessel-Gauss beams” in *JOSA A* 36 (11), 1892-1897 (Optical Society of America, 2019)
3. J. Stock, N. G. Worku und H. Gross, „Coherent field propagation between tilted planes” in *JOSA A* 34 (10), 1849-1855 (Optical Society of America, 2017)
4. J. Stock, A. Broemel, J. Hartung, D. Ochse, und H. Gross, „Description and Reimplementation of Real Freeform Surfaces” in *Applied Optics* 56, 391-396 (Optical Society of America, 2017)
5. M. Fischer, C. Schmidt, E. Sakat, J. Stock, A. Samarelli, J. Frigerio, M. Ortolani, D. Paul, G. Isella, A. Leitenstorfer, P. Biagioni und D. Brida, „Optical Activation of Germanium Plasmonic Antennas in the Mid-Infrared“ in *Physical Review Letters* 117(4), 047401 (American Physical Society, 2016)

Konferenzbeiträge und Vorträge

1. J. Stock, M. Beier, J. Hartung, S. Merx und H. Gross, „Optical simulation of an imaging telescope including manufactured freeform surfaces” in EOSAM Delft 2018: Design, Tolerancing and Fabrication, (European Optical Society, 2018)
2. S. Merx, J. Stock und H. Gross, „Sensitivity analysis of Bessel-beams generated by axicons” in EOSAM Delft 2018: Design, Tolerancing and Fabrication, (European Optical Society, 2018)
3. J. Stock, „Holistic simulation of optical systems”, Doktorandentag der Carl-Zeiss AG 2018
4. A. Broemel, J. Stock und H. Gross, „Beschreibung von Freifromflächen in Design und Fertigung”, Keynote, 1. OptecNet Jahrestagung Mainz 2017
5. M. Fischer, C. Schmidt, J. Stock, E. Sakat, A. Samarelli, J. Frigerio, P. Biagioni, D. Paul, G. Isella, A. Leitenstorfer und D. Brida, „Optical Switching of Mid-Infrared Plasmonic Nanoantennas Based on Germanium” in CLEO: 2015, OSA Technical Digest, paper FW3E.2. (Optical Society of America, 2015)

C. Danksagung

Diese Arbeit wäre ohne die Unterstützung und den Rückhalt von vielen unterschiedlichen Personen nicht möglich gewesen, denen ich im Folgenden danken möchte.

An erster Stelle sei hier Prof. Dr. Herbert Gross genannt. Du hast mir nicht nur die Promotion an deinem Lehrstuhl ermöglicht und mich die letzten drei Jahre auf dem Weg zu dieser Arbeit begleitet, sondern hast mich zu jeder Zeit mit deinem unerschöpflichen Wissen unterstützt und meine Begeisterung für die Optik wachsen lassen. Darüber hinaus hast du die Entwicklung meiner Persönlichkeit in den letzten Jahren stark geprägt. Vielen Dank für dein Vertrauen in mich.

Viele Ergebnisse dieser Arbeit sind in unterschiedlichen Kooperationen entstanden. Besonders hervorheben möchte ich Matthias Beier, Johannes Hartung, Tobias Herfurth und Marcus Trost vom Fraunhofer IOF Jena, Birk Andreas von der PTB in Braunschweig und Dominik Bauer, stellvertretend genannt für die Trumpf GmbH. Der wertvolle Austausch mit euch und die Anmerkungen zu dieser Dissertation haben mir sehr geholfen. Danke für die tolle Zusammenarbeit.

Der Carl-Zeiss-Stiftung danke ich für die Unterstützung in Form eines Promotionsstipendiums und den dadurch gemachten Bekanntschaften mit anderen Wissenschaftlern.

Euch, Brett Robertson, Richard Chipper, Michael Kapfer und Joshua Goncalves, danke ich für eine grandiose Zeit in Perth. Ihr habt mir nicht nur einen mehrmonatigen Forschungsaufenthalt bei AIRO ermöglicht, sondern auch die australische Kultur und Mentalität näher gebracht. Außerdem ein großes Dankeschön an dich, Josh, für die sprachliche Korrektur all meiner Forschungsarbeiten.

Danke an die gesamte Optik-Design-Gruppe und an sämtliche Kollegen, die mich begleitet und mit großartigem Kuchen versorgt haben. Meine Zeit am Institut für

Angewandte Physik wäre ohne euch nur halb so schön gewesen.

Ein fester Bestandteil eines jeden Tages war das gemeinsame Mittagessen und der damit verbundene Spaziergang. Basti, Enrico, Johannes, Sebastian, Sören, Christoph und Ralf, auch wenn ihr alle an eurer Pünktlichkeit arbeiten solltet, werde ich diese kleine Auszeit mit euch sehr vermissen.

Ein ganz besonders großer Dank gilt meinem Nachbarn, sowohl am Schreibtisch als auch zu Hause. Lieber Basti, gerade auf den letzten Metern dieser Arbeit hast du mich fernab jeder Selbstverständlichkeit unterstützt. Auf dich war jeder Zeit Verlass. Ich hoffe ich kann dir dies irgendwann zurückgeben.

Darüber hinaus möchte ich mich bei Alexander, Arne, Benni, Andy, Stefan, Magdalena, Johannes, Gabriel und Christopher für die unglaubliche und oftmals unerwartete Unterstützung bedanken. Egal ob bei gemeinsamen Radfahrten, Abendessen oder Ausflügen, ihr habt mir den nötigen Ausgleich verschafft.

Der bedingungslose Rückhalt meiner Familie bedeutet mir sehr viel. Wieder einmal habt ihr mir gezeigt, dass ich mich voll und ganz auf euch verlassen kann und ihr mich stets auf den Boden der Tatsachen zurückholt. Jedes Wochenende bei euch zu Hause hat mir Kraft gegeben.

Die letzten Zeilen dieser Arbeit gehören der wichtigsten Person in meinem Leben. Liebe Dagmar, danke für einfach alles!